PhD THESIS

VISCOUS FINGERING IN COMPLEX MAGNETIC FLUIDS: WEAKLY NONLINEAR ANALYSIS, STATIONARY SOLUTIONS AND PHASE-FIELD MODELS

Sérgio Henrique Albuquerque Lira

Recife - PE, Brazil

2014

UNIVERSIDADE FEDERAL DE PERNAMBUCO
DEPARTAMENTO DE FÍSICA – CCEN
PROGRAMA DE PÓS-GRADUAÇÃO EM FÍSICA

TESE DE DOUTORADO

VISCOUS FINGERING IN COMPLEX MAGNETIC FLUIDS: WEAKLY NONLINEAR ANALYSIS, STATIONARY SOLUTIONS AND PHASE-FIELD MODELS

por

Sérgio Henrique Albuquerque Lira

Tese apresentada ao Programa de Pós-Graduação em Física do Departamento de Física da Universidade Federal de Pernambuco como parte dos requisitos para obtenção do título de Doutor em Física.

Orientador:

Prof. José Américo de Miranda Neto (Orientador, DF-UFPE)

Recife - PE, Brasil
Fevereiro - 2014

Catalogação na fonte
Bibliotecário Jefferson Luiz Alves Nazareno, CRB 4-1758

Lira, Sérgio Henrique Albuquerque.
Viscous fingering in complex magnetic fluids: weakly nonlinear analysis, stationary solutions and phase-field models. / Sérgio Henrique Albuquerque Lira. – Recife: O Autor, 2014.
129 f.: fig., graf.

Orientador: José Américo de Miranda Neto.
Tese (Doutorado) - Universidade Federal de Pernambuco. CCEN. Física, 2014.
Inclui referências.

1. Dinâmica dos fluidos. 2. Fluidos não-newtonianos. 3. Fluidos magnéticos. I. Miranda Neto, José Américo de. (Orientador). II. Título.

532.05 (22. ed.) FQ 2014-38

Universidade Federal de Pernambuco
Departamento de Física – CCEN
Programa de Pós-Graduação em Física
Cidade Universitária - 50670-901 Recife PE Brasil
Fone (++ 55 81) 2126-7640/2126-8449
http://www.ufpe.br/ppgfisica e-mail: posgrad@df.ufpe.br

Parecer da Banca Examinadora de Defesa de Tese de Doutorado

Sérgio Henrique Albuquerque Lira

VISCOUS FINGERING IN COMPLEX MAGNETIC FLUIDS: WEAKLY NONLINEAR ANALYSIS, STATIONARY SOLUTIONS AND PHASE-FIELD MODELS

A Banca Examinadora composta pelos Professores José Américo de Miranda Neto (Presidente e Orientador), Renê Rodrigues Montenegro Filho, Wilson Barros Junior, todos do Departamento de Física da Universidade Federal de Pernambuco, Antonio Martins Figueiredo Neto, do Instituto de Física da Universidade de São Paulo e Jaume Casademunt Viader, do Departamento de Estrutura e Constituintes da Matéria da Universidade de Barcelona, Espanha, consideram o candidato:

(X) Aprovado ( ) Reprovado ( ) Em exigência

Secretaria do Programa de Pós-Graduação em Física do Departamento de Física do Centro de Ciências Exatas e da Natureza da Universidade Federal de Pernambuco, em vinte e um de fevereiro de dois mil e catorze.

Prof. José Américo de Miranda Neto
Presidente e Orientador

Prof. Renê Rodrigues Montenegro Filho

Prof. Wilson Barros Junior

Prof. Antonio Martins Figueiredo Neto

Prof. Jaume Casademunt Viader

To my grandparents: Domingos, Elza, Ivete and José.

Acknowledgements

First of all, I thank prof. José Miranda for all the advising support and confidence in our research. It has been a pleasure to work with him during all these years, to be part of his group in Recife and also to be his personal friend.

I also thank prof. Jaume Casademunt for receiving me so well at the Universitat de Barcelona. I am very grateful for being able to work there on the lamellar fragment problem under his supervision during my one year sandwich stage. Living in Barcelona was indeed an amazing experience and made me grow personally and academically.

I thank Rafael Oliveira for all the collaboration in obtaining the exact stationary solutions presented in Chapter 3, and also for further numerical discussions. I thank João Fontana for the collaboration on the yield stress problem of Chapter 4. I thank Carles Blanch-Mercader very much for all the support on numerical and analytical discussions that led us to the results presented in Chapter 5.

I am also thankful to Hermes Gadêlha for all the nice discussions about biological problems. To my colleagues Eduardo and Chico for their joyful company and fruitful discussions. To the Fractal members Victor, Tiago, Leo and Hugo, for organizing great meetings. To everyone that helped me at the UB and made my staying there be so pleasant, especially to my office colleagues Xumeu, Elisenda and Albert.

In addition, I would like thank all the members of the jury for accepting being part of this process and useful comments.

Finally, my special thanks to my wife Fernanda for unconditional love and support.

For financial support I thank to CNPq and INCT-FCx.

It is not knowledge, but the act of learning, not possession but the act of getting there, which grants the greatest enjoyment.

—CARL FRIEDRICH GAUSS

Resumo

Nesta Tese são empregadas técnicas analíticas e numéricas para investigar o fenômeno de formação de dedos viscosos entre fluidos imiscíveis confinados quando um destes fluidos é um fluido magnético complexo. Diferentes tipos de esquemas geométricos efetivamente bidimensionais foram investigados. Duas situações distintas são tomadas com relação à natureza da amostra de fluido magnético: um fluido newtoniano usual, e um fluido magneto-reológico que apresenta um *yield stress* dependente da intensidade do campo magnético. Equações governantes adequadas são derivadas para cada um dos casos. Para obter um entendimento analítico dos estágios iniciais da evolução temporal da interface foi empregada uma análise fracamente não-linear de modos acoplados. Este tipo de análise acessa a estabilidade de uma interface inicialmente perturbada e também revela a morfologia dos dedos emergentes. Em algumas circunstâncias soluções estacionárias podem ser encontradas mesmo na ordem não-linear mais baixa. Nesta situação é feita uma comparação de algumas destas soluções com soluções estáticas totalmente não-lineares obtidas através de um formalismo de vortex-sheet na condição de equilíbrio. Em seguida foi desenvolvido um modelo de *phase-field* aplicado a fluidos magnéticos que é capaz de simular numericamente a dinâmica totalmente não-linear do sistema. O modelo consiste em introduzir uma função auxiliar que reproduz uma interface difusa de espessura finita. Utilizando esta ferramenta também é possível estudar um complexo problema de dedos viscosos de origem biológica: o fluxo de actina como um fluido ativo dentro de um fragmento lamelar.

Palavras-chave: Formação de dedos viscosos. Ferrofluido. Fluido magneto-reológico. *Yield stress*. *Phase-field*.

Abstract

In this thesis, analytical and numerical approaches are employed in order to investigate the phenomenon of viscous fingering between confined immiscible fluids when one of the fluids is a complex magnetic fluid. Different types of effectively two-dimensional geometrical setups and applied magnetic field configurations are investigated. Two distinct situations are taken for the nature of magnetic fluid sample: a regular Newtonian ferrofluid, and a magnetorheological fluid that presents a magnetic field-dependent yield stress. Suitable governing equations are derived for each one of the cases. To obtain analytical insight about early stages of the time evolving interface we employ a weakly nonlinear mode-coupling approach. This kind of analysis accesses the stability of an initially perturbed interface, and also reveals the morphology of the emerging fingers. At some circumstances, stationary solutions may be found already at lowest nonlinear order. In this context, we compare some of these solutions to fully nonlinear steady profiles obtained by using a vortex-sheet formalism at the equilibrium condition. Moreover, we develop a phase-field model applied to magnetic fluids that is capable of numerically simulate the fully nonlinear dynamics of the system. The model consists on introducing an auxiliary function that reproduces a diffuse interface of finite thickness. By utilizing this tool we are also able to study a complex viscous fingering problem of biological origin: the flow of actin as an active fluid inside of a lamellar fragment.

Keywords: Viscous fingering. Ferrofluid. Magnetorheological fluid. Yield stress. Phase-field.

List of Figures

Contents

CHAPTER 1

Introduction

1.1 Pattern formation in viscous fingering

Classical viscous fingering pattern formation takes place when a less viscous fluid displaces a more viscous one in the confined geometry of two narrowly spaced parallel plates, the so called Hele-Shaw (H-S) cell [1]. The initially flat interface between these two immiscible fluids becomes unstable, so broad perturbations arise and tend to grow, what is commonly referred to as the Saffman-Taylor instability (see Fig. 1.1). This problem has produced a lot interest for physicists and engineers during several decades due to its prototypical character with many theoretical and practical implications. Mathematically, it is defined as a nonlocal moving boundary problem of Laplacian growth, and it is intimately related to a variety of groundbreaking phenomena, such as dendritic growth, oil recovery, etc [2]. In practice, it is an excellent laboratory because of its relative simplicity both experimentally and in its theoretical formulation.

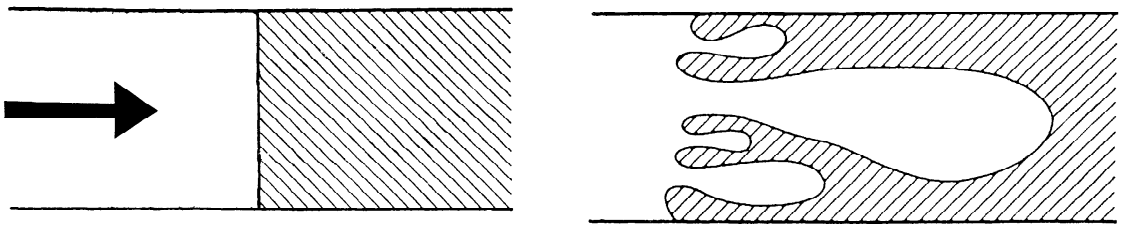

Figure 1.1: Schematic top views of the Saffman-Taylor instability based on experiments at the channel geometry [3].

Despite of being most known by its classical viscosity-driven setup, the Saffman-Taylor instability may also be driven by other kinds of mechanisms. For instance, the rotating Hele-

Shaw problem is a variation of the traditional instability [1, 2], in which the cell rotates, and the competition between centrifugal and capillary forces results in interface destabilization. During the last two decades different aspects of the problem have been investigated, including the development of zero surface tension time-dependent exact solutions [4, 5, 6], the consideration of miscible fluid displacements [7], the dependence of pattern morphologies on viscous [8, 9] and wetting [10] effects, the influence of Coriolis force on the interfacial dynamics [11, 12], and the occurrence of complex pinch-off phenomena [13].

Another suggestive variant of the Hele-Shaw problem with usual viscous fluids considers that at least one of the fluids is a ferrofluid [14, 15], a superparamagnetic liquid which promptly responds to even modest magnetic stimuli. This property turns out to be very interesting since it introduces the possibility of generating pretty different viscous fingering patterns by adjusting an applied magnetic field. One compelling example of pattern-forming systems in confined ferrofluids is related to the labyrinthine instability [16, 17, 18], in which highly branched structures are formed when a magnetic field is applied perpendicularly to the plates of a Hele-Shaw cell (see left panel in Fig. 1.2). Beautiful spiral patterns and amazing protozoan-like shapes can also arise when a rotating magnetic field is added to the perpendicular field setup [20] (see right panel in Fig. 1.2). The emergence of peculiar diamond-ring-shaped structures has been detected in centrifugally-driven Hele-Shaw flows under the action of an azimuthal magnetic field [21]. In addition, quite regular n-fold symmetric shapes emerge in both immiscible [22] and miscible [23] ferrofluids when perpendicular and azimuthal magnetic fields are applied simultaneously. Finally, the development of starfish-like morphologies has been recently predicted if a radial magnetic field configuration is used [24].

In contrast to what happens to ferrofluids, the investigation of Hele-Shaw pattern formation with magnetorheological (MR) fluids has been amply overlooked. Magnetorheological fluids consist of much larger, micronsized magnetized particles dispersed in aqueous or organic carrier liquids. The unique feature of this kind of magnetic fluid is the abrupt change in its viscoelastic properties upon the application of an external magnetic field [25, 26, 27, 28, 29] (see Fig. 1.3). In the absence of an applied field ("off" state) the magnetized particles in the suspension are randomly distributed, so that MR fluids appear similar to usual nonmagnetic fluids.

Figure 1.2: Ferrofluid viscous fingering patterns produced by different magnetic field configurations. The left panel [19] depicts the labyrinthine instability formed when a uniform magnetic field is applied perpendicularly to the plates. The mid and right panels [20] show spiral and protozoan-like shapes that arise when a rotating magnetic field is added to the perpendicular field.

However, when a magnetic field is applied ("on" state) the large particles suspended in the fluid interact, and tend to align and link together along the field's direction, creating long particle chains, columns, and other more complex structures. Interestingly, the formation of such structures restrict the motion of the fluid, allowing it to display a solidlike behavior. A MR fluid can be characterized by its yield stress, which measures the strength of the field-induced structures formed.

Despite all the efforts and important results obtained by researchers on the development of viscous fingering in Newtonian Hele-Shaw flows (i. e., constant viscosity fluid flow), the pattern forming dynamics with yield stress fluids, even at the nonmagnetic case, has been relatively underlooked. In contrast to Newtonian fluids, yield stress fluids [30, 31] can support shear stresses without flowing. As long as the stress remains below to a certain critical value they do not flow, but respond elastically to deformation. So, such materials possess properties of both viscous fluids and elastic solids, behaving like a "semi-solid". On the theoretical side, a linear stability analysis of the Saffman-Taylor problem in rectangular and radial cells with yield stress fluids [32] has predicted that the instability can be drastically modified. On the experimental arena some interesting findings have been disclosed in channel geometry [33, 34]: depending on whether viscous effects or yield stresses dominates, fractal patterns, or ramified

Figure 1.3: Magnetorheological fluid sample at the abscence of an applied magnetic field (left) and at the presence of a magnet (right).

structures where multiple fingers propagate in parallel may arise.

Another remarkable scenario in which viscous fingering takes place is that of biological fluids. Recently, it has been shown that in appropriate circumstances the flow of actin in lamellar fragments satisfies Darcy's law in an effectively two-dimensional geometry [35, 36], thus reducing the dynamics to a free-boundary problem similar to that of viscous-fingering in Hele-Shaw cells, but with different boundary conditions [37]. The comprehension of this mechanism is of major importance for one to attain shape polarization that allows cell motility and threadmilling. As shown in Fig. 1.4, a lamellar cell fragment may undergo on a shape transition that produces threadmilling by actin polymerization.

In order to fill some of the gaps exposed above, this Thesis proposes a theoretical study about the viscous fingering phenomenon in complex magnetic fluids. And by complex magnetic fluids we comprehend ferrofluids, MR fluids, yield stress fluids and lamellar fragments. During its development, we make use of analytical and numerical tools to elucidate the main aspects of the dynamics and morphology of such interfacial pattern formations.

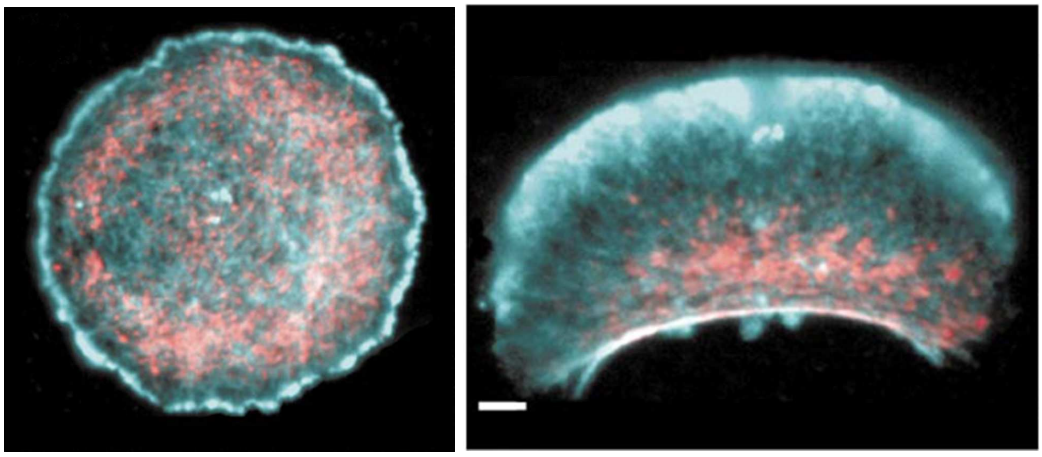

Figure 1.4: Figure extracted from [35]. The left panel shows a fairly circular actin lamellar fragment that does not propagate. When perturbed this fragment may acquire the steady shape in the right panel that propagates upwards, where the white bar in the bottom gives a one micrometer scale.

1.2 Darcy's law for Newtonian fluids

We now make a brief derivation of the governing equations for classical viscous fingering in regular Newtonian fluids. By understanting this simpler situation we will be able to describe more complex systems in our further investigation.

Consider two immiscible and incompressible fluids of viscosity η_j and density ρ_j (where $j = 1,2$ labels the different fluids) are placed between two parallel rigid plates of transversal separation b. The equation that governs the hydrodynamic flow of such fluids is the Navier-Stokes equation

$$\rho_j \left[\frac{\partial \mathbf{u}_j}{\partial t} + (\mathbf{u}_j \cdot \nabla)\mathbf{u}_j \right] = -\nabla P_j + \eta_j \nabla^2 \mathbf{u}_j, \tag{1.1}$$

where $\mathbf{u}$ is the 3-D fluid velocity and P is its 3-D pressure field. Eventual extra forces would appear added at the right hand side of Eq. (1.1). Since we are dealing with an effective two-dimensional problem, we may reduce the 3-D flow to an equivalent 2-D one by gap-averaging Eq. (1.1) at the direction perpendicular to the plates. This is done by considering non-slip boundary conditions at the plates and taking, thus, the velocity profile as being parabolic at

the transversal direction. We also assume that the lubrication approximation is valid, i. e., that inertial terms in the right hand side of Eq. 1.1 are negligible when compared to viscous contributions. By following these steps we get Darcy's law

$$\mathbf{v}_j = -\frac{b^2}{12\eta_j}\nabla p_j, \tag{1.2}$$

where $\mathbf{v}$, p and ∇ are now the gap-averaged velocity, pressure and 2-D gradient operator, respectively. This is also the equation that describes fluid flow in porous media.

To complete the description of the moving boundary problem between two fluids we must also take into account the boundary conditions across the fluid-fluid interface

$$(\mathbf{v}_2 - \mathbf{v}_1)\cdot\mathbf{n} = 0, \tag{1.3}$$

$$(\mathbf{v}_2 - \mathbf{v}_1)\cdot\mathbf{s} = \frac{2b^2}{12(\eta_1+\eta_2)}\mathbf{s}\cdot[\nabla(p_1 - p_2) + A(\mathbf{v}_2 + \mathbf{v}_1)], \tag{1.4}$$

where $A = (\eta_1 - \eta_2)/(\eta_1 + \eta_2)$ is the viscous contrast. Eq. (1.3) is the kinematic boundary condition and it imposes that both fluids have the same normal velocity component at the interface, since the normal interface velocity itself is given by $V_n = \mathbf{v}_2\cdot\mathbf{n} = \mathbf{v}_1\cdot\mathbf{n}$. On the other hand, Eq. (1.4) says that the tangential velocity components are discontinuous at the interface, and we say that $(\mathbf{v}_2 - \mathbf{v}_1)\cdot\mathbf{s}$ is the interface vortex-sheet. This is the only source of vorticity in the problem, since at each bulk phase Eq. (1.2) guarantees that the flow is vortex-free. The remaining ingredient is the pressure jump condition

$$p_1 - p_2 = \sigma\kappa, \tag{1.5}$$

where σ is the surface tension between the fluids and κ is the interface in-plane curvature.

To conclude we point out that since the fluids are incompressible

$$\nabla\cdot\mathbf{v_j} = 0, \tag{1.6}$$

what means pressure obeys Laplace's equation $\nabla^2 p_j = 0$. Therefore the moving boundary

problem is completely determined in terms of the velocity field by Eqs. (1.6), (1.3) and (1.4).

1.3 Thesis outline

In Chapter 2 we investigate the problem of a ferrofluid confined in a vertical Hele-Shaw cell and subjected to an in-plane uniform magnetic field. In Section 2.1 we take the particular case where the applied magnetic field is normal to the initially flat interface and show the main results of Ref. [38]. In Section 2.2 we subject both upper and lower fluids to a parallel flow and let the applied magnetic field to make a tilting angle with the initial interface, as in Ref. [39]. In both cases, we perform a weakly nonlinear analysis that is able to reproduce the morphology of such pattern formation phenomenon at lowest nonlinear order. A mode-coupling theory is used to compare the early nonlinear evolution of the interface with asymptotic shapes obtained when relevant forces equilibrate. Our nonlinear results indicate that the time-evolving shapes tend to approach stable stationary solutions for the normal magnetic field case, and propagating steady nonlinear waves for the tilted field.

In Chapter 3 we study the behavior of a magnetorheological fluid droplet confined to a Hele-Shaw cell in the presence of an applied magnetic field. In Section 3.1 we consider the case of an in-plane radially increasing external magnetic field case, as explored in Ref. [40]. In Section 3.2 we take a rotating H-S cell under the presence of an azimuthal field produced by a current carrying wire, as in Ref. [41]. Interfacial pattern formation is investigated by considering the competition among capillary, viscoelastic, and magnetic forces. The contribution of a magnetic field-dependent yield stress is taken into account. Linear stability analysis reveals the stabilizing role played by yield stress. On the other hand, a mode-coupling approach predicts that the resulting fingering structures should become less and less sharp as yield stress effects are increased. By employing a vortex-sheet formalism we have been able to identify a family of exact stationary solutions of the problem. A weakly nonlinear approach is employed to examine this fact and to gain analytical insight into relevant aspects related to the stability of such exact stationary solutions.

In Chapter 4 we report analytical results contained in Ref. [42] for the development of interfacial instabilities in a radial Hele-Shaw cell in which a nonmagnetic yield stress fluid is pushed by a Newtonian fluid of negligible viscosity. By dealing with a gap averaging of the Navier-Stokes equation, we derive a Darcy-law-like equation for the problem, valid in the regime of high viscosity compared to yield stress effects, and that accounts for a general yielding direction.

In Chapter 5 we present phase-field numerical models inspired by Ref. [43] that simulate viscous fingering in a H-S cell. In Section 5.2 we develop such diffuse interface method for the case of magnetic fluids, and in Section 5.3 this is done for the case of lamellar fragments.

Finally, in Chapter 6 we present our main conclusions and perspectives.

CHAPTER 2

Field-induced patterns in ferrofluids

A ferrofluid is a stable colloidal suspension of nanometric magnetic particles dispersed in a nonmagnetic liquid carrier [14, 15] which responds paramagnetically to applied magnetic fields. The most remarkable feature of this material is the fact that it combines the fluidity of liquids and the magnetic properties typical of solids. The magnetic susceptibility of ferrofluids is much higher than that of ordinary solid paramagnets, so that it promptly reacts to even minor magnetic stimuli. This behavior leads to the development of a number of interesting field-induced interfacial instabilities, and pattern formation processes which have attracted much interest [44, 45, 46, 47, 48].

One striking example of pattern-forming systems in ferrofluids is the popular Rosensweig (or, peak) instability [49]. It occurs when a uniform magnetic field is applied normal to an initially flat, ferrofluid free surface. The competition between magnetic, gravitational, and capillary forces results in the rising of a three-dimensional (3D) array of spiky structures, that look like horns growing from the liquid free surface. During the last four decades both linear and nonlinear aspects of the problem have been vigorously investigated [49, 50, 51, 52, 53, 54]. Recent variations of this archetypal ferrohydrodynamic instability revealed other exceptional properties such as the formation of stable solitonlike structures at the magnetic fluid-air interface [55], the verification of a hybrid-type instability in miscible ferrofluids where peak and labyrinthine patterns arise [56], and the occurrence of magnetic wave turbulence on the surface of the ferrofluid [57].

An effectively 2D counterpart of the traditional 3D Rosensweig instability can be obtained when a more viscous and more dense ferrofluid is placed below a nonmagnetic fluid in the confined geometry of a vertical Hele-Shaw cell. Experimental studies [58, 59] have demonstrated that the initially flat fluid-fluid interface goes unstable if a uniform magnetic field is applied normal to it, and in the plane of the Hele-Shaw cell. It has been shown that above a certain

critical value of the applied field, the interface deforms leading to the formation of a regular pattern formed by a periodic line of quasi-2D peaked structures. In Ref. [59] a Darcy's law approach is used to describe the early dynamics of such ferrofluid peak arrangement. The initial evolution of small interfacial deformations has been studied by a linear stability analysis, in which the condition for the neutrality of such deformations was determined. However, not much has been discussed about the development of such confined peak-shaped morphology at nonlinear stages of the dynamics.

A related theoretical investigation [52] tried to mimic the fully 3D Rosensweig problem by focusing on an idealized version of the system. A high-order perturbative approach has been employed to study the static surface profile of a vertical, truly 2D ferrofluid layer subjected to a normal magnetic field. The starting point of their analysis assumes that the shape of the perturbed ferrofluid interface is determined by a pressure equilibrium condition. In this context, a somewhat cumbersome Galerkin-type anzatz is used to expand both the magnetic field and the surface deflection up to fifth-order in the perturbation amplitudes. As a result, peaks are obtained for larger values of the applied magnetic field. Despite the relative intricacy of their analytical method, no specific mechanism is proposed to explain the formation of the static peaks within the nonlinear regime. Moreover, the nonlinear stability of such static structures has not been analyzed.

2.1 Normal-field instability in confined ferrofluids

In this section we show that the phenomenon of ferrofluid peak formation in vertical Hele-Shaw cells under a normal, in-plane magnetic field can be properly reproduced at lowest nonlinear perturbative order through a mode coupling approach of the dynamics [60, 61]. By employing a second-order theory and considering the interplay of a small number of Fourier modes, we show that the main features of the ferrofluid peak formation in confined geometry can be revealed in a very simple and clear manner. The nonlinear coupling is due to the influence of a normal magnetic traction term which appears in a generalized Young-Laplace

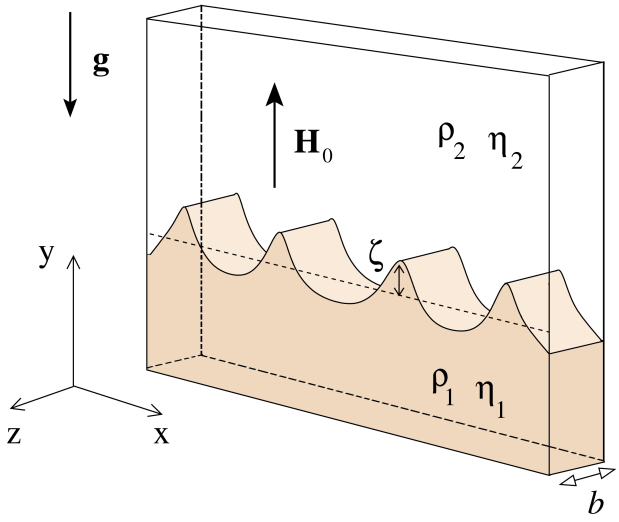

Figure 2.1: Schematic illustration of the vertical Hele-Shaw cell setup. Fluid 1 is a ferrofluid (shaded region), while fluid 2 is nonmagnetic. The densities and viscosities of the fluids are respectively denoted by ρ_j, and η_j, where $j = 1$ and 2. A uniform magnetic field $\mathbf{H}_0$ is applied along the positive y direction, and the acceleration of gravity points downward ($\mathbf{g} = -g\hat{\mathbf{y}}$). The cell has thickness b, and interfacial perturbations are represented by $\zeta = \zeta(x,t)$.

pressure drop boundary condition for ferrofluids. We have also studied the stationary shapes obtained when the forces involved balance equally. This offers the opportunity to contrast the shapes of time evolving and steady state structures. Nonlinear stationary solutions are found to be stable.

2.1.1 Mode coupling strategy

Consider a vertical Hele-Shaw cell of thickness b containing two semi-infinite immiscible viscous fluids. Denote the densities and viscosities of the lower and upper fluids, respectively as ρ_1, η_1 and ρ_2, η_2 (Fig. 2.1). The cell lies parallel to the xy plane, where the y axis is vertically upward. Between the two fluids there exists a surface tension σ, and the lower fluid is assumed to be a ferrofluid (magnetization $\mathbf{M}$), while the upper fluid is nonmagnetic (zero magnetization). Acceleration of gravity $\mathbf{g} = -g\hat{\mathbf{y}}$, where $\hat{\mathbf{y}}$ denotes the unit vector in the y-axis.

A uniform external magnetic field $\mathbf{H}_0 = H_0\hat{\mathbf{y}}$ is applied in the plane of the cell, being normal to the initially flat fluid-fluid interface.

Due to the action of the magnetic field the fluid-fluid interface may deform, and its perturbed shape is described as $\mathscr{I}(x,y,t) = y - \zeta(x,t) = 0$, where $\zeta(x,t) = \sum_{k=-\infty}^{+\infty} \zeta_k(t)\exp(ikx)$ represents the net interface perturbation with Fourier amplitudes $\zeta_k(t)$, and wave numbers k. We follow the standard approximations used by other investigators [14, 15, 16, 17, 62, 63] and assume that the ferrofluid is magnetized such that its magnetization is constant and collinear with the applied field $\mathbf{M}(\mathbf{H}) = M(H_0)\hat{\mathbf{y}}$. We consider only the lowest order effect of the magnetic interactions that would result in fluid motion.

For the confined geometry of a Hele-Shaw cell, we reduce the 3D flow to an equivalent 2D one by averaging the Navier-Stokes equation over the direction perpendicular to the plates (defined by the z axis). Using no-slip boundary conditions and neglecting inertial terms, one derives a modified Darcy's law as [17, 38, 59, 62]

$$\mathbf{v}_j = -\frac{b^2}{12\eta_j}\left\{\nabla p_j - \frac{1}{b}\int_{-b/2}^{+b/2} \mu_0(\mathbf{M}\cdot\nabla)\mathbf{H}dz + \rho_j g\hat{\mathbf{y}}\right\} \tag{2.1}$$

where $j = 1$ ($j = 2$) labels the lower (upper) fluid, and p_j denotes the hydrodynamic pressure. The local magnetic field appearing in (2.1) differs from the applied field $\mathbf{H}_0$ by a demagnetizing field of the polarized ferrofluid $\mathbf{H} = \mathbf{H}_0 + \mathbf{H}_d$, where $\mathbf{H}_d = -\nabla\varphi$, and φ is a scalar magnetic potential. Notice that since the applied field is spatially uniform it eventually drops out in the calculation of the magnetic term in (2.1), and the magnetic effects are due to the demagnetizing field.

As commented earlier we consider that the magnetization of the magnetic fluid in a uniform magnetic field is both uniform and constant, an assumption first introduced by Cebers and Maiorov [16]. This corresponds to method *C* in Ref. [64], where the validity of the constant magnetization hypothesis has been examined. We emphasize that although the magnetization is assumed to be uniform, the demagnetizing field is not. It is precisely this shape dependent demagnetizing field contribution (the so-called "fringing field") that gives rise to the fingering

instabilities in this model (see, for instance, Refs. [17, 63]). The influence of the constant magnetization approximation on the nature of the flat-deformed interface transition is discussed in Ref. [65] for the ferrofluid labyrinthine pattern formation case.

Equation (2.1) can be conveniently rewritten as

$$\mathbf{v}_j = -\frac{b^2}{12\eta_j}\nabla\left\{p_j + \mu_0\frac{M}{b}\int_{-b/2}^{+b/2}\frac{\partial\varphi}{\partial y}dz + \rho_j g y\right\} \tag{2.2}$$

where

$$\varphi = \frac{1}{4\pi}\int_{\mathscr{S}}\frac{\mathbf{M}\cdot\mathbf{n}'}{|\mathbf{r}-\mathbf{r}'|}d^2r' = \frac{1}{4\pi}\int_{-\infty}^{+\infty}\int_{-b/2}^{+b/2}\frac{M\hat{\mathbf{y}}\cdot\mathbf{n}'\,dx'dz'}{\sqrt{(x-x')^2+(y-y')^2+(z-z')^2}}. \tag{2.3}$$

The unprimed coordinates $\mathbf{r}$ denote arbitrary points in space, and the primed coordinates $\mathbf{r}'$ are integration variables within the magnetic domain $\mathscr{S}$, and $d^2r' = dx'dz'$ denotes the infinitesimal area element. The vector $\mathbf{n}'$ represents the unit normal to the magnetic domain in consideration. In Eq. (2.2) the velocity depends on a linear combination involving gradients of hydrodynamic pressure, magnetic potential, and gravity term, so we may think of the term between curly brackets as an effective pressure.

From Eq. (2.2) and the incompressibility condition $\nabla\cdot\mathbf{v}_j = 0$ it can be verified that the velocity potential ϕ_j ($\mathbf{v}_j = -\nabla\phi_j$) obeys Laplace's equation. The problem is then specified by the augmented pressure jump boundary condition at the interface

$$p_1 - p_2 = \sigma\kappa - \frac{1}{2}\mu_0(\mathbf{M}\cdot\mathbf{n})^2, \tag{2.4}$$

plus the kinematic boundary condition, which states that the normal components of each fluid's velocity are continuous at the interface

$$\mathbf{n}\cdot\nabla\phi_1 = \mathbf{n}\cdot\nabla\phi_2. \tag{2.5}$$

The first term on the right-hand side of Eq. (2.4) represents the usual contribution related to surface tension and interfacial curvature κ. The second term is the so-called magnetic normal traction [14, 15], which considers the influence of the normal component of the magnetization at the interface. For the current field configuration this magnetic piece is at least of second-order in the interface perturbation ζ, being legitimately nonlinear. The magnetic traction term will have a key role in determining the shape of the emerging interfacial patterns at the onset of nonlinear effects.

We proceed by following standard steps performed in weakly nonlinear studies [60, 61]. First, Fourier expansions are defined for the velocity potentials, and then boundary conditions (2.4) and (2.5) are used to express ϕ_j in terms of ζ_k consistently up to second-order. By substituting these relations in Eq. (2.2), and Fourier transforming, yields a dimensionless mode coupling equation for the system (for $k \neq 0$)

$$\dot{\zeta}_k = \lambda(k)\zeta_k + \sum_{k' \neq 0} [F(k,k')\ \zeta_{k'}\zeta_{k-k'} + G(k,k')\ \dot{\zeta}_{k'}\zeta_{k-k'}], \tag{2.6}$$

where

$$\lambda(k) = |k| \left[N_B W(k) - N_G - k^2 \right] \tag{2.7}$$

denotes the linear growth rate. The parameter

$$N_B = \frac{\mu_0 M^2 b}{\sigma} \tag{2.8}$$

represents a magnetic Bond number, and measures the ratio of magnetic to capillary forces. Likewise,

$$N_G = \frac{(\rho_1 - \rho_2) g b^2}{\sigma} \tag{2.9}$$

defines a gravitational Bond number, and measures the importance of gravitational force rela-

tive to the surface tension. In addition,

$$W(k) = \frac{1}{\pi} \int_0^\infty \left(\frac{\sin \tau}{\tau} \right)^2 [\sqrt{(k/2)^2 + \tau^2} - \tau] \, d\tau \tag{2.10}$$

is clearly a positive quantity, and originates from the contribution of the demagnetizing field.

The second-order mode coupling terms are given by

$$F(k,k') = \frac{N_B}{2} |k| k' (k - k'), \tag{2.11}$$

$$G(k,k') = A|k|[\mathrm{sgn}(kk') - 1]. \tag{2.12}$$

The sgn function equals ± 1 according to the sign of its argument, and the viscosity contrast is defined as $A = (\eta_1 - \eta_2)/(\eta_1 + \eta_2)$. In Eqs. (2.6)-(2.12) lengths and velocities are rescaled by b, and $\sigma/[12(\eta_1 + \eta_2)]$, respectively. We focus on the situation in which $\rho_1 > \rho_2$, and $\eta_1 \gg \eta_2$, so that the fluid-fluid interface is gravitationally stable ($N_G > 0$) and $A \approx 1$. This is done to allow a more direct connection with existing experiments [58, 59] where $\eta_1 \gg \eta_2$. As a matter of fact, the second-order results presented in the rest of this section remain practically unchanged as A is modified.

It is worth noting that the coupling term (2.11) comes from magnetic normal traction contribution in the pressure jump condition (2.4). This is exactly the term that is responsible for the development of peaked ferrofluid patterns already at second-order. Observe that there is no demagnetizing field contribution at second-order. We stress that the theoretical results presented in the following sections utilize dimensionless quantities which are extracted from the realistic physical parameters used in the experiments of Ref. [59].

2.1.2 Pattern morphology and nonlinear stability of stationary patterns

Before examining how we can use the mode coupling equation (2.6) to access purely nonlinear aspects related to the morphology of the interface, we briefly discuss a few useful concepts associated with the linear growth rate (2.7). Since a positive $\lambda(k)$ leads to an unstable

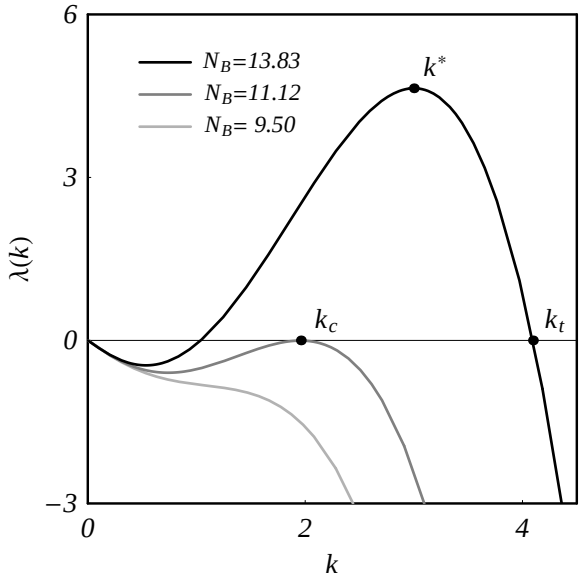

Figure 2.2: Linear growth rate $\lambda(k)$ as a function of the wave number k for $N_G = 1.44$, and three different values of the magnetic Bond number N_B. The critical (k_c), fastest growing (k^*), and threshold (k_t) wave numbers are also indicated. The critical magnetic Bond number is $N_B = 11.12$.

behavior, Eq. (2.7) tells us that the magnetic terms N_B and $W(k)$ are destabilizing. On the other hand, gravity and surface tension try to stabilize interfacial disturbances. The interplay of these competing effects determines the linear stability of the flat interface. This is illustrated in Fig. 2.2 which plots $\lambda(k)$ in terms of k, for $N_G = 1.44$, and three increasingly larger values of the magnetic Bond number. It is clear from Fig. 2.2 that the transition from a stable to an unstable situation occurs if both of the following conditions are met

$$\lambda(k) = 0, \text{ and } \frac{\partial \lambda(k)}{\partial k} = 0.$$

This defines a critical wave number k_c and a critical magnetic Bond number at which this exchange of stability takes place. Thus, when N_B is increased from zero, the interface remains flat over a range of values of N_B up to a point when transition suddenly occurs ($N_B = 11.12$), and a line of peaks with $k = k_c$ is formed. This is in fact what is observed experimentally [58,

59]. Note that the experimental investigation performed in Ref. [58] reveals the emergence of nonzero height peaks at the critical field, and a hysteresis phenomenon is observed. However, this effect is not contemplated by our analytical model, and also not detected in Ref. [59].

For larger N_B two other quantities of interest can be defined for a range of wave numbers over which $\lambda(k) \geq 0$ (see Fig. 2.2): k^*, the wave number of the fastest growing mode, maximizes $\lambda(k)$; k_t, the threshold wave number beyond which all modes are stable, is the largest wave number for which $\lambda(k)$ vanishes. As N_B grows, k^* and k_t shift to the right and modes of higher wave number become unstable.

At this point, we turn our attention to the weakly nonlinear, intermediate stages of pattern evolution, and use the equation of motion (2.6) to investigate how the magnetic field influences the shape of the fingering patterns at the onset of nonlinear effects. Inspired by an approach originally proposed in Refs. [60, 61], we focus on a mechanism controlling the finger shape behavior through magnetic means, and consider the coupling of a small number of modes. For a given N_B larger than the critical value, only discrete modes multiple of k^* are selected. In this framework, we examine the interaction of the fundamental mode with its own harmonic. For the rest of this section, we consider N_B above the critical situation, and take the fundamental wave number $k = k^*$ as the fastest growing mode. Consequently, the harmonic mode $2k^*$ always lies to the right of the threshold wave number k_t. Therefore, the harmonic is always linearly stable against growth.

As extensively discussed in Refs. [24, 60, 61] when one considers the second-order coupling of just two modes (i.e., the fundamental and its harmonic) one finds that the presence of the fundamental naturally forces growth of the harmonic mode through a nonlinear driven term in the mode coupling equations. The interesting point is that the sign of such nonlinear driven term dictates whether fingertip sharpening or fingertip broadening is favored by the dynamics. If the nonlinear term is positive, the harmonic mode is driven positive, the sign that is required to cause upward pointing fingers to become sharp, favoring fingertip sharpening. In contrast, if the nonlinear coupling term is negative, growth of a negative harmonic is favored, leading to upward-pointing fingertip broadening. Based on this mechanism the finger shape behavior of confined fluid systems can be described in a very simple manner.

It turns out that the ferrofluid finger tip-sharpening behavior observed experimentally in Refs. [58, 59] can be described by the mechanism mentioned above. The justification is that finger tip-sharpening requires the growth of a sizable harmonic mode. Of course, this cannot be achieved through a purely linear description. However, by inspecting Eq. (2.6), we note that the second-order term $F(n,n')$, which is reminiscent of the magnetic normal traction contribution in (2.4), does involve magnetic field effects. This term drives growth of the harmonic mode (with the phase appropriate to sharpen finger tips) despite its linear stability, leading to the development of peaked ferrofluid structures already at second-order.

Considering such a mechanism our aim is to illustrate the time evolution of the interface and the occurrence of ferrofluid finger tip-sharpening. It is convenient for the subsequent discussions to consider cosine $a_k = \zeta_k + \zeta_{-k}$ and sine $b_k = i(\zeta_k - \zeta_{-k})$ modes, rather than the complex modes employed in Eq. (2.6). Describing the fundamental as a cosine mode with positive amplitude, we only need to examine the harmonic cosine mode to analyze finger tip behavior and pattern morphology. Under such circumstances, the evolving interface can be described as $\zeta(x,t) = a_k(t)\cos kx + a_{2k}(t)\cos 2kx$, where the perturbation amplitudes $a_k(t)$ and $a_{2k}(t)$ are obtained from the second-order solution of the mode coupling Eq. (2.6). Specifically, one needs to solve the following coupled nonlinear differential equations

$$\dot{a}_{2k} \;=\; \lambda(2k)a_{2k} + \frac{1}{2}[F(2k,k)a_k + G(2k,k)\dot{a}_k]\; a_k, \tag{2.13}$$

$$\dot{a}_k = \lambda(k)a_k + \frac{1}{2}[F(k,-k)a_k + G(k,-k)\dot{a}_k]\; a_{2k} + \frac{1}{2}[F(k,2k)a_{2k} + G(k,2k)\dot{a}_{2k}]\; a_k. \tag{2.14}$$

By solving Eqs. (2.13) and (2.14) the interface evolution is plotted in Fig. 2.3 for $N_G = 1.44$, $N_B = 13.83$, $k^* = 3$, and considering initial conditions $a_k(0) = 0.0001$, and $a_{2k}(0) = 0$. Note that the harmonic mode is absent initially. The times shown are $t = 0.8, 1.2,$ and 2. The resulting patterns reveal the emergence of increasingly sharp, peaked structures of the ferrofluid

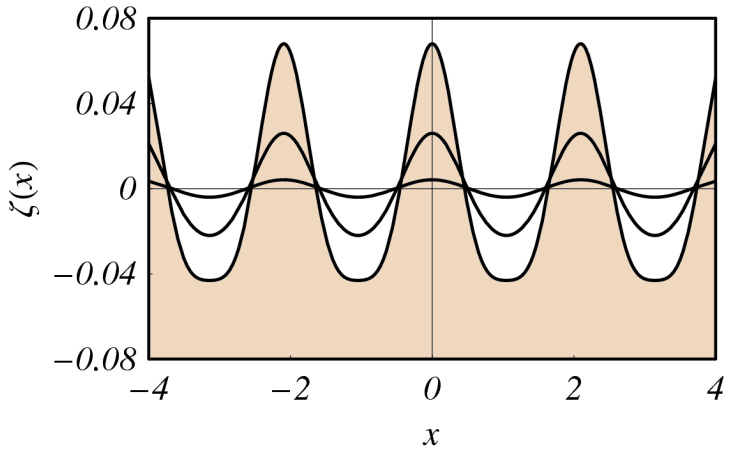

Figure 2.3: Time evolution of the interface shape. The shaded region represents the ferrofluid pattern morphology at time $t = 2$. The interface profile for $t > 2$ is indistinguishable from the one shown at $t = 2$.

penetrating the nonmagnetic fluid. As time increases the downward moving fingers of the upper fluid look wider and flatter at their extremities, getting closer to the stationary shape already revealed at $t = 2$ (shaded region in Fig. 2.3). This characteristic shape is consistent with the experimental patterns exhibited in Refs. [58, 59], and also with the purely static profiles obtained theoretically in Ref. [52]. It is also worthwhile to note that the interface profiles obtained for $t > 2$ lie on top of the curve plotted at time $t = 2$ signalizing that a steady state has been reached. Considering the simplicity of our analytical approach (lowest-order nonlinear coupling of just two Fourier modes), as expected we find that a precise quantitative agreement between our theoretical shapes and the experimental profiles is not observed. However, the main morphological features of the real ferrofluid patterns can be indeed predicted and satisfactorily depicted by our mode coupling theory.

Complementary information about the pattern-forming phenomenon depicted in Fig. 2.3 is provided by Fig. 2.4 which plots the time evolution of the cosine perturbation amplitudes a_k and a_{2k}. We clearly observe that the weakly nonlinear coupling dictates naturally the enhanced growth of a positive harmonic mode, precisely the phase that is required to produce finger tip-sharpening. It is also evident that after an initial period of growth both perturbation amplitudes

saturate, so that they remain unchanged as time progresses. This confirms the idea that the system tends to a steady state configuration.

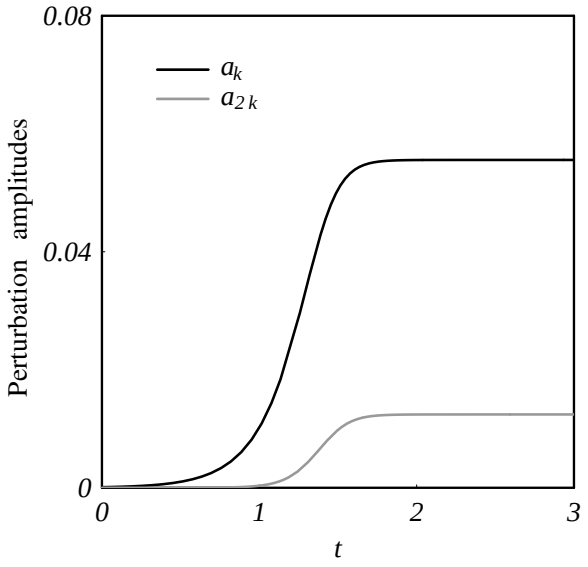

Figure 2.4: Time evolution of the perturbation amplitudes $a_k(t)$ and $a_{2k}(t)$ for the evolving interface depicted in Fig. 2.3. It is clear that both amplitudes eventually tend to stationary values.

The nontrivial stationary cosine amplitudes for the harmonic (a_{2k}^{st}) and fundamental (a_k^{st}) can be obtained analytically by setting their time derivative terms to zero in the mode coupling equations (2.13) and (2.14), yielding

$$a_{2k}^{st} = \frac{-2\lambda(k)}{[F(k,-k)+F(k,2k)]}, \tag{2.15}$$

$$a_k^{st} = \sqrt{\frac{4\lambda(2k)\lambda(k)}{F(2k,k)[F(k,-k)+F(k,2k)]}}, \tag{2.16}$$

where

$$F(k,-k)+F(k,2k) = -2N_B k^2|k| < 0,$$

$$F(2k,k) = N_B k^2 |k| > 0,$$

$$\lambda(k) > 0, \text{ and } \lambda(2k) < 0.$$

It is reassuring to observe that a_{2k}^{st} is a genuinely positive quantity.

We close this section by examining the stability of the stationary solutions. In fact, we have verified that the steady solution given by Eqs. (2.15) and (2.16) is stable. This is done by considering the nonlinear differential equations (2.13) and (2.14). Through a standard linearization process close to the stationary solution, we diagonalize the resulting system of equations, determining the eigenvalues which dictate the stability of the fixed point [66]

$$\varepsilon_{\pm} = \frac{\lambda(2k)}{2}\left\{1 \pm \sqrt{1 + \frac{16k^2 N_B \lambda(k)}{\lambda(2k)[\lambda(k) + 2k^2 N_B]}}\right\}. \tag{2.17}$$

For the stationary solution under consideration both eigenvalues have negative real parts, characterizing a stable node or spiral. Regardless of the initial conditions for the perturbation amplitudes the system asymptotically approaches the stable fixed point. It is worth pointing out that this is in contrast with the typical unstable behavior exhibited by other steady (nonzero surface tension) solutions obtained for nonmagnetic [67, 68] and magnetic [24, 40, 41] fluids in Hele-Shaw cells. We also find that the unperturbed (flat) interface is a saddle point, and therefore unstable.

2.2 Nonlinear traveling waves in confined ferrofluids

Frontal fluid flows in the confined geometry of a Hele-Shaw cell have been plentifully investigated during the last five decades. Under frontal flow, the motion of the fluids is normal to the initially undisturbed interface between them, and might lead to the formation of viscous fingering phenomena [1, 2]. Curiously, the related problem of fluids flowing parallel to their

separating interface, and the development of interfacial traveling waves in the Hele-Shaw setup has been much less exploited in the literature [69, 70, 71, 72]. Zeybek and Yortsos [69, 70] studied parallel flow in a horizontal Hele-Shaw cell. In the limit of large capillary numbers and large wavelength they have found Korteweg-de Vries (KdV) dynamics leading to stable finite amplitude soliton solutions. Afterward, Gondret, Rabaud, and co-workers [71, 72] examined, through experiments and theory, the appearance of traveling waves for parallel flow in a vertical Hele-Shaw cell. They have observed that the interface is destabilized above a certain critical flow velocity, so that waves grow and propagate along the cell. Such waves are initially sinusoidal then turn to localized structures presenting a nonlinear shape.

The theoretical model presented in Ref. [71] was based on a modified Darcy equation for the gap-averaged flow with an additional term representing inertial effects. Within this context a Kelvin-Helmholtz instability for inviscid fluids has been found. For viscous fluids they derived a Kelvin-Helmholtz-Darcy equation and verified that the threshold for instability was governed by inertial effects, while the wave velocity was determined by the Darcy's law flow of viscous fluids. Their theoretical analysis has been backed up by their own experimental results. Theoretical improvements in the description of the system have been proposed in Refs. [73, 74, 75] where the gap-averaged approach utilized in [71] has been replaced by an alternative scheme directly based on the fully three-dimensional Navier-Stokes equation. In the end, the calculations in Refs. [73, 74, 75] lead to an equation of motion similar to the one derived in [71], but with slightly different coefficients.

One additional example of parallel flow in vertical Hele-Shaw cells is the linear stability analysis performed by Miranda and Widom [76]. The major difference between their work and the ones performed in Refs. [69, 70, 71, 72, 73, 74, 75] is the fact that one of the fluids is a ferrofluid [14, 15], and that an external magnetic field is applied. The field could lie in the plane of the Hele-Shaw cell, either tangential or normal to the fluid-fluid interface. A ferrofluid behaves as a regular viscous fluid except that it can experience forces due to magnetic polarization [77]. This opens up the possibility of investigating the role played by the magnetic field in the dynamics of the parallel flow. It has been shown [76] that the dispersion relation governing mode growth is modified so that the magnetic field can destabilize the interface even

in the absence of inertial effects. However, it has been deduced that the magnetic field would not affect the speed of wave propagation. Despite all that, a study addressing the effect of the magnetic field on the morphological structure and nonlinear evolution of the propagating waves is still lacking.

In this section we re-examine the problem initially proposed in Ref. [76] by considering the action of an in-plane, tilted applied magnetic field which makes an arbitrary angle with the direction defined by the unperturbed fluid-fluid interface. This apparently naive modification proves to be crucial in creating a connection between the applied field and the propagating wave velocity. Moreover, in contrast to what was done in [76] we go beyond the linear regime, and tackle the problem by using a perturbative weakly nonlinear approach. This particular theoretical tool enables one to extract valuable analytical information at the onset of nonlinearity. As a consequence, one can investigate the influence of the magnetic field on the nonlinear dynamics and ultimate shape of the traveling surface waves.

The layout of this section is as follows. Section 2.2.1 introduces the governing equations of the parallel flow system with a ferrofluid, and presents our mode-coupling approach which is valid at lowest nonlinear perturbative order [60, 61]. Linear and weakly nonlinear dynamics are discussed in Secs. 2.2.2 and 2.2.3. We show that the effect of the magnetic field on the velocity and shape of the propagating waves can be accessed by considering the interplay of a small number of Fourier modes. One important result is the feasibility of sustaining, moving, and controlling a traveling wave solely under the action of an external magnetic field. Stationary wave profiles are found for different values of the magnetic field tilting angle. Our main conclusions are summarized in Sec. 6.1.

2.2.1 Governing equations and analytical calculations

Consider two semi-infinite immiscible viscous fluids, flowing with velocities U_j where $j = 1$ ($j = 2$) labels the lower (upper) fluid. The flow takes place along the x direction in a vertical Hele-Shaw cell of thickness b (Fig. 2.5). The densities and viscosities of the fluids are denoted respectively as ρ_j, and η_j. The cell lies parallel to the xy plane, where the y axis is vertically

upward. Between the fluids there exists a surface tension σ, and the lower fluid is assumed to be a ferrofluid (magnetization **M**), while the upper fluid is nonmagnetic (zero magnetization). Acceleration of gravity $\mathbf{g} = -g\hat{\mathbf{y}}$, where $\hat{\mathbf{y}}$ is the unit vector in the y-axis. The base flow is horizontal with $\eta_1 U_1 = \eta_2 U_2$ [71] because the flows in the two fluids are driven by the same pressure gradient.

A uniform external magnetic field $\mathbf{H}_0 = H_0(\cos\alpha\ \hat{\mathbf{x}} + \sin\alpha\ \hat{\mathbf{y}})$ is applied in the plane of the cell. The shape of the perturbed fluid-fluid interface is described as $\mathscr{I}(x,y,t) = y - \zeta(x,t) = 0$, where $\zeta(x,t) = \sum_{k=-\infty}^{+\infty} \zeta_k(t)\exp(ikx)$ represents the net interface perturbation with Fourier amplitudes $\zeta_k(t)$, and wave numbers k.

For the quasi two-dimensional (2D) geometry of the Hele-Shaw cell, the 3D fluid flow is reduced to an equivalent 2D one by averaging the Navier-Stokes equation over the direction perpendicular to the plates. Using no-slip boundary conditions and neglecting inertial terms, the flow in such a confined environment is governed by the modified Darcy's law in Eq. (2.1).

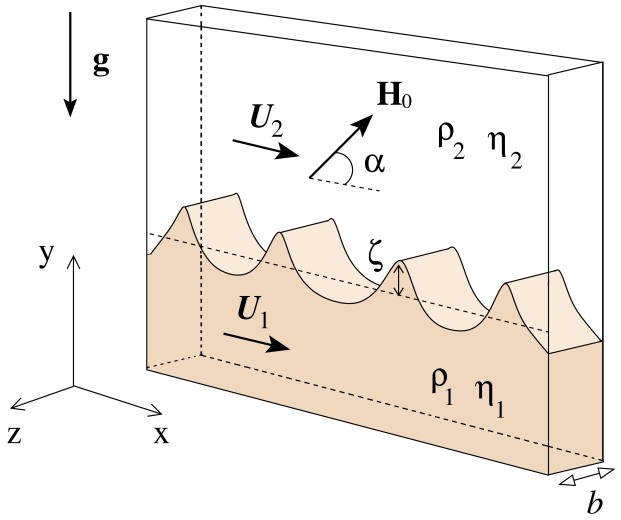

Figure 2.5: Schematic configuration of the parallel flow in a vertical Hele-Shaw cell. The lower fluid is a ferrofluid, while the upper fluid is nonmagnetic. An external uniform magnetic field $\mathbf{H}_0$ is applied making an angle α with the initially undisturbed interface separating the fluids.

The role of inertia in the problem can be quantified by a Reynolds number (relative measure of inertial and viscous forces) which is directly proportional to the cell gap thickness, and in-

versely proportional to the viscosity of fluid, $\mathrm{Re}_j = (\rho_j U_j b)/(12\eta_j)$. Since most experimental and theoretical studies of ferrofluid flow in Hele-Shaw cells deal with very thin cell gaps and highly viscous fluids, the vanishing Reynolds number limit is readily validated. Under such circumstances, the fluid motion is perfectly described by the gap-averaged modified Darcy's law (2.1). As discussed in Refs. [71, 78, 79] in unidirectional Hele-Shaw parallel flow, the inertial effects can be neglected, even at relatively large Reynolds numbers as long as $\mathrm{Re}_j < \mathrm{Re}_c$, where Re_c is the Reynolds number corresponding to the laminar-turbulent transition.

We follow the standard approximations used in the previous section and assume that the magnetization is collinear with the applied field $\mathbf{M}(\mathbf{H}) = M(\cos\alpha\ \hat{\mathbf{x}} + \sin\alpha\ \hat{\mathbf{y}})$, where $M = M(H_0)$. Only the lowest order effect of the magnetic interactions that would result in fluid motion is considered. We emphasize that although the magnetization is taken to be uniform, the demagnetizing field is not.

Taking into consideration the physical assumptions mentioned above, and the particular geometry of our system Eq. (2.1) can be rewritten as

$$\mathbf{v}_j = -\frac{b^2}{12\eta_j}\nabla\left\{ p_j + \rho_j g y + \mu_0 \frac{M}{b}\int_{-b/2}^{+b/2}\left[\cos\alpha\frac{\partial\varphi}{\partial x} + \sin\alpha\frac{\partial\varphi}{\partial y}\right] dz \right\}, \tag{2.18}$$

where

$$\begin{aligned} \varphi &= \frac{1}{4\pi}\int_{\mathscr{S}} \frac{\mathbf{M}\cdot\mathbf{n}'}{|\mathbf{r}-\mathbf{r}'|} d^2r' \\ &= \frac{1}{4\pi}\int_{-\infty}^{+\infty}\int_{-b/2}^{+b/2} \frac{M(\cos\alpha\ \hat{\mathbf{x}} + \sin\alpha\ \hat{\mathbf{y}})\cdot\mathbf{n}'\, dx'dz'}{\sqrt{(x-x')^2+(y-y')^2+(z-z')^2}}. \end{aligned} \tag{2.19}$$

The unprimed coordinates $\mathbf{r}$ denote arbitrary points in space, and the primed coordinates $\mathbf{r}'$ are integration variables within the magnetic domain $\mathscr{S}$, and $d^2r' = dx'dz'$ denotes the infinitesimal area element. The vector $\mathbf{n}'$ represents the unit normal to the magnetic domain under study.

By inspecting Eq. (2.18) we observe that the velocity depends on a linear combination involving gradients of hydrodynamic pressure, gravity, and magnetic potential, respectively.

So, the term between curly brackets in (2.18) can be seen as an effective pressure. Therefore, as in the Hele-Shaw problem with nonmagnetic fluids [1, 2], the flow is potential, $\mathbf{v}_j = -\nabla\phi_j$, but now with a velocity potential given by

$$\phi_j = \frac{b^2}{12\eta_j}\left\{p_j - \mu_0 M^2 I(x,y) + \rho_j g y\right\}, \tag{2.20}$$

where

$$I(x,y) = \frac{1}{4\pi b}\int_{-\infty}^{+\infty}\int_{-b/2}^{+b/2}\int_{-b/2}^{+b/2} \frac{\left[-\cos\alpha\ \frac{\partial\zeta(x')}{\partial x'} + \sin\alpha\right]}{\sqrt{1+\left(\frac{\partial\zeta(x')}{\partial x'}\right)^2}} \times \frac{\left[\cos\alpha\ (x-x') + \sin\alpha\ (y-\zeta(x'))\right]\, dx'dz'dz}{\sqrt{(x-x')^2+(y-\zeta(x'))^2+(z-z')^2}}. \tag{2.21}$$

In Eq. (2.21) the integral in dz is related to the gap-average calculation [see Eq. (2.18)], while the integrals in dx' and dz' come from the surface integral in the magnetic domain of interest $\mathscr{S}$ [see Eq. (2.19)]. Notice that incompressibility ($\nabla\cdot\mathbf{v}_j = 0$) then yields Laplace's equation for the velocity potential.

The problem is specified by the two boundary conditions given by Eqs. (2.4) and (2.5). Equation (2.4) is an augmented pressure jump condition at the interface, where κ denotes the interfacial curvature. A crucial difference of this expression from the one utilized in the non-magnetic situation is given by the second term on the right-hand side: the so-called magnetic normal traction [14, 15] which considers the influence of the normal component of the magnetization at the interface. For the current field configuration this magnetic piece is at least of second-order in ζ, being legitimately nonlinear. This magnetic term contributes to determine the shape of the traveling wave profiles at the onset of nonlinear effects. The second boundary condition (2.5) simply states the continuity of the normal flow velocity at the interface.

Our next task is to derive an equation of motion for the perturbation amplitudes which is able to capture the essential physics at the lowest nonlinear level. This is done by following standard steps performed in previous weakly nonlinear studies [38, 60, 61]. First, we define

Fourier expansions for the velocity potentials. Then, we express ϕ_j in terms of the perturbation amplitudes ζ_k by considering the kinematic boundary condition (2.5). Substituting these relations, and the modified pressure jump condition Eq. (2.4) into Eq. (2.20), always keeping terms up to second-order in ζ, and Fourier transforming, we find the dimensionless equation of motion (for $k \neq 0$)

$$\begin{aligned} \dot{\zeta}_k &= \Lambda(k)\zeta_k \\ &+ \sum_{k' \neq 0} [F(k,k')\ \zeta_{k'}\zeta_{k-k'} + G(k,k')\ \dot{\zeta}_{k'}\zeta_{k-k'}], \end{aligned} \tag{2.22}$$

where the overdot denotes total time derivative,

$$\Lambda(k) = \lambda(k) - ik\left[c_0 + N_B|k|\frac{\sin 2\alpha}{2}\right] \tag{2.23}$$

is a complex linear growth rate, and

$$\begin{aligned} \lambda(k) &= |k|\{N_B[\sin^2\alpha\ W_1(k) - \cos^2\alpha\ W_2(k)] \\ &- k^2 - N_G\} \end{aligned} \tag{2.24}$$

is its real part.

The system is characterized by three dimensionless parameters

$$\begin{aligned} N_B &= \frac{\mu_0 M^2 b}{\sigma},\ N_G = \frac{(\rho_1 - \rho_2)gb^2}{\sigma},\ \text{and} \\ c_0 &= \frac{12(\eta_1 U_1 + \eta_2 U_2)}{\sigma}. \end{aligned}$$

The magnetic Bond number N_B measures the ratio of magnetic to capillary forces, while the gravitational Bond number N_G accounts for the relative importance of gravitational force to the surface tension. The parameter c_0 represents the propagation contribution due to the parallel flow. Notice that c_0 can be seen as a modified capillary number $\mathrm{Ca} = \mathrm{Ca}_1 + \mathrm{Ca}_2$, where $\mathrm{Ca}_j =$

$12\eta_j U_j/\sigma$ is the capillary number of fluid j. In addition,

$$W_1(k) = \frac{1}{\pi}\int_0^\infty \frac{(1-\cos k\tau)}{\tau^2}[\sqrt{\tau^2+1}-\tau]\,d\tau, \tag{2.25}$$

and

$$W_2(k) = \frac{k}{\pi}\int_0^\infty \frac{\sin k\tau}{\tau}[\sqrt{\tau^2+1}-\tau]\,d\tau \tag{2.26}$$

originate from the contribution of the demagnetizing field.

The second-order mode-coupling terms are given by

$$\begin{aligned} F(k,k') &= N_B|k|\frac{k'(k'-k)}{2}\Bigg\{\cos 2\alpha \\ &+ i\sin 2\alpha\left[\frac{W_1(k')}{k'}-\frac{W_2(k)}{2k}+\frac{W_3(k,k')}{k'(k'-k)}\right]\Bigg\}, \end{aligned} \tag{2.27}$$

and

$$G(k,k') = A|k|[\mathrm{sgn}(kk')-1], \tag{2.28}$$

where

$$\begin{aligned} W_3(k,k') = \frac{1}{\pi}\int_0^\infty &[\sin k\tau-\sin k'\tau-\sin(k-k')\tau] \\ &\times\left\{\frac{[\sqrt{\tau^2+1}-\tau]}{\tau^4}+\frac{1}{2\tau}\left[\frac{1}{\tau}-\frac{1}{\sqrt{\tau^2+1}}\right]\right\}d\tau \end{aligned} \tag{2.29}$$

is another demagnetizing integral. Notice the presence of the imaginary part in (2.27), that is proportional to N_B and $\sin 2\alpha$, and would vanish for a purely vertical or horizontal magnetic field. The sgn function equals ± 1 according to the sign of its argument, and the viscosity contrast is defined as $A = (\eta_1-\eta_2)/(\eta_1+\eta_2)$. In Eqs. (2.22)-(2.29) lengths and velocities are rescaled by b, and $\sigma/[12(\eta_1+\eta_2)]$, respectively. Without loss of generality we focus on the situation in which $\rho_1 > \rho_2$, and $\eta_1 \gg \eta_2$, so that the interface is gravitationally stable

($N_G > 0$) and $A \approx 1$. Since the gravitational Bond number plays a minor role to our analysis, for the rest of this section we fix its value as $N_G = 1.4$. We recover the results for the vertical magnetic field configuration without flow, previously studied in Ref. [38], by setting $\alpha = \pi/2$ and $c_0 = 0$. It should be noted that the theoretical results presented in the following section utilize dimensionless quantities which are extracted from the realistic physical parameters used in the experiments of Refs. [71] and [59].

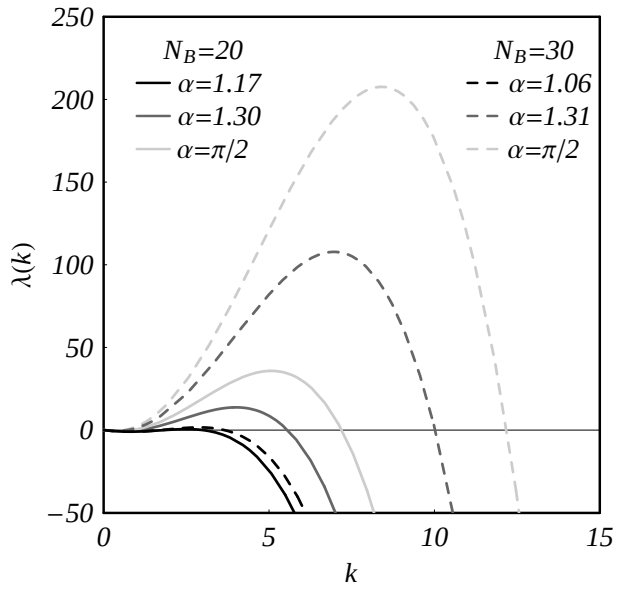

Figure 2.6: The real part of the linear growth rate $\lambda(k)$ as a function of the wave number k for $N_G = 1.4$. Continuous (dashed) curves refer to $N_B = 20$ ($N_B = 30$). For each N_B we plot curves for three values of the angle α, where lighter gray curves correspond to higher values of α.

2.2.2 Linear regime

Before examining how we can use the mode-coupling equation (2.22) to access important nonlinear aspects related to the traveling waves, we briefly discuss a few useful concepts associated with the linear growth rate (2.23). The real part of the growth rate $\mathrm{Re}[\Lambda(k)] = \lambda(k)$ governs the exponential growth or decay of the wave amplitudes at the linear regime. Since a positive $\lambda(k)$ leads to an unstable behavior, Eq. (2.24) tells us that the term $W_1(k)$ [$W_2(k)$],

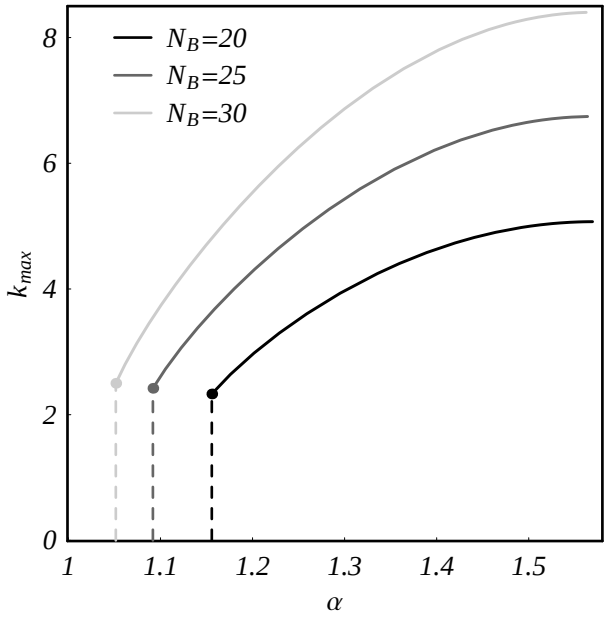

Figure 2.7: Dominant wave number k_{max} as a function of the angle α for $N_G = 1.4$ and three different values of N_B. The dots indicate the critical values of α below which the interface is stable.

proportional to N_B and representing the contribution of the vertical (horizontal) magnetic field component, is destabilizing (stabilizing). On the other hand, gravity and surface tension try to stabilize interfacial disturbances. The interplay of these competing effects determines the linear stability of the initially flat fluid-fluid interface. This is illustrated in Fig. 2.6 which plots $\lambda(k)$ in terms of k, for two values of N_B, and three increasingly larger values of the angle α. By inspecting Eq. (2.24) it is clear that the magnetic field (demagnetizing field contribution) causes the instability, even in the absence of inertial effects [38, 76].

It is clear from Fig. 2.6 that, for a given magnetic Bond number and by increasing α, the transition from a stable to an unstable situation occurs when $\lambda(k) = 0$ and $d\lambda(k)/dk = 0$, what defines a critical value for α. Moreover, the maximum of $\lambda(k)$ takes place at $k = k_{max}$, that characterizes the dominant wave number of the emergent pattern. It increases and moves towards higher values of k as α approaches $\pi/2$. The behavior of $\lambda(k)$ as a function of α is magnified by increasing N_B. We point out that, in order to observe any instability band, N_B

must be above the critical value given by the vertical field situation ($N_B > 11.12$) [38], as it was shown in Sec. 2.1.

The behavior of k_{max} as a function of α is depicted in Fig. 2.7. Here we see that as α approaches $\pi/2$ ($\alpha \approx 1.57$) k_{max} reaches a maximum possible value for a given N_B. The critical values of α are marked with dots and vertical dashed lines. By increasing the magnetic field the curves move upwards, and the critical values of α decrease.

The imaginary part of the growth rate (2.23), $\mathrm{Im}[\Lambda(k)]$, divided by $-k$ give us the phase velocity of perturbations at the linear regime. It presents a parallel flow contribution represented by c_0, and a magnetic one proportional to N_B that comes from the fact that the magnetic field has nonzero x and y components. This last term is very important for our analysis of propagating profiles, and would not be present if the magnetic field was simply vertical ($\alpha = \pi/2$) or horizontal ($\alpha = 0$) as considered in Ref. [76]. In order to detect any influence of the magnetic field on the phase velocity we must consider the interval between these two limiting situations ($0 < \alpha < \pi/2$). From these comments the key role played by the tilted magnetic field becomes evident: now one could have wave propagation even if $c_0 = 0$, and it would be exclusively due to magnetic effects.

2.2.3 Weakly nonlinear dynamics

At this point, we turn our attention to the weakly nonlinear, intermediate stages of interfacial pattern evolution. We use the equation of motion (2.22) to investigate how the magnetic field influences the shape and velocity of the propagating waves. We employ a theoretical approach originally proposed in Refs. [60, 61], and focus on a mechanism controlling the interface behavior through magnetic means. This is done by considering the coupling of a small number of modes. For a given α larger than the critical value, only discrete modes multiple of the dominant wave number k_{max} are selected due to translational invariance. In this framework, we examine the interaction of the fundamental mode k with its own harmonic $2k$. For the rest of this section, we consider values of α above the critical situation, and take the fundamental wave number $k = k_{max}$ as the fastest growing mode.

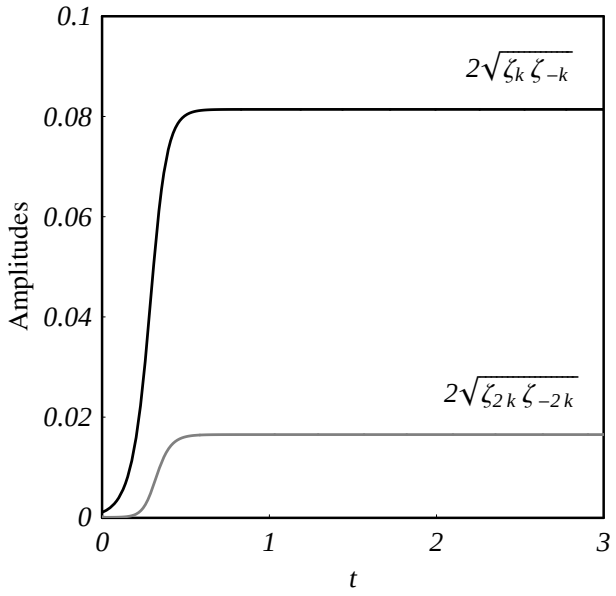

Figure 2.8: Numerical time evolution of the absolute value of the perturbation amplitudes for the fundamental mode ($2\sqrt{\zeta_k\zeta_{-k}}$) and its first harmonic ($2\sqrt{\zeta_{2k}\zeta_{-2k}}$). The parameters considered correspond to the continuous dark gray curve in Fig. 2.6 ($N_G = 1.4$, $c_0 = 0.5$, $N_B = 20$ and $\alpha = 1.30$). As time grows, the amplitudes tend to saturate and reach stationary values indicating the propagation of an unchanged shape profile.

Considering these two modes the moving interface profile can be described as

$$\begin{aligned}\zeta(x,t) &= \zeta_k(t)\exp(ikx)+\zeta_{-k}(t)\exp(-ikx)\\ &+ \zeta_{2k}(t)\exp(2ikx)+\zeta_{-2k}(t)\exp(-2ikx),\end{aligned} \tag{2.30}$$

with ζ_k and ζ_{-k} (also ζ_{2k} and ζ_{-2k}) being complex conjugates. Specifically, one needs to solve the following coupled nonlinear differential equations

$$\dot{\zeta}_{2k} = \Lambda(2k)\zeta_{2k}+\left[F(2k,k)\zeta_k+G(2k,k)\dot{\zeta}_k\right]\,\zeta_k, \tag{2.31}$$

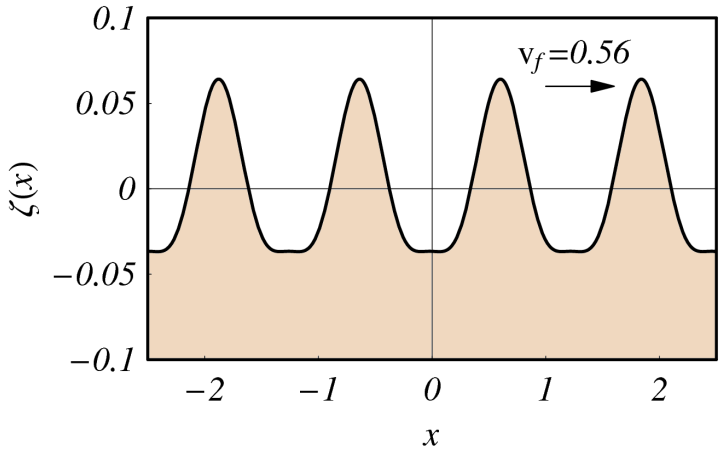

Figure 2.9: Propagating wave profile for $c_0 = 0.5$, $N_B = 20$ and $\alpha = \pi/2$, resulting in $v_f = 0.56$. The profile and velocity are reflected in relation to the y axis if we perform the transformation $c_0' = -c_0$.

$$\begin{aligned} \dot{\zeta}_k &= \Lambda(k)\zeta_k + [F(k,-k)\zeta_{-k} + G(k,-k)\dot{\zeta}_{-k}]\ \zeta_{2k} \\ &+ [F(k,2k)\zeta_{2k} + G(k,2k)\dot{\zeta}_{2k}]\ \zeta_{-k}. \end{aligned} \tag{2.32}$$

The interface evolution is obtained by numerically solving Eqs. (2.31) and (2.32). We have verified that the amplitudes and relative phase of the solutions saturate for later times, leading to stationary propagating profiles. Figure 2.8 shows the time evolution of the absolute value of the perturbation amplitudes. We consider very low initial amplitude values ($\zeta_k = 0.001$ and $\zeta_{2k} = 0.0001$) and parameters $N_G = 1.4$, $c_0 = 0.5$, $N_B = 20$ and $\alpha = 1.30$. This figure depicts the amplitudes evolution beginning from a nearly flat interface, exponentially growing at the linear stage, and then saturating at later times. So, after a transient period of growth the perturbation amplitudes remain unchanged as time progresses. The main difference from these findings and the results in Ref. [38] is the fact that here the saturated modes ζ_k and ζ_{2k} now maintain a locked phase difference between them, in such a way to lead to a steady profile propagation. It is also evident from Fig. 2.8 that the weakly nonlinear coupling naturally dictates the enhanced growth of a positive harmonic mode.

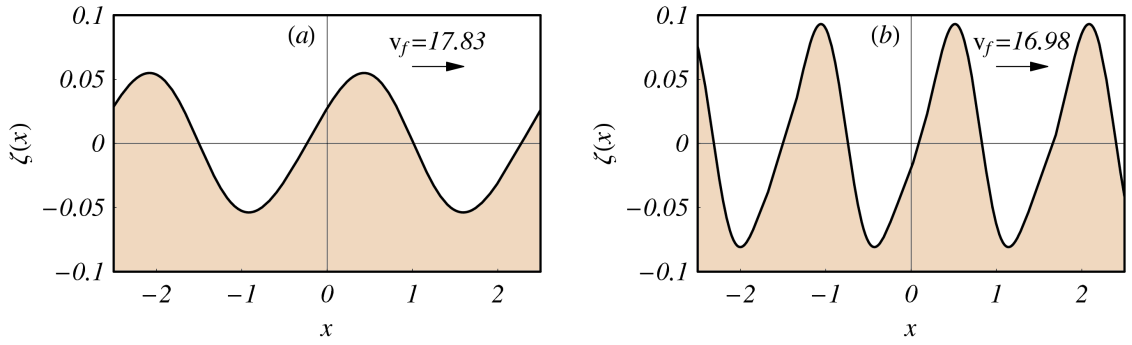

Figure 2.10: (a) Propagating wave profile for $N_B = 20$ and $\alpha = 1.17$, resulting in $v_f = 17.83$.(b) Propagating wave profile for $N_B = 20$ and $\alpha = 1.30$, resulting in $v_f = 16.98$. The profile and velocity are reflected in relation to the y axis if we perform the transformation $\alpha' = \pi - \alpha$. Note that here $c_0 = 0$.

An example of a steady propagating profile found numerically is plotted in Fig. 2.9 for $N_G = 1.4$, $c_0 = 0.5$, $N_B = 20$ and $\alpha = \pi/2$ ($k_{max} = 5.07$). Its real growth rate is represented by the light gray solid curve in Fig. 2.6. The resulting wave pattern shows a sequence of sharp peaked structures separated by wider troughs. These shapes are similar to the ones obtained in the situation in which there is no parallel flow, and the magnetic field is vertical [38]. There is little morphological difference produced by the introduction of the parallel flow, represented by a nonvanishing c_0, if $\alpha = \pi/2$, but now we have a propagating profile instead of a stationary one. We define v_f as the final propagation velocity of the saturated profile, which in Fig. 2.9 case equals 0.56. Note that v_f is not given solely by the linear phase velocity in (2.23), but it is a result of the weakly nonlinear coupling between the modes in the saturated regime.

Since c_0 has very little influence on the morphology of the rising wave patterns (independently of the angle α), we take c_0=0 in Fig. 2.10, and focus on the role of the magnetic field tilting angle α in determining the morphology of the propagating solutions. In practical terms, for finite surface tension flows, the limit $c_0 = 0$ can be obtained by setting the velocities $U_1 = U_2 = 0$. For α close to the critical value, as it is shown in Fig. 2.10(a), the solution is dominated by the fundamental mode and the shape of the profile resembles a pure propagating cosine wave. As α is increased, the wave morphology changes and we see a series of slightly inclined peaks, as exemplified in Fig. 2.10(b). This is possible due to the significant magnitude

of the first harmonic mode. For higher values of α we get peaked structures similar to the ones depicted in Fig. 2.9 (where $\alpha = \pi/2$). Notice that it is sufficient to explore the influence of the tilted magnetic field in the range $0 \leq \alpha \leq \pi/2$. This is justified by the fact that the propagating wave problem is reflected with relation to the y axis under the transformation $\alpha' = \pi - \alpha$, and it is symmetric under the transformation $\alpha' = \pi + \alpha$. Complementary information about the influence of α on the magnitude of the final propagating velocities will be exploited in the discussion of Fig. 2.11.

2.2.4 Analytical approach to steady solutions

In order to have a more quantitative account of the propagating steady profiles numerically predicted in Sec. 2.2.3, we now carry out an analytical study aiming to find wave solutions to our problem, and analyze their stability.

To obtain a steady propagating solution we impose that $\zeta(x,t) = \zeta(kx - \omega t)$, where ω is real and $\mathrm{v}_f = \omega/k$ is the final propagating velocity. Therefore, we can write $\zeta_k(t) = c_1 \exp(-i\omega t)$ and $\zeta_{2k}(t) = c_2 \exp(-i2\omega t)$ as propagating modes with constant amplitudes. We may take c_1 as a real constant without loss of generality, since an imaginary part of it would simply translate the resulting profile. However, we keep c_2 as a complex number, so there is a phase difference between the modes ζ_k and ζ_{2k}, something that is relevant for the profile morphology. By inserting these conditions into Eqs. (2.31) and (2.32) we get a complete set of nonlinear time-independent equations that determine c_1, c_2 and ω [see Eqs. (2.34) and (2.35) in Sec. 2.2.5].

By manipulating the equations of the system described above we find a cubic algebraic equation for ω with real coefficients that depends on the functions expressed by Eqs. (2.23)-(2.29). We have verified that within our range of physical parameters (taken from the experiments in Refs. [71] and [59]), this polynomial equation has a positive discriminant, and therefore, three different real roots are found (see Sec. 2.2.5 for details). To find out which of these solutions gives the actual propagating velocity we perform a stability analysis of the propagating solution by perturbing the modes' stationary amplitudes $\zeta_k(t) = (\varepsilon_1 + c_1)\exp(-i\omega t)$, and

$\zeta_{2k}(t) = (\varepsilon_2 + c_2)\exp(-i2\omega t)$, with $\varepsilon_1 = \varepsilon_1(t)$ real and $\varepsilon_2 = \varepsilon_2(t)$ complex. By inserting this conditions in Eqs.(2.31) and (2.32), and expanding up to first order in ε, the stability analysis of the solution leads to a set of equations that can be expressed in a matrix form as

$$\begin{pmatrix} \dot{\varepsilon}_1 \\ \dot{\varepsilon}_2 \end{pmatrix} = \begin{pmatrix} \mathscr{A}_{11} & \mathscr{A}_{12} \\ \mathscr{A}_{21} & \mathscr{A}_{22} \end{pmatrix} \begin{pmatrix} \varepsilon_1 \\ \varepsilon_2 \end{pmatrix}, \tag{2.33}$$

where

$$\begin{aligned} \mathscr{A}_{11} &= \frac{\Lambda(k) + i\omega + (F(k,-k) + F(k,2k) + iG(k,-k)\omega)c_2}{1 - G(k,-k)c_2}, \\ \mathscr{A}_{12} &= \frac{(F(k,-k) + F(k,2k))c_1 + iG(k,-k)\omega c_1}{1 - G(k,-k)c_2}, \\ \mathscr{A}_{21} &= 2F(2k,k)c_1, \\ \mathscr{A}_{22} &= \Lambda(2k) + i2\omega. \end{aligned}$$

If the real part of an eigenvalue of the matrix $\mathscr{A}$ is positive (negative), it indicates that there is an unstable (stable) branch of the dynamic system defined by Eqs. (2.31) and (2.32), and whether the perturbations increase (decrease) with time. For each of the analyzed set of parameters, there is only one root for ω that makes negative the real parts of both eigenvalues of $\mathscr{A}$. Thus, it defines the actual stable propagating solution. This root is explicitly given in Eq. (2.42) in Sec. 2.2.5.

Figure 2.11 makes a comparison of the analytical weakly nonlinear prediction for final propagating velocity from (2.42) (plotted as continuous curves) with the one obtained by numerically solving the differential equations (2.31) and (2.32) (plotted as dots). It is also shown the linear prediction for the fastest growing mode phase velocity $\mathrm{Im}[-\Lambda(k_{max})/k_{max}]$ displayed as dotted curves. This is done to investigate the plausibility of the purely linear approximation. Here we plot v_f as a function of α for three values of $N_B = 20, 25, 30$ with black, dark gray and light gray curves, respectively. Since we are considering the case where $c_0 = 0$, there are only contributions to v_f that come from the tilted magnetic field. The vertical dashed lines indicate the critical values of α below which the interface is stable and remains flat. As we can see, the

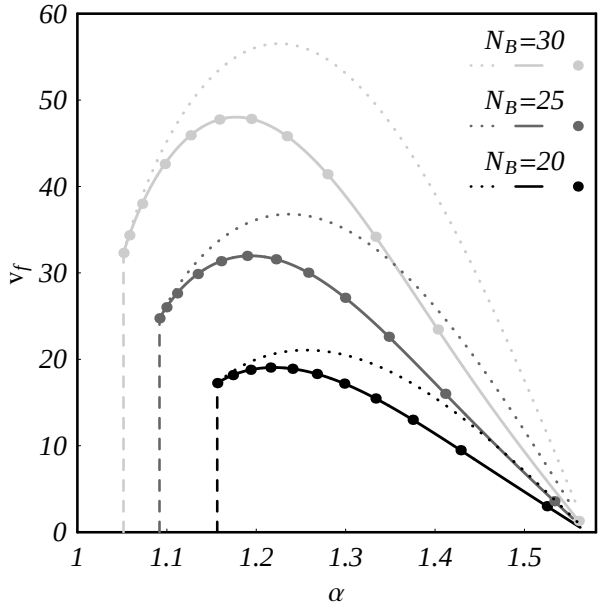

Figure 2.11: Propagating final velocity v_f as a function of α for $c_0 = 0$, $N_B = 20$ (black), $N_B = 25$ (dark gray) and $N_B = 30$ (light gray). The dotted curves depict the linear prediction of the fastest growing mode phase velocity, the solid curves correspond to the analytical weakly nonlinear prediction, and the dots show the velocities obtained by numerically evaluating the time evolution of Eqs. (2.31) and (2.32). The dashed vertical lines indicate the critical values of α.

curves reach a maximum of v_f for a value of α greater than the critical one, and then tend to zero as α approaches $\pi/2$, when there is no magnetic field tilting. In addition, it is observed that for any value of α the final velocity gets larger when N_B is increased. So, by tuning α and N_B one can control v_f.

By comparing the solid curves with the dotted ones, we notice that the linear prediction works well when α is near its critical value or near $\pi/2$. This can be understood by the observation that near the critical value of α only the fundamental mode k_{max} has noticeable amplitude, and there is effectively just one mode acting, and thus negligible nonlinear coupling. For higher values of α there is a relevant difference between the weakly nonlinear and the linear prediction, indicating that the coupling between the k_{max} and its harmonic is significant. More-

over, for α near $\pi/2$ there is no second-order contribution to the propagation, so the agreement with the linear prediction is good again. On the other hand, by comparing the solid curves with the dots, we verify that there is an excellent agreement between the analytical weakly nonlinear predictions, and the numerical results. Therefore, we conclude that the coupling between the modes plays a fundamental role in determining the final propagation velocity.

2.2.5 Nonlinear velocity calculation

In this section we present the details of the analytical calculation for the nonlinear wave velocity v_f. We begin by substituting the ansatz expressions $\zeta_k(t) = c_1 \exp(-i\omega t)$ and $\zeta_{2k}(t) = c_2 \exp(-i2\omega t)$ in Eqs. (2.31) and (2.32) to obtain the following equations involving c_1, c_2 and ω

$$\begin{aligned} \omega &= i\Lambda(k) + ic_2[F(k,-k) + F(k,2k) \\ &+ i(G(k,-k) - G(k,2k))\omega], \end{aligned} \tag{2.34}$$

$$2\omega c_2 = i\Lambda(2k)c_2 + ic_1^2[F(2k,k) - iG(2k,k)\omega], \tag{2.35}$$

where we have used that $\zeta_{-k}(t) = \zeta_k^*(t)$ and $c_1 = c_1^*$, with the star representing complex conjugation. By taking the real and imaginary parts of these equations, and by eliminating the variables c_1 and c_2, we find a third order polynomial equation for ω

$$a\omega^3 + b\omega^2 + c\omega + d = 0, \tag{2.36}$$

whose coefficients are real, and given by

$$\begin{aligned} a &= \mathrm{Re}[(G(k,-k) - G(k,2k))\{2F(2k,k) \\ &+ G(2k,k)(2\Lambda(k) + \Lambda(2k))\} \\ &- 2G(2k,k)(F(k,-k) + F(k,2k))], \end{aligned} \tag{2.37}$$

$$
\begin{aligned}
b &= \mathrm{Im}[(F(k,-k)+F(k,2k))\{2F(2k,k) \\
&+ G(2k,k)(2\Lambda^*(k)+\Lambda^*(2k))\} \\
&+ (G(k,-k)-G(k,2k))\{F^*(2k,k)(2\Lambda(k) \\
&+ \Lambda(2k))+G(2k,k)\Lambda(k)\Lambda(2k)\}],
\end{aligned}
\tag{2.38}
$$

$$
\begin{aligned}
c &= \mathrm{Re}[(F^*(k,-k)+F^*(k,2k))\{G(2k,k)\Lambda(k)\Lambda(2k) \\
&+ F^*(2k,k)(2\Lambda(k)+\Lambda(2k))\} \\
&- (G(k,-k)-G(k,2k))F^*(2k,k)\Lambda(k)\Lambda(2k)],
\end{aligned}
\tag{2.39}
$$

$$
d = \mathrm{Im}[(F^*(k,-k)+F^*(k,2k))F^*(2k,k)\Lambda(k)\Lambda(2k)].
\tag{2.40}
$$

The problem is further simplified by noticing that Eq. (2.28) imposes that $G(k,2k)=G(2k,k)=0$. The discriminant of Eq. (2.36) is

$$
\Delta = 18abcd - 4b^3d + b^2c^2 - 4ac^3 - 27a^2d^2,
\tag{2.41}
$$

being always positive for the range of physical parameters considered in this work [59, 71]. As a result, there are three distinct real roots given by

$$
\omega_1 = -\frac{b}{3a} + \frac{(1-i\sqrt{3})(-b^2+3ac)}{3\,2^{\frac{2}{3}}a\,p} - \frac{(1+i\sqrt{3})p}{3\,2^{\frac{4}{3}}a},
\tag{2.42}
$$

$$\omega_2 = -\frac{b}{3a} + \frac{(1+i\sqrt{3})(-b^2+3ac)}{3\,2^{\frac{2}{3}}a\,p} - \frac{(1-i\sqrt{3})p}{3\,2^{\frac{4}{3}}a}, \tag{2.43}$$

$$\omega_3 = -\frac{b}{3a} + \frac{2^{\frac{1}{3}}(-b^2+3ac)}{3a\,p} - \frac{p}{3\,2^{\frac{1}{3}}a}, \tag{2.44}$$

where

$$\begin{aligned} p &= \Big[-2b^3+9abc-27a^2d \\ &+ \sqrt{4(-b^2+3ac)^3+(-2b^3+9abc-27a^2d)^2}\Big]^{\frac{1}{3}}. \end{aligned} \tag{2.45}$$

By performing a stability analysis for each of these roots, as described in Sec. 2.2.4, we verify that ω_1 is the only one that is indeed stable. Therefore, the solution related to ω_1 [Eq. (2.42)] is the one that prevails from the system dynamics, so that the observed final nonlinear propagating velocity is given by $v_f = \omega_1/k$.

CHAPTER 3

Field-induced patterns in MR fluids

As it was explained in the previous chapter, magnetic fluids termed as ferrofluids [14, 15] are stable colloidal suspensions typically containing water or oil combined with nanometersized magnetic particles. This particular type of magnetic fluid is ultrastable against settling, behaves superparamagnetically, can be considered to be a Newtonian fluid, and is characterized by its prompt response to even modest magnetic fields. Due to its responsiveness to magnetic stimuli, the study of ferrofluid interfacial pattern formation has become considerably popular [80, 81]. In particular, under spatially confined circumstances of a Hele-Shaw cell the viscosity-driven Saffman-Taylor instability [1] is supplemented by a magnetically induced instability, leading to a variety of interesting interfacial behaviors. The Hele-Shaw flow problem, with either non-magnetic or magnetic fluids, has already proven its prototypical role in the context of interfacial pattern formation [2].

On the other hand, the study of Hele-Shaw pattern formation with magnetorheological (MR) fluids has not been much investigated. Magnetorheological fluids consist of much larger, micronsized magnetized particles dispersed in aqueous or organic carrier liquids, display strong nonNewtonian features, and are much less stable than ferrofluids. The unique feature of this kind of magnetic fluid is the abrupt change in its viscoelastic properties upon the application of an external magnetic field [25, 26, 27, 28, 29]. A MR fluid can be characterized by its yield stress, which measures the strength of its solidlike behavior. As opposed to Newtonian fluids, yield stress fluids [30] (magnetic or not) can support shear stresses without flowing. As long as the stress remains below to a certain critical value they do not flow, but respond elastically to deformation. In MR fluids the yield stress is magnetic field-dependent, and varies quadratically with the strength of the applied field. As the magnitude of the applied magnetic field is increased, the yield stress which is associated to the highest value of stress required to break the existing network of magnetic interactions, also increases. In this sense, MR fluids work as

smart materials whose viscoelastic properties can be conveniently tuned by an applied magnetic field. By the way, the appearance of viscoelastic properties such as yield stress in ferrofluids, and its quadratic dependence on the applied magnetic field has been recently verified experimentally [82, 83]. Nevertheless, it has been found that in ferrofluids the field-dependent yield stress is indeed very small as compared to the typical values obtained for MR fluids.

3.1 Radial magnetic field

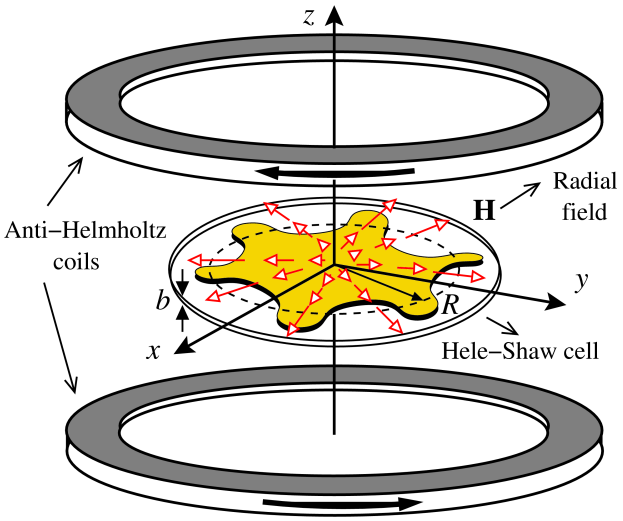

Figure 3.1: Schematic illustration of a Hele-Shaw cell of thickness b containing an initially circular droplet (dashed curve) of a MR fluid, surrounded by a nonmagnetic fluid. The anti-Helmholtz coils produce a magnetic field **H** pointing radially outwards in the plane of the cell. Fingering interfacial patterns arise due to the action of the radial magnetic field.

In this section we embark upon the study of pattern formation phenomena in MR fluids confined in Hele-Shaw geometry. Considering the paradigmatic role played by Hele-Shaw flows [1, 2, 14, 15, 80, 81], our investigation can be of significance to a number of physical, biological, and engineering systems related to the viscous fingering phenomenon. It is in this context where the problem we study can gain some more general relevance. We follow a

previous analysis recently performed by our research group [24] in which the response of a *ferrofluid* droplet to a radial magnetic field has been investigated. Here, unlike most common situations examined in the literature, we focus on the situation where the constrained drop is a *magnetorheological* fluid, allowing its yield stress to be manipulated via the application of an external radial magnetic field. The magnetically tuned viscoelastic properties introduced by this system open up the possibility of unveiling still unexplored pattern morphologies and interesting dynamic behavior.

In Sec. 3.1.1 the basic equations describing the system are presented, and the moving boundary problem is properly specified. By employing a mode-coupling approach (Sec. 3.1.2) we have been able to study the linear stability of the rising patterns, as well as to examine important aspects of their morphology at the onset of nonlinear effects. A more detailed account of the resulting nonlinear shapes is provided by the determination of nontrivial exact stationary solutions for the problem with nonzero surface tension. These solutions are obtained through a vortex-sheet formalism, and reveal the development of characteristic swollen polygon-shaped patterns (Sec. 3.1.3). We have also identified a magnetically induced shape transition in which the interface goes from convex to concave as magnetic field effects are considerably larger than interfacial tension. A summary of our chief conclusions is presented in Sec. 6.2.

3.1.1 Physical problem and governing equations

Figure 3.1 illustrates an incompressible, MR fluid droplet of unperturbed radius R and viscosity η, which is surrounded by a nonmagnetic, Newtonian fluid of negligible viscosity. The fluids are located between two narrowly spaced flat plates of a Hele-Shaw cell of thickness b. The surface tension between the fluids is nonzero and denoted by γ. We consider that the MR fluid droplet is subjected to a radial magnetic field

$$\mathbf{H} = \frac{H_0}{L} r\, \hat{\mathbf{r}}, \tag{3.1}$$

where r is the radial distance from the origin of the coordinate system (located at the center of the droplet), H_0 is a constant, L is a characteristic length, and $\hat{\mathbf{r}}$ is a unit vector in the

radial direction. It is worth pointing out that this specific magnetic field configuration can be generated by a pair of identical Helmholtz coils whose currents are equal and flow in opposite directions (“anti-Helmholtz" configuration). The experimental conditions required to obtain such a radial magnetic field have been discussed in detail in Ref. [84].

For the quasi-two-dimensional geometry of the Hele-Shaw cell, one reduces the three-dimensional flow to an equivalent two-dimensional one by averaging the Navier-Stokes equation over the direction perpendicular to the plates. The gap-average procedure is performed by neglecting the inertial terms, considering a large aspect ratio geometry ($R \gg b$), and using the Bingham model for yield stress fluids [32, 85]. By taking into account the contribution of viscoelastic and magnetic effects, plus the existence of a magnetic field-dependent yield stress $\sigma_y = \sigma_y(H)$, one can write a modified Darcy's law for confined MR fluids [32, 85, 86]

$$\mathbf{v} = -\frac{b^2}{12\eta}\left[\nabla\Pi + \frac{3\sigma_y(H)}{b}\,\hat{\mathbf{r}}\right]. \tag{3.2}$$

The derivation of Eq. (3.2) assumes the regime of high viscosity compared to yield effects. On the basis of the symmetry of the applied magnetic field configuration, we consider the prevalent yielding occurring along the radial direction. Note that one recovers the usual Darcy's law for Newtonian magnetic fluids [16, 17] by setting $\sigma_y(H) = 0$.

The gap-averaged generalized pressure is defined as

$$\Pi = \frac{1}{b}\int_{-b/2}^{+b/2}[P - \Psi]\,dz, \tag{3.3}$$

where P is the three-dimensional hydrodynamic pressure,

$$\Psi = \mu_0 \int_0^H M dH \tag{3.4}$$

represents a magnetic pressure, μ_0 denotes the magnetic permeability of free space, and M is the magnetization of the MR fluid. Note that for the nonmagnetic fluid $M = 0$. In this context, the magnetic body force acting on the MR fluid is given by $\mu_0 M\nabla H$ [14, 15], where H is the applied magnetic field.

The magnetic field-dependent yield stress is given by [27, 28, 29, 82, 83, 87, 88]

$$\sigma_y(H) = \sigma_{y0} + \alpha H^2, \tag{3.5}$$

where σ_{y0} represents the yield stress in the absence of the magnetic field, and α is a constant that depends on the material properties of the MR fluid, being proportional to the particle volume fraction [29]. In general the field dependence of a yield stress fluid is represented by a power law $\sigma_y(H) - \sigma_{y0} \sim H^n$ with $1 \leq n \leq 2$, and the case we consider here $n = 2$ is the one for which the magnetization is linearly related to the applied magnetic field [27, 28, 29] $\mathbf{M} = \chi \mathbf{H}$, where χ is the magnetic susceptibility. This linear relation holds as long as $H \ll H_{sat}$, where H_{sat} is the field magnitude at saturation magnetization [$O(10^2$ kA/m $- 10^3$ kA/m)]. It is worth emphasizing that, despite the nonNewtonian character of the MR fluid (due to its yield stress), we consider that it presents a constant viscosity. This assumption enables the flow to stay potential. Of course, more involved theoretical descriptions may incorporate a shear and magnetic field-dependent viscosity to certain types of magnetic fluids [89], but this is beyond the scope of our current work.

Forces arising from gradients of the mean pressure, as in the case of Darcy's law (3.2), characterize an irrotational flow in the bulk. In this framework Darcy's law (3.2) can be conveniently rewritten in a *dimensionless* form

$$\begin{aligned} \mathbf{v} &= -\nabla\phi, \\ \phi &= p - \chi N_B r^2 + S_0 r + S r^3, \end{aligned} \tag{3.6}$$

where ϕ is a velocity potential, and p is the gap-averaged hydrodynamic pressure. The parameter

$$N_B = \frac{\mu_0 H_0^2 r_0^3}{2\gamma L^2} \tag{3.7}$$

represents the dimensionless magnetic Bond number, and measures the ratio of magnetic to

capillary forces. In addition

$$S_0 = \frac{3\sigma_{y0} r_0^2}{\gamma b} \tag{3.8}$$

and

$$S = \frac{\alpha H_0^2 r_0^4}{\gamma L^2 b} \tag{3.9}$$

are related to the yield stress contributions at zero, and nonzero applied magnetic field, respectively. In Eq. (3.6) lengths and velocities are rescaled by r_0, and $\gamma b^2/(12\eta r_0^2)$, respectively. The typical length scale r_0 is of the order of the unperturbed droplet radius R, and will be more properly defined subsequently (Sec. 3.1.3). From now on, we work with the dimensionless version of the equations.

By inspecting Eq. (3.6) the driving and stabilizing forces of the problem become apparent. It has a radial driving force pushing the MR fluid off-center, with a term growing linearly with the radial coordinate (proportional to N_B) stemming from the magnetic pressure Eq. (3.4). Moreover, it presents two stabilizing contributions, the first one being a constant force (proportional to S_0), and a second which is quadratic (proportional to S) in the radial coordinate. These stabilizing forces come from the two terms of the yield stress given by Eq. (3.5). Already at this point, we can find noteworthy connections of Eq. (3.6) with general Hele-Shaw flow problems: one can identify the rotating Hele-Shaw centrifugal force [8, 90, 91], and the channel-geometry constant driving force (gravity or pressure difference) [92, 93] but of stabilizing nature. On the other hand, the quadratic term in the force (proportional to S) is unparalleled, being exclusively related to the field-dependent yield stress.

Further specification about the velocity potential is provided by the augmented pressure jump boundary condition

$$\Delta p = \kappa - N_B \chi^2 r^2 (\hat{\mathbf{n}} \cdot \hat{\mathbf{r}})^2, \tag{3.10}$$

where $\hat{\mathbf{n}}$ denotes the unit normal vector to the interface. The first term on the right-hand side of Eq. (3.10) represents the usual contribution related to surface tension and interfacial curvature κ. Here κ is the dimensionless in-plane curvature. The meniscus curvature, in the direction perpendicular to the plates, is of larger magnitude, but nearly constant. Therefore, its gradient is nearly zero, so that it does not significantly affect the dynamics. When the assumption of

constant meniscus curvature is valid, the cell gap thickness can be scaled out of the problem, since it always appears together with the viscosity. This is the reason why the basic equations of the problem are not explicitly dependent on b. The second term in Eq. (3.10) is set by the so-called magnetic normal traction [14, 15], which considers the influence of the normal component of the magnetization at the interface, and its linear relation to the applied magnetic field.

From the incompressibility condition $\nabla \cdot \mathbf{v} = 0$ it can be verified that the velocity potential is Laplacian. Therefore, the definition of the moving boundary problem is specified by the following equations

$$\nabla^2 \phi = 0, \tag{3.11}$$

$$\frac{\partial \phi}{\partial n}|_{in} = \frac{\partial \phi}{\partial n}|_{out}, \tag{3.12}$$

$$\frac{\partial \phi}{\partial s}|_{in} - \frac{\partial \phi}{\partial s}|_{out} = \Gamma, \tag{3.13}$$

where the subscripts label the inner (*in*) and outer (*out*) fluids, and $\partial/\partial s = \partial_s$ ($\partial/\partial n = \partial_n$) is the derivative along the tangent (normal) direction to the interface. Equation (3.12) describes the continuity of the normal velocity at the interface, and Eq. (3.13) its tangential jump of magnitude Γ. This jump originates a nonzero vorticity region restricted to the interface separating the fluids [94, 95]. With the help of the generalized Darcy's law Eq. (3.6), and the pressure jump Eq. (3.10) an explicit expression for the vortex sheet strength can be derived yielding

$$\begin{aligned} \Gamma &= 2\partial_s \left\{ \kappa - N_B r^2 \chi [1 + \chi (\hat{\mathbf{n}} \cdot \hat{\mathbf{r}})^2] + S_0 r + S r^3 \right\} \\ &- \left(\frac{\partial \phi}{\partial s}|_{in} + \frac{\partial \phi}{\partial s}|_{out} \right). \end{aligned} \tag{3.14}$$

While presenting our results in Secs. 3.1.2 and 3.1.3 we make sure that the values of all relevant dimensionless quantities we utilize [Eqs. (3.7)-(3.9)] are consistent with realistic physical parameters related to existing magnetic field arrangements, and material properties of MR fluids. For the typical parameters related to the Hele-Shaw setup under study, we take $b = 10^{-3}$ m (which appears in S_0 and S), and $R = 10^{-2} - 10^{-1}$ m. Recall that r_0 (that shows up in N_B,

S_0, and S) has the same order of magnitude of R. While dealing with the strength of the magnetic fields, we consider a relatively low values 2.5 kA/m $\leq H_0 \leq$ 10 kA/m which are easily achievable by using a typical Helmholtz coils setup, where the radius of a coil is considerably larger than the radius of the MR fluid droplet. The characteristic length L related to the radial magnetic configuration is of the order of a few centimeters [84]. The quantities H_0 and L are present in the paramenters N_B and S. Regarding the material properties of the MR fluid, in S we take $\alpha = 3.0 \times 10^{-7}$ N/A^2 [82, 88], and in S_0 consider that the "off" state yield stress σ_{y0} varies from 0.3 Pa to 45 Pa [88, 96]. For the magnetic susceptibility we take $0.1 \leq \chi \leq 1$ [97]. Finally, for the surface tension γ we use a typical value of 10^{-3} Pa m in the parameters given by Eqs. (3.7)-(3.9).

3.1.2 Linear stability and weakly nonlinear dynamics

After having formally stated the moving boundary problem in terms of the velocity potential, we proceed by employing a perturbative mode-coupling approach to examine the linear stability of the interface, and morphological features of the resulting patterns at the onset of nonlinear effects.

Due to the action of the radial magnetic field the fluid-fluid interface may deform, and its perturbed shape is described as $\mathscr{R}(\varphi,t) = R + \zeta(\varphi,t)$, where $\zeta(\varphi,t) = \sum_{n=-\infty}^{+\infty} \zeta_n(t) \exp(in\varphi)$ represents the net interface perturbation with Fourier amplitudes $\zeta_n(t)$, and discrete azimuthal wave numbers n. The azimuthal angle in the plane of the Hele-Shaw cell is denoted by φ. We define Fourier expansions for the velocity potential, and use the boundary conditions presented in Sec. 3.1.1 to express ϕ in terms of ζ_n to obtain a dimensionless mode-coupling differential equation for the system (for $n \neq 0$), accurate to second-order in the perturbation amplitudes

$$\begin{aligned} \frac{d\zeta_n}{dt} &= \lambda(n)\,\zeta_n \\ &+ \sum_{n' \neq 0} \left[F(n,n') + \lambda(n')G(n,n')\right]\,\zeta_{n'}\zeta_{n-n'}, \end{aligned} \tag{3.15}$$

where

$$\lambda(n) = |n| \left[2N_B\chi(1+\chi) - \frac{1}{R^3}(n^2-1) - \frac{S_0}{R} - 3SR \right] \tag{3.16}$$

is the linear growth rate. The second-order mode-coupling terms are represented as

$$\begin{aligned} F(n,n') &= \frac{|n|}{R}\Bigg\{ N_B\chi[1+\chi(1+n'(n-n'))] \\ &- \frac{1}{R^3}\left[1 - \frac{n'}{2}(3n'+n)\right] - 3SR \Bigg\}, \end{aligned} \tag{3.17}$$

$$G(n,n') = \frac{1}{R}\{|n|[\mathrm{sgn}(nn')-1]-1\}. \tag{3.18}$$

The sgn function equals ± 1 according to the sign of its argument. Notice that when $S = S_0 = 0$ Eqs. (3.16)-(3.18) reproduce the results obtained in Ref. [24] for the corresponding problem in Newtonian ferrofluids, where yield stress effects have been completely neglected.

The terms appearing in the expression for the function $F(n,n')$ in Eq. (3.17) arise from the magnetic applied field, surface tension, and field-dependent yield stress, respectively. The term proportional to χ^2 comes from the square of the projection of the interface normal in the radial direction in the pressure jump condition [Eq. (3.10)]. In contrast the function $G(n,n')$ defined in Eq. (3.18) presents no dependence on magnetic effects.

We use Eq. (3.15) to investigate how the development of interfacial instabilities at early stages of the pattern formation is influenced by the radial magnetic field. At the linear level, the relevant physical effects examined in the discussion of Eq. (3.6) just add up, as expressed by the linear growth rate. Since a positive $\lambda(n)$ leads to an unstable interface, Eq. (3.16) tells us that for a given nonzero χ, N_B destabilizes the system. As expected, the magnetic contribution to the growth rate tends to move the MR fluid toward regions of higher magnetic fields, stimulating the growth of fingering structures. This behavior is analogous to the role played by the centrifugal force in the rotating Hele-Shaw problem [8, 90, 91]. On the other

hand, the term involving (n^2-1) is associated to the surface tension and plays a stabilizing role. The terms related to the yield stress contribution (S and S_0) are also stabilizing and tend to inhibit fingering formation. In particular the term S_0 is related to a constant radial force acting similarly to gravity or pressure difference appearing in the usual Saffman-Taylor problem in channel geometry [92, 93].

By examining Eq. (3.16) it is evident that increasingly larger values of S and S_0 shrink the band of unstable modes [which can be accessed by taking $\lambda(n)=0$]. In addition, we notice that the maximum of $\lambda(n)$ which occurs at $n=n_{max}$, where

$$n_{max}=\sqrt{\frac{1}{3}\left\{1+R^3\left[2N_B\chi(1+\chi)-\frac{S_0}{R}-3SR\right]\right\}} \tag{3.19}$$

decreases as S or S_0 is ramped up. As it is well known, the fastest growing mode, given by the closest integer to n_{max}, is the mode that will tend to dominate during early stages of the pattern formation.

In summary, at the very early stages of the dynamics the role of the yield stress terms is to decrease the wave number of maximum growth just as the maximum growth rate, and to tight the band of unstable modes. Conversely, both N_B and χ tend to destabilize the system. Note that the additional magnetization term appearing in Eq. (3.10) is of second order in the interface perturbation ζ, being legitimately nonlinear and therefore of no influence at purely linear stages of interfacial evolution.

Despite the importance of the linear stability analysis, interesting information about the morphology of the rising patterns can be acquired at the weakly nonlinear stage of the interface evolution. We investigate how the radial magnetic field influences the shape of the emerging MR fluid patterns by using the full mode-coupling differential equation (3.15). As in Refs. [24, 61] we study a mechanism controlling the finger shape behavior through magnetic means, and consider the coupling of a small number of modes. To simplify our discussion we rewrite Eq. (3.15) in terms of cosine and sine modes, where the cosine $a_n=\zeta_n+\zeta_{-n}$ and sine $b_n=i(\zeta_n-\zeta_{-n})$ amplitudes are real-valued. Without loss of generality we choose the phase of the fundamental mode so that $a_n>0$ and $b_n=0$. Under such circumstances, finger tip-sharpening

and tip-broadening phenomena are described by considering the influence of a fundamental mode n on the growth of its harmonic $2n$. One key piece of information about the morphology of the emerging patterns can be extracted from the equation of motion (3.15) for the harmonic cosine mode

$$\frac{da_{2n}}{dt} = \lambda(2n)\, a_{2n} + \frac{1}{2}\, T(2n,n)\, a_n^2, \tag{3.20}$$

where the finger tip function is given by

$$T(2n,n) = [F(2n,n) + \lambda(n)\, G(2n,n)]\,, \tag{3.21}$$

due to Eqs. (3.17) and (3.18). It can be shown that the equivalent growth of the sine mode b_{2n} is uninfluenced by a_n and does not present second-order couplings, so we focus on the growth of the cosine mode.

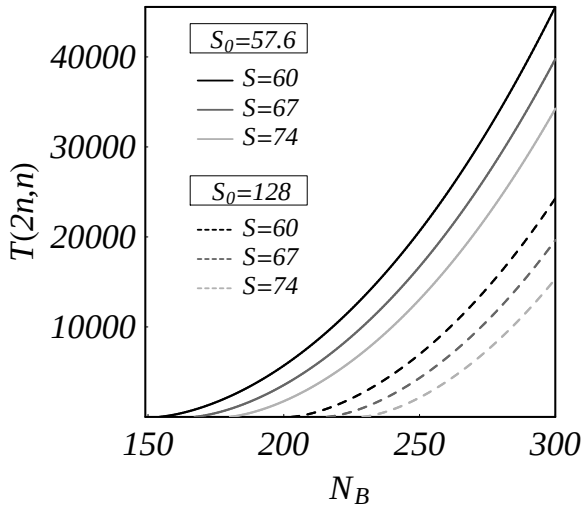

Figure 3.2: Behavior of the finger tip function $T(2n,n)$ as the magnetic Bond number N_B is varied, for $R = 0.9$, $\chi = 0.5$, and two different values of the zero field yield stress parameter: $S_0 = 57.6$ (solid curves), and $S_0 = 128$ (dashed curves). For each value of S_0, three increasing magnitudes for the magnetic field-dependent yield stress parameter are used: $S = 60$ (black), $S = 67$ (dark gray), and $S = 74$ (light gray).

The interesting point about the function $T(2n,n)$ is that it controls the finger shape behavior. The sign of $T(2n,n)$ dictates whether finger tip-sharpening or finger tip-broadening is favored by the dynamics. From Eq. (3.20) we see that if $T(2n,n) > 0$, the result is a driving term of order a_n^2 forcing growth of $a_{2n} > 0$, the sign that is required to cause outwards-pointing fingers to become sharp, favoring finger tip-sharpening. In contrast, if $T(2n,n) < 0$ growth of $a_{2n} < 0$ would be favored, leading to outwards-pointing finger tip-broadening.

In order to gain insight about the morphological response of the fingers to the action of a radial magnetic field, and also to the effects induced by yield stress, in Fig. 3.2 we plot $T(2n,n)$ as a function of N_B. We consider two distinct values of S_0, and for each one of them we take three increasingly larger values of S. As in Ref. [24], to ensure that both participating modes (n and $2n$) are able to grow we take n such that $\lambda(2n) = 0$, implying in the observance of a critical value of N_B for each pair of S_0 and S.

By inspecting Fig. 3.2 we readily observe that $T(2n,n)$ is a positive, increasing function of N_B, indicating that once the fingers are formed they tend to develop sharp tips. Moreover, for a given S_0 we notice that $T(2n,n)$ tends to decrease as one increases the value of S. This indicates that the yield stress influences the shape of the patterns, inhibiting the formation of pronounced spiked tips. It is also clear that larger values of S_0 favor further suppression of sharp edged fingers.

We conclude this section by contrasting the finger tip behavior studied here with other general Hele-Shaw problems. First, we point out that in the channel geometry Hele-Shaw setup [92, 93] there is no coupling between the fundamental and its first harmonic mode, leading to absence of finger tip-splitting at second order. Besides, the situation of a Newtonian ferrofluid in the presence of a radial magnetic field [24] does present such a coupling, resulting in a high magnitude, positive finger tip function $T(2n,n)$ which favors the formation of sharp fingers. However, in the MR fluid case, the presence of the yield stress (negative sign) terms S and S_0 in the mode-coupling function $F(n,n')$ and in $\lambda(n)$ conspire to produce a positive finger tip function of smaller magnitude, resulting in fingering structures that are less sharp than the ones obtained with Newtonian ferrofluids.

The weakly nonlinear predictions suggest that the resulting fingers should become less and

less sharp as the yield stress parameters are augmented. In this sense, our mode-coupling approach enables one to access analytically the morphology of the emerging structures already at very early nonlinear stages of the dynamics. This is in contrast to the usual purely linear results which primarily refer to the stability of the patterns.

3.1.3 Exact stationary solutions

In this section we turn to a more specific description of the patterns' morphology through the calculation of exact solutions for this problem. The exact stationary solutions reveal even more details about the shape of the patterns. Similarly to Ref. [24] we apply a vortex-sheet formalism [94, 95] in order to access the exact stationary shapes obtained when a droplet of a confined MR fluid is subjected to a radial magnetic field. As discussed in detail in Refs. [68, 98] this type of exact solutions with nonzero surface tension can be found by imposing a condition of zero vorticity ($\Gamma = 0$) plus considering a stationary state ($\partial\phi/\partial s|_{in} = \partial\phi/\partial s|_{out} = 0$) in Eq. (3.14). Under such circumstances, we find that the curvature of the interface satisfies a nonlinear ordinary differential equation

$$\partial_s \left\{ \kappa - N_B r^2 \chi [1 + \chi (\hat{\mathbf{n}} \cdot \hat{\mathbf{r}})^2] + S_0 r + S r^3 \right\} = 0, \tag{3.22}$$

which can be integrated to obtain

$$\kappa = \kappa(r, r\sin\psi) = a + b\, r^2 + c\, (r\sin\psi)^2 - S_0 r - S r^3, \tag{3.23}$$

where a is a constant of integration. For brevity we define $b = N_B\chi$, and $c = N_B\chi^2$. In Eq. (3.23) we have used the fact that $\hat{\mathbf{n}} \cdot \hat{\mathbf{r}} = \pm\sin\psi$, where ψ is the angle between the radius vector $\hat{\mathbf{r}}$ and the tangent vector $\hat{\mathbf{s}}$ at the interface.

Our goal is to study the fully nonlinear family of planar curves whose curvature has the general form given by Eq. (3.23). These curves are the nonzero surface tension exact stationary solutions which balance the competing capillary, viscoelastic, and magnetic effects at the MR

fluid interface. A number of important morphological features of the stationary solutions can be obtained by the numerical evaluation of the nonlinear differential equation (3.22), without recourse to intensive numerical simulations. This way, we can explore the richness behind a family of curves whose curvatures are prescribed by Eq. (3.23) by manipulating the relevant control parameters of the problem, namely N_B, χ, S_0, S, the constant a, and the specifications $r_0 = r(\varphi = 0)$ and $\psi_0 = \psi(\varphi = 0)$. For a thorough discussion about the numerical approach used to solve the type of differential equation given in (3.22) we refer the reader to Ref. [98].

The parameter r_0 defines the maximum radial distance obtained for a given stationary pattern, and is of the order of the unperturbed droplet radius R. At this point, we justify our choice of r_0 as a convenient parameter to rescale lengths in our problem. If the unperturbed radius R were to be chosen as the parameter to rescale lengths, a very strict constraint would be imposed to the system, since in this case all the areas of the resulting exact steady shapes should have to coincide. It turns out that it is not at all trivial to keep the areas of all perturbed patterns the same, and simultaneously fulfill the requirements that all interfacial curves should be closed (i.e., commensurable with 2π), and non-self-intersecting. We have circumvented this practical difficulty by conveniently selecting r_0 as the appropriate length scale for the problem without loss of generality.

In Fig. 3.3 we present a representative collection of possible exact stationary solutions for the problem of a confined MR fluid droplet under the influence of a radial magnetic field. The shapes are obtained for $N_B = 256$, $\chi = 0.5$, $\psi_0 = \pi/2$, $r_0 = 1$, $S_0 = 57.6$, and by considering four decreasing values of the magnetic field-dependent yield stress parameter S: (a) 105.13, (b) 100.13, (c) 93.13, and (d) 84.13. For convenience, for each value of S, we adjust the constant a so that the final pattern has the number of fingers (or, edges) $n = n_{max}$ as arising from the linear regime according to Eq. (3.19). We emphasize that the choice of a is arbitrary, and the way we set it should not be interpreted as if the linear regime dictates the final morphological features of the fully nonlinear exact steady shapes. Note that all patterns shown in this work are stationary shapes, and *not* a time evolving sequence of events. The resulting peculiar shapes depicted in Fig. 3.3 resemble convex-shaped polygons. In fact, they are what we could name as n-gons with $n = 2, 3, 4$ and 5 corners. They look like “swollen" regular polygons presenting convex edges.

This family of shapes differs from the ones obtained in Ref. [24] for Newtonian ferrofluids, where concave-shaped polygons and peaky starfish-like structures (with edges curved inward) have been obtained. So, the convex-shape signature of the patterns can be attributed to the yield stress effects introduced by the parameters S_0 and S. It is also evident from Fig. 3.3 that by decreasing the value of S (keeping N_B and S_0 fixed) the number of fingering structures (or, corners) increases.

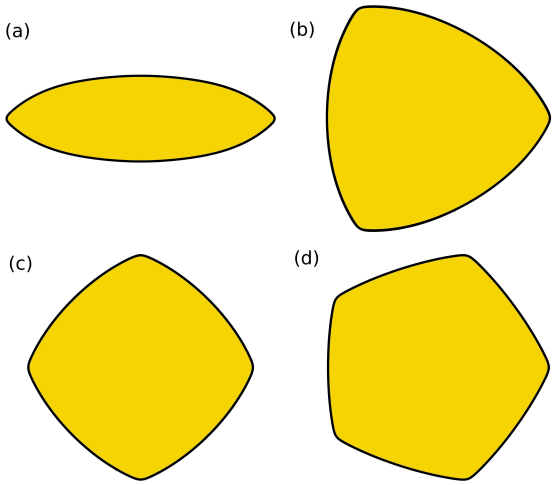

Figure 3.3: Typical stationary shape solutions for $N_B = 256$, $\chi = 0.5$, $\psi_0 = \pi/2$, $r_0 = 1$, $S_0 = 57.6$, and (a) $S = 105.13$, (b) $S = 100.13$, (c) $S = 93.13$, and (d) $S = 84.13$.

Figure 3.4 addresses a situation similar to the one illustrated in Fig. 3.3, but now taking a larger value of the zero applied field yield stress parameter $S_0 = 128$. We set $N_B = 256$, $\chi = 0.5$, $\psi_0 = \pi/2$, $r_0 = 1$, and consider the following decreasing values of S: (a) 81.67, (b) 76.67, (c) 69.67, and (d) 60.67. As in Fig. 3.3 for each value of S we adjust the magnitude of a so that $n = n_{max}$. The resulting exact shapes are again characterized as regular n-gons presenting convex-shaped edges, where the number of corners increase for lower values of S. However, the patterns shown in Fig. 3.4 for $S_0 = 128$, are even more “inflated" than the ones obtained in Fig. 3.3 for $S_0 = 57.6$. In Fig. 3.4 the edges bulge outward, making the tips of the fingers to become not as sharp as the ones obtained in Fig. 3.3. In other words, the consideration of larger values of S_0 resulted in the inhibition of sharper tips. The comparison between the characteristic shapes presented in Figs. 3.3 and 3.4 reinforces the validity of the weakly nonlinear predictions

made in Sec. 3.1.2, which prognosticated diminished tendency toward finger tip-sharpening for larger S_0.

Another situation of interest refers to the response of the patterns to increased values of the magnetic Bond number N_B. This issue is investigated in Fig. 3.5. It depicts interfacial MR fluid patterns generated by taking $\chi = 0.5$, $\psi_0 = \pi/2$, $r_0 = 1$, $a = -6.36$, $S_0 = 38.02$, $S = 23.80$, and four increasingly larger magnitudes of N_B: (a) 109.85, (b) 126.57, (c) 148.06, and (d) 150.53. Instead of plain convex-shaped structures, different types of patterns arise as N_B increases: first, in Fig. 3.5 (a) a nearly perfect square with almost straight edges is observed. Therefore, the convex polygon sides obtained in Figs. 3.3 and 3.4 have flattened out. As N_B increases further [Fig. 3.5(b)] a sort of "shape transition" is revealed, showing the appearance of a concave-shaped 4-gon presenting more pointy corners (or, fingers). If N_B continues to increase [Fig. 3.5(c)] the number of fingers also increases, while protrusions start growing from them leading to the formation of a starfish-like pattern presenting 5 fingers, similar to those observed in Ref. [24] for Newtonian ferrofluids. If the ramping of N_B goes on [Fig. 3.5(d)], the growth in the number of fingers continues and a six-fingered limiting shape is obtained for which the fingers tend to pinch-off. Incidentally, equivalent pinch-off phenomena have also been found in Ref. [24]. The fact that the patterns presented in Fig. 3.5 tend to the shapes obtained for Newtonian ferrofluids under a radial field makes perfect sense: as N_B is increased the yield stress effects are eventually overcome, making the MR fluid to behave like usual ferrofluids. Note that the linear prediction which regards the growth of a larger number of fingers for increased N_B is consonant with the generic features of the the exact solutions illustrated in Fig. 3.5. Moreover, the weakly nonlinear prediction related to the formation of sharper and sharper fingering structures as N_B is increased can be also verified.

We close this section by discussing an important issue for the relevance of the exact solutions we have found in this work, which refers to their stability. It is known that similar classes of exact solutions, for instance those that arise in the rotating Hele-Shaw problem [68, 98], are unstable. Likewise, the exact stationary patterning structures which emerge when a Newtonian ferrofluid droplet is subjected to an applied radial magnetic field [24] are also unstable. To the best of our knowledge the only known stable exact solutions are those related to peculiar shapes

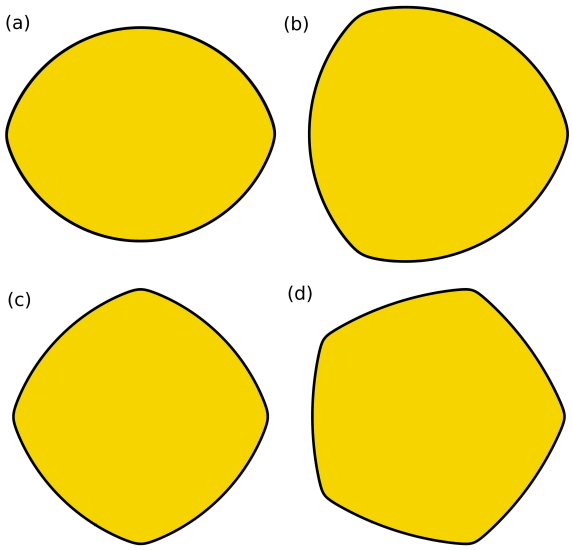

Figure 3.4: Typical stationary shape solutions for $N_B = 256$, $\chi = 0.5$, $\psi_0 = \pi/2$, $r_0 = 1$, $S_0 = 128$, and (a) $S = 81.67$, (b) $S = 76.67$, (c) $S = 69.67$, and (d) $S = 60.67$.

presenting cusplike protrusions obtained for rotating Hele-Shaw flows, in the limit of infinitely long filaments [13].

Despite the stabilizing role played by yield stress effects, we have verified that the exact solutions for MR fluids we investigated in this work are in fact unstable. Most situations will not have a steady state attractor so that a direct connection to the linear and weakly nonlinear regimes can be nontrivial. Moreover, it is correct to say that most of the exact stationary shapes found in Refs. [13, 24, 67, 68, 98], and the ones obtained in this work, are of considerable difficulty to be observed experimentally in a direct fashion. In practice, as discussed in Ref. [68] in order to obtain such stationary solutions one has to be able to carefully set initial conditions which should be sufficiently close to these prescribed forms. In the case of magnetic fluids, this question of experimental accessibility of the steady exact solutions could be possibly facilitated by designing a magnet with the desired shape, and using it to set the proper initial condition in a more controlled fashion [99]. Once this situation is achieved one would verify a slowing down of the dynamics in the neighborhood of stationary states. Actually, an analogous line of reasoning has been recently used in Ref. [13] where it is argued that exact stationary solutions obtained for the rotating Hele-Shaw problem could be of relevance to explain a transient

slowing down observed in existing experiments [100].

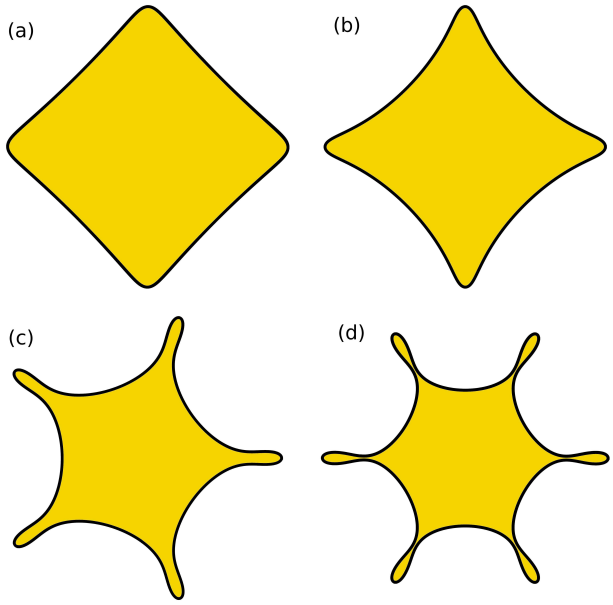

Figure 3.5: Gallery of possible patterns for increasingly larger values of the magnetic Bond number N_B. It is assumed that $\chi = 0.5$, $\psi_0 = \pi/2$, $r_0 = 1$, $a = -6.36$, $S_0 = 38.02$, $S = 23.80$, and (a) $N_B = 109.85$, (b) $N_B = 126.57$, (c) $N_B = 148.06$, and (d) $N_B = 150.53$.

3.2 Stationary shapes of confined rotating magnetic liquid droplets

Since the seminal experimental work by Plateau [101] the study of rotating fluid droplets has attracted the attention of both experimentalists and theorists from several branches of physics. In particular, the understanding of the various equilibrium shapes (ellipsoidlike, two-lobed “peanut" structures, and triangular morphologies) assumed by rotating droplets has caused a lot of excitement [102, 103, 104, 105]. Interestingly, analogies traced between surface tension and gravitational, or nuclear forces have used a spinning droplet description to model more complex phenomena occurring in rotating stars [106] and in nuclear physics processes [107, 108].

An effectively two-dimensional (2D) version of the fully 3D rotating droplet problem can

be examined when the fluid drop is placed in the spatially confined environment of a rotating Hele-Shaw cell [8, 109]. The rotating Hele-Shaw problem is a variation of the traditional viscosity-driven Saffman-Taylor instability [1, 2], in which the cell rotates, and the competition between centrifugal and capillary forces results in interface destabilization. During the last two decades different aspects of the problem have been investigated, including the development of zero surface tension time-dependent exact solutions [4, 5, 6], the consideration of miscible fluid displacements [7], the dependence of pattern morphologies on viscous [8, 9] and wetting [10] effects, the influence of Coriolis force on the interfacial dynamics [11, 12], and the occurrence of complex pinch-off phenomena [13].

A suggestive variant of the usual rotating Hele-Shaw problem with nonmagnetic fluids considers that the spinning fluid is a ferrofluid [14, 15]. Its magnetic property turns out to be very handy since it introduces the possibility of controlling the rotating fluid interface by tuning an external magnetic field. The dynamics of ferrofluid droplets in rotating Hele-Shaw cells subjected to an applied azimuthal magnetic field has been studied in Refs. [21, 110]. Such a magnetic field configuration is produced by a current-carrying wire located at the center of the rotating cell, and aligned with its axis of rotation. Linear stability at early time stages [110] revealed the stabilizing role played by the azimuthal field which acts against destabilizing centrifugal effects. On the other hand, fully nonlinear stages of the advanced time dynamics both in the absence and presence of the magnetic field, have been examined by numerical simulations [21] through conformal mapping techniques.

The numerical investigation performed in [21] unveiled interesting aspects about the time evolution and morphological features of the rotating ferrofluid patterns. Under zero applied field circumstances, and considering an initially motionless Hele-Shaw cell, surface tension makes the ferrofluid droplet to assume a circular shape. However, when the cell is rotated the drop can be distorted as centrifugal forces tend to pull it apart. As the speed of rotation increases one reaches a point where the competition between surface tension and centrifugal forces causes the circular drop to become unstable, and it transforms into a two-fingered, or dumbbell-shaped, object. Further increase in rotation speed should then add a third finger, and, beyond that, four fingers. Eventually, the droplet ought to become a complex multi-fingered

structure where fingers stretch and compete. Ultimately, the formation of filamented arms presenting bulbous ends is observed, where pinch-off events tend to occur. These numerical findings are in agreement with experimental observations [8, 9] and also with phase field [13] and boundary integral simulations [111] for the rotating Hele-Shaw problem with nonmagnetic fluids.

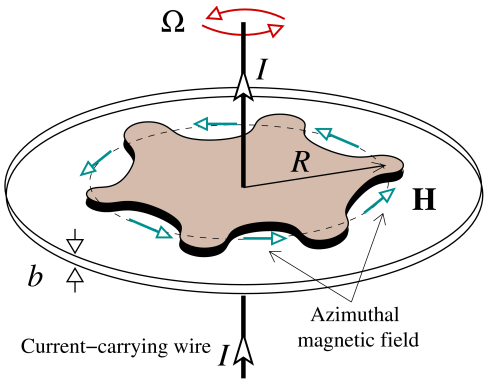

Figure 3.6: Sketch of a rotating Hele-Shaw cell of thickness b containing an initially circular magnetic fluid droplet of radius R. The in-plane azimuthal magnetic field $\mathbf{H}$ is produced by a long wire carrying an electric current I. The cell rotates with constant angular velocity $\mathbf{\Omega}$ around an axis coincident with the wire.

The scenario described above is significantly changed when the azimuthal magnetic field is turned on. The magnetic field generates a radial magnetic body force pointing inward which tends to attract the evolving ferrofluid droplet toward the current-carrying wire. The interplay of centrifugal, capillary, and magnetic effects results in the rising of a different family of morphological structures. For example, the two-fingered dumbbell obtained under the zero field situation develops a bump in the middle that gets larger for larger magnetic field magnitudes. In fact, it has been verified [21] that increasingly larger values of the magnetic field progressively reduces the number of outgrowing fingers. For a sufficiently strong field, a complete interface stabilization could be reached, and a circular shape would be recovered.

The patterns obtained in [21] are non-equilibrium shapes representing the “final" states before pinch-off. In other words, the shapes are evolving and the ferrofluid droplets are about to pinch break into multiple drops. It has also been found that, regardless the number of fingers,

the time evolution of all patterns share a peculiar feature: for large magnetic field strengths one observes a nearly circular droplet, with just one bulbous finger sticking out from it. This peculiar nonlinear phenomenon has been designated as the “diamond ring" instability.

In this section we extend the previous contributions reported in Refs. [21, 110] in some important aspects. First, instead of describing the time evolution of non-equilibrium pattern’s morphologies, we focus on the study of stationary shapes obtained when the forces involved balance equally. This offers the opportunity to contrast the shapes of time evolving and steady state structures. In addition, as opposed to [21, 110] we go beyond purely linear analysis, which does not predict stationary states, and apply a perturbative mode-coupling approach to access relevant features of the interface up to quadratic nonlinearities. This is utilized to gain analytical insight about the stability of the stationary exact solutions. The second-order approximation patterns are compared to the exact solutions, and good agreement is found even at lowest nonlinear order, and considering a small number of perturbative modes.

Furthermore, instead of addressing the influence of magnetic effects just on ferrofluids, we investigate the response of both ferrofluids and magnetorheological (MR) fluids. Ferrofluids generally behave like Newtonian liquids, but MR fluids present a strong magnetic field-dependent yield stress. Yield stress is one of the distinguishing properties of a solid, but usual fluids are not commonly known to exhibit such a property. However, nonNewtonian fluids under external driving do exhibit this behavior. This is a matter that has perhaps been known in the polymer and engineering communities for awhile, but has attracted the attention of mainstream soft matter researchers only in this decade [112, 113]. Magnetically tunable yield stress can be neglected in most existing ferrofluids [82, 83], but is very relevant in MR fluids. Here, we study how the field-dependent viscoelastic properties of the MR fluid determine the ultimate droplet shapes when they are subjected to an azimuthal magnetic field in a rotating Hele-Shaw cell. It can be seen that the difference in material properties of ferrofluids and MR fluids has a significant influence on the morphology of the emerging patterns.

It is worth pointing out that the study of Hele-Shaw pattern formation with MR fluids has been largely unexplored in the literature, and only very recently it has been performed by a couple of research groups [40, 99]. This work brings useful contributions for the better

understanding of this interesting topic in magnetohydrodynamic pattern formation.

3.2.1 Specification of the moving boundary problem

Figure 3.6 illustrates an incompressible, magnetic fluid droplet of unperturbed radius R, viscosity η, and density ρ located between two narrowly spaced flat plates of a Hele-Shaw cell of thickness b. The outer fluid is nonmagnetic and has negligible viscosity and density. The surface tension at the fluid-fluid interface is denoted by γ. We consider that the droplet is subjected to an azimuthal magnetic field produced by a long straight current-carrying wire that is perpendicular to (coaxial with) the plates of the Hele-Shaw cell

$$\mathbf{H} = \frac{I}{2\pi r}\,\hat{\mathbf{e}}_{\varphi}. \tag{3.24}$$

The electric current is represented by I, r is the radial distance from the origin of the coordinate system (located at the center of the cell), and $\hat{\mathbf{e}}_{\varphi}$ is a unit vector in the azimuthal direction. The azimuthal angle in the plane of the cell is denoted by φ. A stabilizing magnetic body force $\sim \nabla H$, where $H = |\mathbf{H}|$, acts on the fluid pointing in the inward radial direction [14, 110]. The cell rotates with constant angular velocity Ω about an axis perpendicular to the plane of the flow, and directed along the wire. The centrifugal force points radially outward and tends to spread the droplet out.

Following the standard approach in Hele-Shaw problems, one starts by neglecting inertial contributions in the 3D Navier-Stokes equation, and by imposing a no-slip boundary condition at the cell plates. Then, by taking a parabolic velocity profile, an effectively 2D flow is obtained by averaging the 3D Navier-Stokes equation over the cell gap direction. By considering the contribution of centrifugal [8], magnetic [16, 17] and viscoelastic effects [32, 85], plus the existence of a magnetic field-dependent yield stress $\sigma_y = \sigma_y(H)$ [40, 86, 87, 88], one can write a modified Darcy's law for the gap-averaged velocity $\mathbf{v}$ of the confined magnetic fluid

$$\mathbf{v} = -\frac{b^2}{12\eta}\left[\nabla\left(\Pi - \frac{\rho\Omega^2 r^2}{2}\right) + \frac{3\sigma_y(H)}{b}\,\hat{\mathbf{e}}_r\right]. \tag{3.25}$$

As in Eq. (3.2), the derivation of Eq. (3.25) assumes the regime of high viscosity compared to yield effects, and prevalent yielding occurring along the radial direction, defined by the unit vector $\hat{\mathbf{e}}_r$. Note that one recovers the usual Darcy's law for Newtonian ferrofluids in a motionless Hele-Shaw cell ($\Omega = 0$) [16, 17] by setting the yield stress contribution $\sigma_y(H) = 0$. We point out that, despite the nonNewtonian character of the MR fluid (due to its sizable yield stress), we consider that it presents a constant viscosity. This assumption enables the flow to stay potential.

In Eq. (3.25) the gap-averaged generalized pressure Π is defined as (3.3), where P is the 3D hydrodynamic pressure and Ψ represents the magnetic pressure. We also assume a linear relationship $\mathbf{M} = \chi\mathbf{H}$, and that the magnetic field-dependent yield stress is given by (3.5).

Since the velocity field is irrotational in the bulk, it is convenient to state our moving boundary problem in terms of a velocity potential ϕ, where $\mathbf{v} = -\nabla\phi$. This allows one to recognize both sides of Eq. (3.25) as gradients of scalar fields, so that it can be rewritten in a *dimensionless* form as

$$\phi = p - \frac{\chi N_B}{r^2} - N_\Omega r^2 + S_0 r - \frac{S}{r}, \tag{3.26}$$

where p is the gap-averaged hydrodynamic pressure. The system is characterized by four dimensionless parameters

$$\begin{aligned} N_B &= \frac{\mu_0 I^2}{8\pi^2\gamma r_0},\ N_\Omega = \frac{\rho\Omega^2 r_0^3}{2\gamma}, \\ S_0 &= \frac{3\sigma_{y0} r_0^2}{\gamma b},\ S = \frac{3\alpha I^2}{4\pi^2\gamma b}. \end{aligned}$$

The parameter N_B represents the magnetic Bond number, and measures the ratio of magnetic to capillary forces. On the other hand, the interplay between centrifugal and surface tension effects is described by a rotational Bond number N_Ω. Moreover, S_0 and S are related to the yield stress contributions at zero, and nonzero applied magnetic field, respectively. In Eq. (3.26) lengths and velocities are rescaled by r_0, and $\gamma b^2/(12\eta r_0^2)$, respectively. As in Ref. [40] we adopt the typical length scale r_0 as being of the order of the unperturbed droplet radius R.

Note that from this point on, we work with the dimensionless version of the equations. We stress that in the presentation of our results in Secs. 3.2.2 and 3.2.3 we make sure that the values of all relevant dimensionless quantities we utilize are consistent with realistic physical parameters [40, 87, 88, 96, 97] related to existing magnetic field arrangements, and material properties of ferrofluids and MR fluids.

By examining Eq. (3.26) it is evident that the only destabilizing contribution comes from the action of the centrifugal force (term proportional to N_Ω). In contrast, the azimuthal magnetic field term involving N_B, which is originated from the magnetic pressure Eq. (3.4), has a stabilizing role. This can be also said about the yield stress pieces derived from Eq. (3.5): both the zero field (S_0) and the field-dependent (S) yield stress terms tend to restrain interface destabilization.

Another important piece of information is provided by the augmented Young-Laplace pressure jump boundary condition

$$\Delta p = \kappa - \frac{N_B \chi^2}{r^2}(\hat{\mathbf{n}} \cdot \hat{\mathbf{e}}_\varphi)^2, \tag{3.27}$$

where $\hat{\mathbf{n}}$ denotes the unit normal vector to the interface. The first term on the right-hand side of Eq. (3.27) represents the usual contribution related to surface tension and the in-plane interfacial curvature κ. The second term in Eq. (3.27) is set by the so-called magnetic normal traction [14, 15], which considers the influence of the normal component of the magnetization at the interface, and its linear relation to the applied magnetic field.

From the incompressibility condition $\nabla \cdot \mathbf{v} = 0$ it can be verified that the velocity potential is Laplacian. Therefore, the definition of the moving boundary problem is specified by the following equations

$$\nabla^2 \phi = 0, \tag{3.28}$$

$$\frac{\partial \phi}{\partial n}|_{in} = \frac{\partial \phi}{\partial n}|_{out}, \tag{3.29}$$

$$\frac{\partial \phi}{\partial s}|_{in} - \frac{\partial \phi}{\partial s}|_{out} = \Gamma, \tag{3.30}$$

where the subscripts label the inner (*in*) and outer (*out*) fluids, and $\partial/\partial s = \partial_s$ ($\partial/\partial n = \partial_n$) is

the derivative along the tangent (normal) direction to the interface. Equation (3.29) describes the continuity of the normal velocity at the interface, and Eq. (3.30) its tangential jump of magnitude Γ. This jump originates a nonzero vorticity region restricted to the interface separating the fluids [94, 95]. With the help of the generalized Darcy's law Eq. (3.26), and the pressure jump Eq. (3.27) an explicit expression for the vortex sheet strength can be derived yielding

$$\begin{aligned} \Gamma &= 2\partial_s \left\{ \kappa - \frac{\chi N_B}{r^2}[1+\chi(\hat{\mathbf{n}}\cdot\hat{\mathbf{e}}_\varphi)^2] - N_\Omega r^2 + S_0 r - \frac{S}{r} \right\} \\ &- \left(\frac{\partial \phi}{\partial s}|_{in} + \frac{\partial \phi}{\partial s}|_{out} \right). \end{aligned} \tag{3.31}$$

Equation (3.31) is the starting point for the calculation of the steady shapes that will be examined in Sec. 3.2.2.

3.2.2 Exact stationary solutions

3.2.2.1 Access to fully nonlinear steady shapes

The possibility of obtaining exact stationary solutions provides a useful way to access fully nonlinear features of the patterns' morphologies through a relatively simple method, which does not rely on complicated numerical simulations. The physical and geometric properties of a special family of curves associated with the motion of a nonmagnetic fluid interface in a rotating Hele-Shaw cell have been recently studied [13, 68, 98]. Such a family of stationary exact solutions with *nonzero* surface tension consists of interface shapes which balance exactly the competing capillary and centrifugal forces. The outcome is the formation of fully nonlinear patterns presenting fingers that assume a teardrop-like shape, and eventually tend to be detached from the main body of the rotating fluid characterizing a pinch-off phenomenon.

A generalized set of exact steady shapes can be obtained when a confined ferrofluid, or a MR fluid droplet is subjected to a radial magnetic field. As in the centrifugally-driven case, the radial field acts to destabilize the system. In these magnetohydrodynamic situations the

emerging stationary solutions result from the balance of centrifugal, capillary, magnetic, and viscoelastic effects. Within this context, different morphologies have been found including starfish-like [24] structures, and bulgy polygonal shapes [40].

As in Refs. [24, 40, 68, 98] we apply a vortex-sheet formalism [94, 95] to get the exact stationary shapes obtained when a rotating droplet of a confined magnetic fluid is subjected to an azimuthal magnetic field. This type of exact solutions can be found by imposing a condition of zero vorticity ($\Gamma = 0$) plus considering a stationary state ($\partial\phi/\partial s|_{in} = \partial\phi/\partial s|_{out} = 0$) in Eq. (3.31). Under such circumstances, we find that the curvature of the magnetic fluid interface satisfies a nonlinear ordinary differential equation which can be readily integrated yielding

$$\begin{aligned} \kappa(r,\cos\psi) &= a + \frac{\chi N_B}{r^2}[1+\chi\cos^2\psi] \\ &+ N_\Omega r^2 - S_0 r + \frac{S}{r}, \end{aligned} \tag{3.32}$$

where a is a constant of integration. In Eq. (3.32) we have used $\hat{\mathbf{n}}\cdot\hat{\mathbf{e}}_\varphi = \pm\cos\psi$. The main purpose of our study is to investigate the fully nonlinear family of planar curves whose curvature has the general form given by Eq. (3.32). Different morphologies can be obtained by manipulating the relevant control parameters of the problem, namely N_B, χ, N_Ω, S_0, S, the constant a, and the specifications $r_0 = r(s=0)$, $\varphi_0 = \varphi(s=0)$, and $\psi_0 = \psi(s=0)$, where s denotes the arclength. For a more detailed account of the numerical approach used to solve the type of differential equation leading to (3.32) we refer the reader to Ref. [98].

A relevant aspect about the type of exact solutions we study here refers to their stability. The great majority of the exact steady shapes computed in Refs. [24, 40, 68, 98] are unstable. The only exception is the somewhat exotic shape presenting cusplike protrusions presented in Ref. [13]. Here, however, we have at our disposal tunable stabilizing effects provided by the azimuthal magnetic field and field-induced yield stress. Within this context it is of interest to examine how these controllable effects can affect the stability of the exact solutions. The analysis of the stability of these steady exact solutions will be examined in Sec. 3.2.3. Another important point is related to the usefulness of the exact steady shapes, and how their morpholo-

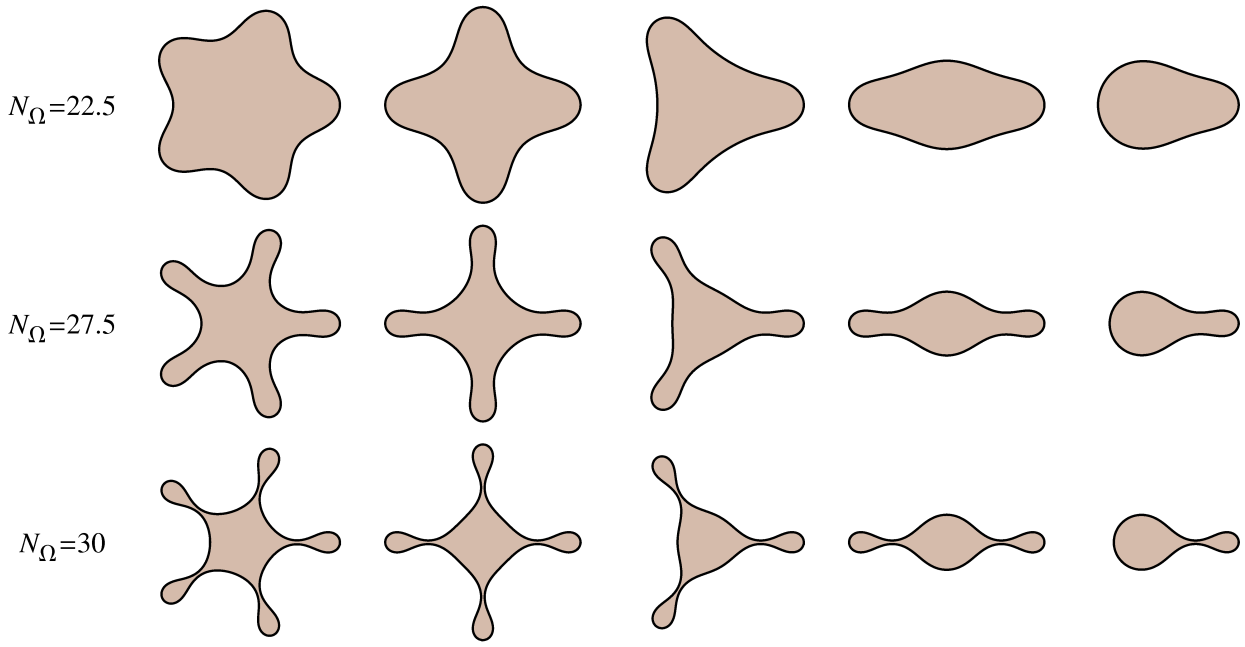

Figure 3.7: Typical stationary shape solutions for a Newtonian ferrofluid droplet ($S_0 = S = 0$), and three different values of the rotational Bond number N_Ω. The intensity of the magnetic Bond number N_B increases from left to right.

gies compare to corresponding time-evolving patterns obtained by numerical simulations [21].

3.2.2.2 Newtonian ferrofluid

We initiate our analysis of the possible exact stationary shapes by focusing on the situation in which the magnetic fluid is a Newtonian ferrofluid, so that yield stress effects are negligible ($S_0 = S = 0$). This is related to the situation that has been examined in Ref. [21] where the time evolution of a ferrofluid rotating droplet has being described numerically. To investigate the role played by the magnetic Bond number N_B on the shape of the patterns, in Fig. 3.7 we present a prototypical compilation of possible exact stationary solutions for three distinct values of the rotational Bond number: N_Ω=22.5 (first row), N_Ω=27.5 (second row), and N_Ω=30 (third row). For a given N_Ω the magnitude of N_B increases from left to right: $6.6250 \leq N_B \leq 7.3731$ (first row), $4.3485 \leq N_B \leq 4.4090$ (second row), and $3.4529 \leq N_B \leq 3.4680$ (third row). The rest of the parameters assume the following values: $\chi = 0.5$, $\psi_0 = \pi/2$, $r_0 = 1$, and the arbitrary

constant $a = -21.0786$.

Before proceeding, we call the reader's attention to two important points: first, we emphasize that the set of patterns illustrated in Figs. 3.7 and 3.8 represent a series of separate stationary shapes, and *not* a time evolving sequence of events. In addition, as it is apparent from these figures, the areas of the various patterns are not necessarily the same. To circumvent the constant area constraint, as in Ref. [40] we conveniently choose a characteristic radial distance r_0 as a parameter to rescale lengths in our problem. The parameter r_0 can be taken as either the minimum or the maximum radial distance defined for a given stationary shape [98]. For each exact pattern, the unperturbed radius R is determined by the circle of equivalent area. All this is done without loss of generality.

The stabilizing nature of the azimuthal field is quite evident in Fig. 3.7: regardless the value of N_Ω, the number of fingering structures tend to decrease from 5 to 1 as N_B is increased. For lower values of the rotational Bond number (N_Ω=22.5) one observes the formation of patterns containing smooth fingers which are relatively thick at their "necks". As centrifugal effects increase in intensity (N_Ω=27.5) the fingers are more powerfully pushed outward, and thinner necks develop. If such effects are further increased (N_Ω=30) bulbous fingers having very thin necks (which are about to pinch-off) arise. Of course, if even larger values of N_Ω are used the interface boundaries would overlap, representing nonphysical solutions.

For any given value of N_Ω the central part of the segments connecting adjacent fingers tend to be flattened out as N_B increases, changing from concave to convex. This is responsible to the formation of small bumps of fluid between neighboring fingers. Despite the fact that all these patterns represent stationary (equilibrium) shapes, non-equilibrium structures that have been previously obtained in Ref. [21] for the time evolution of the system are recovered: for instance, single fingered ("diamond ring") patterns, and twofold morphologies with a bump in the middle can be readily identified in Fig. 3.7 for higher values of N_B. In real experiments and time-evolving numerical descriptions the initial conditions are usually nonsymmetric, so that fingers compete and advance over others. However, it seems reasonable to speculate that if one runs numerical simulations like those performed in Ref. [21] with non-random noise, and instead used a symmetric initial disturbance, the resulting time evolving patterns would look

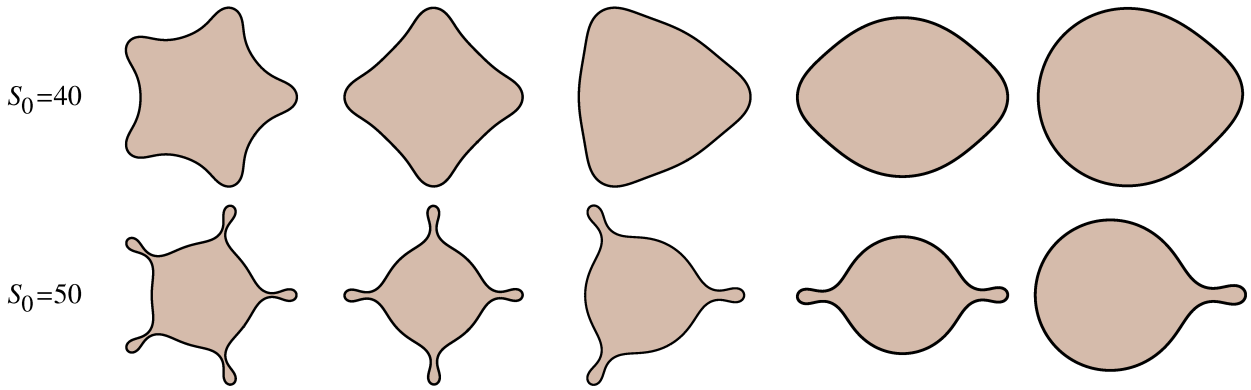

Figure 3.8: Typical stationary shape solutions for a MR fluid droplet, and two different values of the zero field yield stress parameter S_0. Both N_B and N_Ω are kept fixed, while the field-induced yield stress parameter S increases from left to right.

similar to the steady state structures depicted in Fig. 3.7.

3.2.2.3 Magnetorheological fluid

We move on by investigating the influence of viscoelastic and magnetically-induced yield stress effects on the shape of the exact solutions. In order to do that, in Fig. 3.8 we turn to the situation in which the confined magnetic liquid is a MR fluid. So, now both the zero field yield stress parameter S_0, and its field-induced counterpart S will assume nonzero values. Here we fix the value of the magnetic Bond number ($N_B = 3.4529$), and consider two different characteristic values for S_0: 40 (first row) and 50 (second row). On the other hand, the value S increases from left to right: $28.458 \leq S \leq 30.352$ (first row), and $39.906 \leq S \leq 40.352$ (second row). The rotational Bond number is fixed at N_Ω=30, and all the other parameters are the same as the ones used in Fig. 3.7. Under such circumstances, any changes in the shape of the patterns can be attributed to the yield stress effects introduced by the parameters S_0 and S.

By inspecting Fig. 3.8 one can immediately notice that the morphologies obtained for MR fluids are considerably different from those of ferrofluids (Fig. 3.7). The resulting exact shapes constitute N-fold structures, where the number of fingers decrease for larger values of S. Moreover, as S is increased more and more fluid is concentrated around the current-carrying wire

(center of the droplet). This occurs because the effect of the attracting magnetic body force is now supplemented by the stabilizing field-induced yield stress which is inversely proportional to the squared radial distance to the wire. One of the most evident features for the patterns obtained for $S_0 = 40$ is the fact that they look a bit “swollen" as compared to those obtained in Fig. 3.7. As S increases the segments connecting the resulting short fingers tend to bulge outward, leading to morphologies not really characterized by a neck formation. For example, for one-, two-, and threefold structures there is so much fluid located around the center of the drop that only slightly protruded structures emerge. However, when $S_0 = 50$ still another kind of shapes arise, now showing a lot of MR fluid concentrated in the bulk, connected through necks to small droplets which are not as inflated as the ones observed in Fig. 3.7 for $N_\Omega = 30$.

Unfortunately, to date there are neither experiments nor time evolving numerical simulations for MR fluid droplets in rotating Hele-Shaw cells, so that we could compare their specific shapes to the exact stationary solutions depicted in Fig. 3.8. For the same reasons as those discussed at the end of Sec. 3.2.2.2, it would not be completely surprising to find morphological similarities between the steady patterns shown in Fig. 3.8 and eventual time evolving shapes simulated for symmetric initial conditions.

3.2.3 Mode-coupling approach and the stability of the exact solutions

Impelled by the morphological similarities found between some of the exact stationary solutions discussed in Sec. 3.2.2, and the time evolving shapes obtained in Ref. [21], we employ a perturbative mode-coupling approach [61] to gain analytical insight about the stability of the exact stationary solutions. In this context, the stationary approximate interface obtained with a weakly nonlinear analysis can be compared with the fully nonlinear exact steady shapes, as long as the lengths of the fingers are not too large. We discuss to what extent a few perturbative orders can account for the entire exact solution and hence, a certain truncation in the number of Fourier modes involved can be regarded as a good representation of the exact shapes.

Within our mode-coupling approach the perturbed shape of the interface can be described as $\mathscr{R}(\varphi,t) = R + \zeta(\varphi,t)$, where $\zeta(\varphi,t) = \sum_{n=-\infty}^{+\infty} \zeta_n(t)\exp(in\varphi)$ represents the net interface

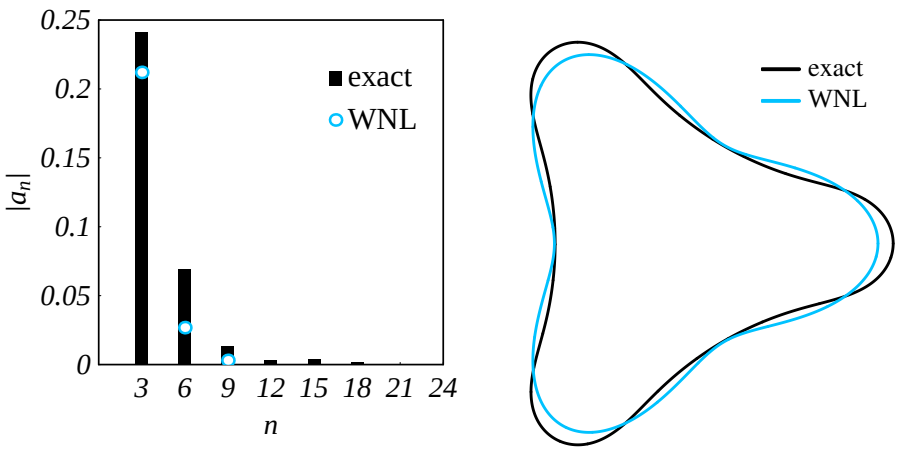

Figure 3.9: Newtonian ferrofluid situation. Left panel: cosine Fourier amplitudes as a function of the azimuthal mode number n. Right panel: comparison between exact and weakly nonlinear (WNL) solutions for the steady interface shape.

perturbation with complex Fourier amplitudes $\zeta_n(t)$, and discrete azimuthal wave numbers n. The zeroth mode is included in the Fourier expansion to keep the area of the perturbed shape independent of the perturbation ζ.

We define Fourier expansions for the velocity potential, and use the boundary conditions presented in Sec. 3.2.1 to express ϕ in terms of ζ_n to obtain a dimensionless mode-coupling differential equation for the system (for $n \neq 0$), accurate to second-order in the perturbation amplitudes. We present the evolution of the perturbation amplitudes as

$$\begin{aligned} \dot{\zeta}_n &= \lambda(n)\zeta_n \\ &+ \sum_{n' \neq 0} [F(n,n')\ \zeta_{n'}\zeta_{n-n'} + G(n,n')\ \dot{\zeta}_{n'}\zeta_{n-n'}], \end{aligned} \tag{3.33}$$

where the overdot represents a total time derivative with respect to time,

$$\lambda(n) = |n| \left[2N_\Omega - \frac{2N_B\chi}{R^4} - \frac{(n^2-1)}{R^3} - \frac{S_0}{R} - \frac{S}{R^3} \right] \tag{3.34}$$

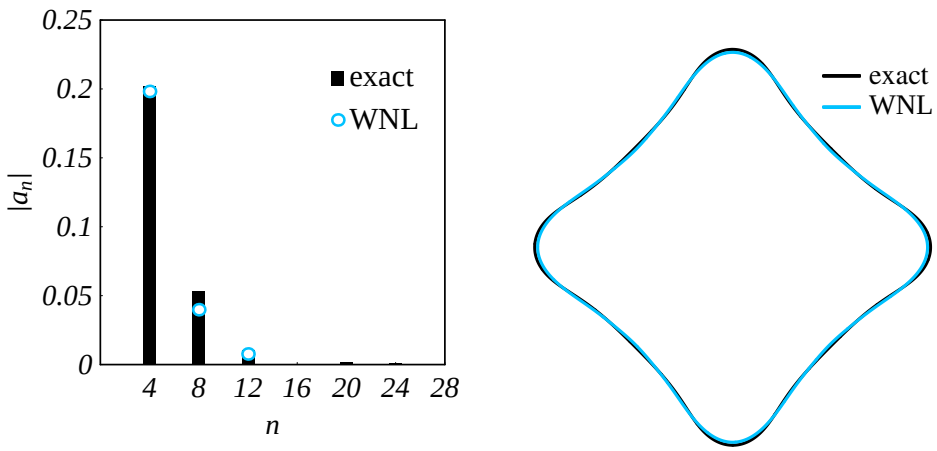

Figure 3.10: Magnetorheological fluid situation. Left panel: cosine Fourier amplitudes as a function of the azimuthal mode number n. Right panel: comparison between exact and weakly nonlinear (WNL) solutions for the steady interface shape.

denotes the linear growth rate, and the functions $F(n,n')$ and $G(n,n')$ are the second order mode-coupling terms given by

$$\begin{aligned} F(n,n') &= \frac{|n|}{R}\left\{N_\Omega + \frac{\chi N_B}{R^4}[3+\chi n'(n'-n)]\right. \\ &- \left.\frac{1}{R^3}\left[1-\frac{n'}{2}(3n'+n)\right]+\frac{S}{R^3}\right\}, \end{aligned} \tag{3.35}$$

and

$$G(n,n') = \frac{1}{R}\{|n|[\mathrm{sgn}(nn')-1]-1\}. \tag{3.36}$$

By examining Eq. (3.34) for the linear growth rate, it is clear that the only destabilizing term is the one related to the centrifugal driving. Azimuthal field, surface tension, and yield stress effects act to restrain interface deformation. The terms appearing in the expression for the function $F(n,n')$ in Eq. (3.35) arise from the centrifugal force, magnetic applied field, surface tension, and field-dependent yield stress, respectively. The term proportional to χ^2 comes from the square of the projection of the interface normal in the azimuthal direction in the pressure jump condition [Eq. (3.27)]. The function $G(n,n')$ defined in Eq. (3.36) couples

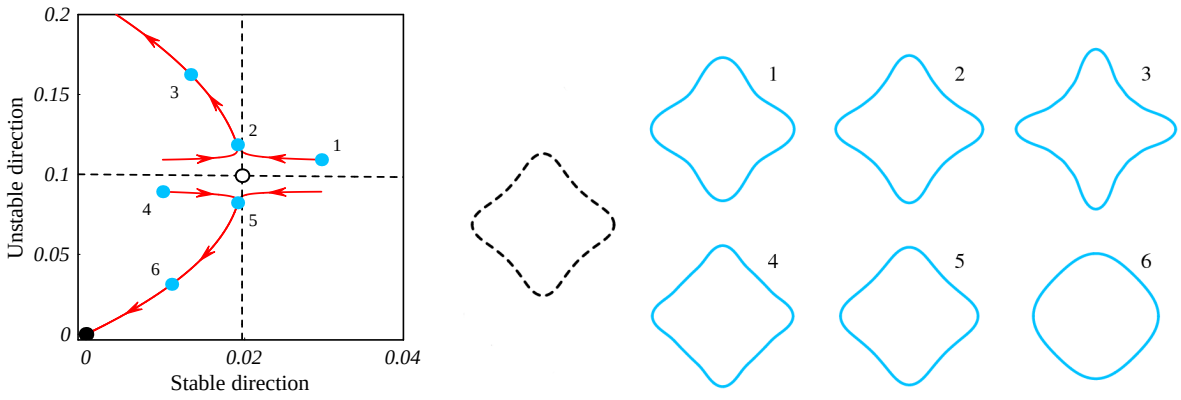

Figure 3.11: Left panel: 2D phase portrait. Right panel: time evolving weakly nonlinear patterns (solid interfaces) for two different initial conditions (1 and 4). The dashed interface represents the saddle point associated to the MR fluid weakly nonlinear pattern shown in Fig. 3.10.

the perturbed flow $\dot{\zeta}$ with the interface shape perturbation ζ, and presents no dependence on magnetic effects. Already at second order, and by using just a few modes we are able to obtain stationary solutions of small perturbation amplitudes.

Figure 3.9 illustrates a comparison between exact stationary shapes and the weakly nonlinear (WNL) steady solutions obtained from Eq. (3.33). We begin by focusing on the threefold ferrofluid pattern presented in the first row of Fig. 3.7 for which $N_\Omega = 22.5$. For this lower value of N_Ω the exact shape is not very perturbed, so that the interface position is a single valued function of the azimuthal angle φ, and the weakly nonlinear approach can be applied. Note that for higher values of N_Ω shown in Fig. 3.7 the resulting patterns become too deformed, so that a Fourier analysis is no longer valid.

The left panel in Fig. 3.9 presents the absolute value of the cosine Fourier amplitudes a_n for various modes n. The data represented by the bars in black are extracted directly from the fully nonlinear threefold pattern in the first row of Fig. 3.7. The cosine and sine amplitudes are defined as $a_n = \zeta_n + \zeta_{-n}$, and $b_n = i\,(\zeta_n - \zeta_{-n})$, respectively. As expected from the symmetry properties and commensurability of the exact solutions, the magnitudes of the sine amplitudes are much smaller than the cosine ones (typically one thousand times smaller), so that they can be safely neglected. The Fourier spectrum of the exact solution demonstrates that the cosine

amplitudes drop quickly as n is increased, in such a way that it is very well described by only three harmonic modes, namely, N, $2N$, and $3N$, where $N = 3$. The open circles express the approximate values of the stationary cosine amplitudes by considering the interplay of these three particular Fourier modes, using the mode-coupling equation (3.33) and setting its time derivative terms to zero. Note this procedure is equilavent of expanding Eq. (3.32) up to second order in the perturbation amplitudes.

The right panel in Fig. 3.9 contrasts the exact shape and the stationary weakly nonlinear solution by utilizing the data shown in the left panel. By inspecting Fig. 3.9 we see that the weakly nonlinear theory works reasonably well in approaching the exact interface shape, even though only three modes are used at the lowest nonlinear order. Similar type of results can be obtained by considering the coupling of only three modes for N-fold patterns with $N \geq 3$. However, for the stationary shapes in Fig. 3.7 presenting one or two protusions, a good weakly nonlinear representation of the exact solution requires the consideration of a higher number of participating modes (five modes for the twofold pattern, and nine modes for the onefold shape).

Similarly to the case of ferrofluids, Fig. 3.10 depicts the behavior of the cosine Fourier amplitudes for varying n (left panel), and the comparison between exact and weakly nonlinear shapes (right panel) for a magnetorheological fluid. We consider the fourfold exact pattern in the first row of Fig. 3.8, and describe the weakly nonlinear solution by assuming the coupling of three modes N, $2N$, and $3N$, where $N = 4$. Here the general conclusions are analogous to the ones we have presented for the ferrofluid case (Fig. 3.9), but the accordance between exact and weakly nonlinear solutions are even better for the MR fluid situation. This is due to the fact that, in addition to the stabilizing role played by the applied azimuthal field, the field-dependent yield stress contributes to the emergence of further stabilized morphologies. Once again, N-fold patterns with $N \geq 3$ are very well described by considering three harmonic modes. However, for $N = 1$ and $N = 2$ a larger number of modes is necessary for a satisfatory weakly nonlinear description of the exact shapes (four modes for the twofold pattern, and eleven modes for the onefold shape).

Now we turn to one last, and important aspect related to the stability of the stationary solutions. Despite the stabilizing role of both applied azimuthal field and magnetic field-dependent

yield stress, we have verified that the steady solutions are unstable. This is done by setting a system of nonlinear differential equations for three cosine harmonic modes N, $2N$, and $3N$, and by using the mode-coupling equation (3.33). Through a standard linearization process close to the stationary solution, we diagonalize the resulting system of equations, determining the eigenvalues which dictate the stability of the fixed point [66]. For any given pattern we have two negative eigenvalues, and one positive, characterizing a 3D saddle-point. Within this scenario we find that the unperturbed (circular) interface is indeed stable. Therefore, if one perturbs a stationary solution it can either relax to a circle or evolve to an increasingly deformed multifingered pattern whose resulting fingers ultimately tend to pinch-off. These generic features are similar to what has been observed in Refs. [13, 68] for the exact stationary solutions obtained in rectangular and rotating Hele-Shaw problems with nonmagnetic fluids.

The characteristic unstable signature of the stationary solutions is illustrated in Fig. 3.11. On the left panel we show a projection of the phase portrait on a 2D subspace determined by two eigenvectors of the stationary solution, which establish stable and unstable directions. These directions are indicated by dashed lines. The dot filled in black corresponds to an attractor, and it is associated to the stable circular interface. On the other hand, the white dot represents a saddle-point which refers to the fourfold MR fluid weakly nonlinear pattern shown in Fig. 3.10. The solid curves represent the trajectories of the system on such 2D phase space for different initial conditions close to the saddle-point. The remaining dots (1-2-3, and 4-5-6) exemplify subsequent time evolving events determined by initial conditions 1 and 4. The right panel depicts the weakly nonlinear shapes related to the paths 1-2-3, and 4-5-6 shown on the left panel. In addition, the dashed pattern refers to the saddle-point situation. It is evident that above the basin of attraction of the stable node the fingered patterns tend to grow (trajectory, and patterns 1-2-3), and below it they move toward a stable circular interface (trajectory, and patterns 4-5-6).

We stress that the nontrivial exact stationary shapes we study in this work are obtained under circumstances associated to a linearly stable regime. This means that is not possible to obtain these exact steady shapes from the time evolution of a nearly circular initial state. However, if one sets an initial condition sufficiently close to the stationary solution, a slowing

down of the dynamics would be detected leading to a circle or to growing fingers. It is also worth noting that all the stationary solutions found in this chapter are indeed unstable.

CHAPTER 4

Darcy's law formulation for Bingham fluids

It is well known that when a less viscous fluid pushes a more viscous one in the confined geometry of a Hele-Shaw cell, the interface separating the fluids develops the Saffman-Taylor instability [1] leading to the formation of fingerlike patterns [2]. The specific morphology of these patterns depend on the nature of the fluids, and on the geometry of the flow. Most of the existing studies on the viscous fingering instability refer to Newtonian fluids. In this case, the resulting interfacial shapes range from a single, smooth, steady-state finger in rectangular (or, channel) geometry [92, 94, 114, 115, 116, 117, 118, 119, 120], to multi-fingered structures in which repeated tip-splitting produces highly ramified patterns in the radial flow setup [61, 121, 122, 123, 124, 125, 126, 127, 128, 129, 130, 131]. These pattern forming phenomena have been extensively studied during the last fifty years through analytical calculations, numerical simulations, and experiments.

Although not as numerous as in the Newtonian fluid case, other Hele-Shaw flow investigations have revealed that a distinct variety of patterns can be formed when one of the fluids is nonNewtonian [132]. While Newtonian fluids are characterized by a constant viscosity, non-Newtonian fluids display a multiplicity of hydrodynamic behaviors ranging from elasticity and plasticity to shear thinning and shear thickening, and in general have a shear-dependent viscosity.

The rheological properties of nonNewtonian fluids exert a profound effect on the shape of the emerging interfacial patterns in Hele-Shaw flows. Rectangular and radial Hele-Shaw experiments involving nonNewtonian fluids like polymer solutions, liquid crystals, clays and foams unveiled pattern morphologies presenting snowflake-like shapes [133] and fracturelike structures [134, 135]. For shear-thinning fluids traditional finger tip-splitting events are inhibited, and the appearance of dendritic patterns with side branching is favored. Cracklike patterns presenting angular branches and sharp tips have also been found. On the other hand, flow with

shear-thickening fluids [136] displays patterns similar to those found in Newtonian fluids but with either narrowing or widening of the fingers, which can present asymmetric humps. This morphological diversity and rich dynamical behavior motivated a number of theoretical studies of the problem through linear and weakly nonlinear analyzes, and sophisticated numerical simulations [137, 138, 139, 140, 141, 142, 143, 144, 145, 146].

Despite all the efforts and important results obtained by researchers on the development of viscous fingering in nonNewtonian Hele-Shaw flows, the pattern forming dynamics with yield stress fluids has been relatively underlooked. In contrast to Newtonian fluids, yield stress fluids [30, 31] can support shear stresses without flowing. As long as the stress remains below to a certain critical value they do not flow, but respond elastically to deformation. So, such materials possess properties of both viscous fluids and elastic solids, behaving like a “semi-solid". On the theoretical side, a linear stability analysis of the Saffman-Taylor problem in rectangular and radial cells with yield stress fluids [32] has predicted that the instability can be drastically modified. On the experimental arena some interesting findings have been disclosed in channel geometry [33, 34]: depending on whether viscous effects or yield stresses dominates, fractal patterns, or ramified structures where multiple fingers propagate in parallel may arise.

In a more recent experimental work [147] fingering in a yield stress fluid in rectangular as well as in radial Hele-Shaw cells has been examined. As in Ref. [33, 34], different regimes leading to diverse pattern morphologies have been observed: at low velocities (where yield stress dominates) ramified structures arise; however, for higher velocities (viscous effects prevail), in addition to tip-splitting, interesting side branching instabilities become apparent. Although the behavior at the low velocity regime can be quantitatively explained from the linear stability results presented in Ref. [32], the nonlinear side branching and tip-splitting instabilities detected at higher velocities are not fully understood to date. So, a theoretical study addressing these suggestive pattern forming phenomena in yield stress fluids is still lacking.

In this Chapter we carry out the analytical weakly nonlinear analysis of the problem in which a yield stress fluid flows in a radial Hele-Shaw cell. We focus on the regime in which viscosity effects are prevalent over yield stress. By exploring the onset of nonlinear effects we try to gain analytical insight into the dynamic process of fingering formation. In particular,

we seek to understand how mode-coupling dynamics leads to basic morphological features and behaviors observed experimentally in such nonNewtonian Hele-Shaw flows [147].

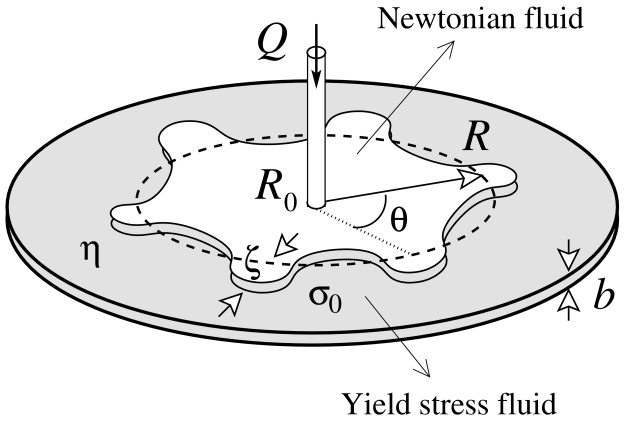

Figure 4.1: Schematic configuration of radial flow in a Hele-Shaw cell. The inner fluid is Newtonian and has negligible viscosity. The outer fluid is a yield stress fluid. The unperturbed fluid-fluid interface (dashed curve) is a circle of radius R. All physical parameters are defined in the text.

The Hele-Shaw cell is depicted in Fig. 4.1 and consists of two parallel plates separated by a small distance b. Consider the displacement of a nonNewtonian fluid of viscosity η and yield stress σ_0, by a Newtonian fluid of negligible viscosity in such confined geometry. The surface tension between the fluids is denoted by γ. The Newtonian fluid is injected at a constant areal flow rate Q at the center of the cell, along the direction perpendicular to the plates (z-axis).

We focus on deriving the relevant hydrodynamic equation for a Hele-Shaw flow of a yield stress fluid. Our main goal is to obtain a Darcy's like law which relates the gap-averaged velocity with the pressure gradient and the yield stress, taking into account the coupling between them. We start by taking the Navier-Stokes equation for an incompressible viscous fluid [148]

$$\rho\left[\frac{\partial \mathbf{u}}{\partial t}+(\mathbf{u}\cdot\nabla)\mathbf{u}\right]=-\nabla P-\nabla\cdot\tau, \tag{4.1}$$

where ρ is density, $\mathbf{u}$ denotes the three-dimensional velocity, P is the pressure, and τ represents the stress tensor that includes the yield stress. In the scope of the lubrication approximation, where the distance between the plates b is much smaller than the unperturbed radius R of the

fluid-fluid interface, the motion is a creeping flow. Therefore, we may neglect the inertial terms between square brackets in Eq. (4.1), as well as impose that the prevailing terms in $\nabla \cdot \tau$ are those with transversal derivatives. Within this framework, we also consider that pressure is constant along the transversal direction (z-axis). Thus, by integrating (4.1) we obtain

$$\tau_{iz} = \left| \frac{b}{2} - z \right| \nabla_i P, \tag{4.2}$$

where $i = r, \theta$ is the label that indicates polar radial or azimuthal components, with the origin placed at the center of the droplet. We have used the symmetry of the flow to state that the shear stress is zero at the mid-plane $z = b/2$ (since the plates are located at $z = 0$ and $z = b$).

Furthermore, as a constitutive relation for yield stress fluids, we use the Bingham model [132]. It states that, for a given shear stress higher than the fluid yield stress magnitude σ_0, there is flow and the stress tensor is given by

$$\tau_{iz} = -\left[\eta \frac{\partial u_i}{\partial z} + \sigma_i \right]. \tag{4.3}$$

This situation corresponds to $|\tau| > \sigma_0$, where $|\tau| = \sqrt{\tau_{rz}^2 + \tau_{\theta z}^2}$. We point out that, in contrast to previous works [40, 41, 85, 149], here we allow the yield stress to exhibit both r and θ polar components, in such a way that its response is now opposite to the stress tension. This is precisely what will allow us to couple the yield stress to the velocity direction by the end of our derivation. From Eq. (4.2) we see that the stress tension is parallel to pressure gradient and we may write $\sigma_i = -\sigma_0 \, \nabla_i P / |\nabla P|$.

On the other hand, if $|\tau| \leq \sigma_0$, the shear stress do not overcome the yield stress, thus there is no flow

$$\frac{\partial u_i}{\partial z} = 0, \tag{4.4}$$

meaning that $\sigma_i = -\tau_{iz}$.

Since the problem is symmetric with respect to the mid-plane $z = b/2$, we may assume $0 \leq z \leq b/2$ for simplicity. From Eq. (4.2) we find the critical height z_c which separates the

sheared region from the unsheared region

$$z_c = \frac{b}{2} - \frac{\sigma_0}{|\nabla P|}. \tag{4.5}$$

Then, by using Eq. (4.2) and the profile velocity continuity at $z = z_c$, it is possible to determine the velocity profile for both regions

$$\begin{aligned} \mathbf{u} &= -\frac{\nabla P}{\eta}\left[z\left(z_c - \frac{z}{2}\right)\right] \text{ for } 0 \leq z < z_c, \\ \mathbf{u} &= -\frac{\nabla P}{\eta}\frac{z_c^2}{2} \text{ for } z_c \leq z \leq \frac{b}{2}. \end{aligned} \tag{4.6}$$

It is well known that this velocity profile cannot be exact for different kind of flows [150, 151, 152]. However, the expression given by (4.6) is a good approximation when one only seeks the relationship between the pressure drop and the mean velocity [32], which is exactly our case.

We define the gap-averaged velocity as

$$\mathbf{v} = \frac{1}{b}\int_0^b \mathbf{u}\, dz, \tag{4.7}$$

and by gap-averaging (4.6) we finally obtain a dimensionless modified Darcy's law for yield stress fluids

$$\mathbf{v} = -\nabla P\left[1 - \frac{\delta}{|\nabla P|} + \frac{4\,\delta^3}{27|\nabla P|^3}\right]. \tag{4.8}$$

The dimensionless parameter

$$\delta = \frac{\pi\sigma_0 b R_f}{2\eta Q} \tag{4.9}$$

is a modified plasticity number, and quantifies the ratio between yield stress and viscous forces. Hereafter, we take δ as positive (since $Q > 0$) and refer to it as the yield stress parameter. We point out that, in Eq. (4.8) lengths and velocities were rescaled by R_f and $Q/(2\pi R_f)$ respectively, where R_f is the radius of the unperturbed interface at $t = t_f$. From this point on we use the dimensionless version of the equations. Our Eq. (4.8) is in agreement with the results of

Ref. [149] which studied the simpler situation involving the purely radial flow of a perfectly circular droplet.

Since we are interested in examining the interface destabilization process, we consider the regime where viscous forces prevail over the yield stress and flow is facilitated, which corresponds to $\delta \ll 1$. Therefore, we may neglect the third order term in δ shown in Eq. (4.8). Moreover, since (4.8) states that velocity is parallel to the pressure gradient, we may rewrite it in a more convenient way as

$$\nabla P = -\mathbf{v}\left[1 + \frac{\delta}{|\mathbf{v}|}\right]. \tag{4.10}$$

Equation (4.10) is an alternative form of Darcy's law ideally suited to describe the Hele-Shaw flow dynamics in the weak yield stress regime. The usual Newtonian Darcy's law is recovered when we set $\delta = 0$. This equation was used in [42] to investigate the interfacial instabilities that take place when a Newtonian fluid redially displaces a yield stress fluid. We address the reader to this reference in order contemplate the different morphological features exhibited by the model for this particular case.

We close this section by calling the reader's attention to an important distinction between our current results and the ones obtained in Ref. [140]. Kondic *et al.* [140] studied a nonNewtonian model where shear-thinning fluids were analyzed. In their work, a theoretical model for a shear rate dependent viscosity results in generalized Darcy's law [their Eq. (2)], which is distinct from our Darcy's law [Eq. (4.10)] for yield stress fluids. It should be emphasized that we do not propose a shear-thinning model, i. e., a shear dependent viscosity to a nonNewtonian fluid. Rather, we seek for a Darcy's law to a yield stress fluid, a nonNewtonian fluid that can support shear stresses without flowing, and derive a specific modified Darcy's law [our Eq. (4.10)] to describe flow of such a fluid in the confined geometry of a Hele-Shaw cell. Moreover, contrary to what is done in Ref. [140], our approach considers a Bingham model [Eq. (4.3)] where η denotes a Newtonian (constant) viscosity.

CHAPTER 5

Phase-field approach

Diffuse interface methods have become popular tools for physical modeling of multiphase systems with and without flow. Among them, the phase-field method has emerged as a widely used technique to numerically simulate complex interfacial pattern formation processes. Diffuse interface models are built on the notion that the interface between the phases is not a sharp boundary, but has a finite width and is characterized by rapid but smooth transitions in the density, viscosity and other physical quantities. In phase-field models, a non-conserved order parameter, the phase field θ, is introduced to describe the phase transition. It has constant values in the bulk phases (e.g., in this work, $\theta = +1$ in one bulk phase and $\theta = -1$ in the other) and varies smoothly across the diffuse interface region ($-1 < \theta < +1$) in a hyperbolic tangent or similar fashion. The propagation equation for the phase field (i.e., the phase-field equation) and the relevant conservation equations are derived from thermodynamically consistent theories of continuum phase transitions that account for the gradient energy across the diffuse interface. The most appealing feature of the phase-field method is that all governing equations can be solved over the entire computational domain without any a priori knowledge of the location of the interfaces. Interface tracking is completely avoided and topology changes are handled naturally without the need for any special procedures. Even though interface curvature and normal direction are not explicitly evaluated, the phase-field method is especially well suited for problems in which the interface motion depends on gradients of an external field normal to the interface and on the local curvature of the interface.

This method introduces a mesoscale ε, which is not present in the original macroscopic equations and determines a finite thickness to the interface. By consistency, this parameter must be the smallest length scale of the problem. The equations are then chosen in such a way that the original bulk equations (or sharp interface equations) and boundary conditions are recovered in the $\varepsilon \to 0$ limit. Therefore, the phase-field equations for a given model are not

intended to describe the true mesoscale physics of the system, and are then not unique.

In a general point of view, we may reproduce a static interface between two fluid phases confined in two dimensions by relaxing the phase-field θ as

$$\varepsilon^2 \partial_t \theta = f(\theta) + \varepsilon^2 \nabla^2 \theta, \tag{5.1}$$

where $f(\theta)$ is a function chosen to reproduce the desired θ values at the distinct fluid phases. We take $f(\theta) \equiv \theta(1-\theta^2)$ in order to reproduce the bulk phases as the values $\theta = \pm 1$. Then, Eq. (5.1) becomes a Ginzburg-Landau equation for a nonconserved order parameter θ. The θ field in this model is known to diffuse towards a kink solution of a certain width in a short time scale.

Lets for instance set as initial condition to the phase-field the following step function: $\theta = +1$ for the inner phase $\rho > 0$, and $\theta = -1$ for the outer phase $\rho < 0$, where ρ is the normal distance to the arbitrary initial interface and it is positive inwards. After relaxing this initial condition using Eq. (5.1), we obtain as the leading order solution [43, 153] $\theta \approx \tanh[\rho/(\varepsilon\sqrt{2})]$. Notice that this solution indicates that $\nabla\theta$ points at the normal direction to the interface at the diffuse region between the phases. Moreover, the interface can be tracked by taking the curve $\theta = 0$ and its introduced thickness is of the order of ε (in fact, if we define the diffuse interface as $-0.9 < \theta < 0.9$, its width is given by $-1.5\,\varepsilon\sqrt{2} < \rho < 1.5\,\varepsilon\sqrt{2}$). However, this kink profile keeps evolving towards the minimization of the length of the effective interface with normal velocity proportional to the local curvature (i.e., according to Allen-Cahn law [43]). This issue leads the interface to a curvature flow, causing the loss of phase (i. e., loss of fluid mass), and will be further discussed in the following section.

5.1 Viscous fingering in usual Newtonian fluids

A consistent phase-field model suitably developed to reproduce the viscous fingering dynamics of usual Newtonian fluids was originally proposed by Ref. [43]. In their work, they introduce an additional term in Eq. (5.1) in order to cancel out the local Allen-Cahn dynamics

of the interface, and maintain the hyperbolic tangent profile while the interface moves. This solves the problem of mass conservation at each phase and imposes a correct normal velocity at the boundary in between them. In this section we will briefly comment some important aspects of this model, so later on we may use it as a reference for viscous fingering in complex fluids.

First of all, we must set the original dynamical equations and boundary conditions at the sharp interface H-S problem, and only then find out their proper phase-field equations. The original sharp interface equations for the flow of two immiscible viscous fluids in a Hele-Shaw cell may be written in terms of a stream function, i. e., the harmonic conjugate of the velocity potential. Since the fluids are taken to be incompressible, $\nabla \cdot \mathbf{v} = 0$ holds at the bulk of each fluid and we may define the scalar stream function ψ for each fluid as $\mathbf{v} = \nabla \times (\psi\ \mathbf{z})$, where $\mathbf{z}$ is the unitary vector at the direction perpendicular to the H-S plates. The fact that the stream function is continuous at the interface makes the use of this variable particularly convenient. The Hele-Shaw equations in stream function formulation can be written as

$$\nabla^2 \psi = -\Gamma\ \delta(\rho), \tag{5.2}$$

where Γ represents the vortex-sheet strength between the fluids, $\delta(\rho)$ is the Dirac δ distribution and ρ is the normal distance to the interface. The parameter Γ is evaluated at the interface as the discontinuity of the tangential components of the outer ($\mathbf{v}_2$) and inner ($\mathbf{v}_1$) fluid velocities, i. e., $\Gamma = (\mathbf{v}_2 - \mathbf{v}_1) \cdot \mathbf{s}$ at the interface, where $\mathbf{s}$ denotes the unitary vector tangential to the interface. As a matter of fact, the proper boundary conditions to the velocity field across the interface, Eqs. (1.3) and (1.4), are already taken into account in Eq. (5.2). Moreover, by utilizing Darcy's law [Eq. (1.2)] we may rewrite the vortex-sheet in terms of the stream function [43]

$$\Gamma = \gamma + A(\partial_n \psi_2 + \partial_n \psi_1), \tag{5.3}$$

where ∂_n is the derivative at the normal direction to the interface and $A = (\eta_1 - \eta_2)/(\eta_1 + \eta_2)$ is the viscosity contrast between the fluids. The γ term comes from the tangential pressure gradient difference at the interface and is determined by the pressure boundary condition [Eq. (1.5)].

At the absence of external forces we have

$$\gamma = 2\frac{\sigma b^2}{12(\eta_1+\eta_2)}\partial_s \kappa, \tag{5.4}$$

where σ is the surface tension, and $\partial_s \kappa$ is the derivative of the interface in-plane curvature along the tangential direction. If there were any discontinuities caused by external forces, such as centrifugal forces [9], they would also appear here in the γ expression.

Now we have set the sharp interface equations (5.2) and (5.3), we may write the phase-field relaxation equation for ψ as

$$\tilde{\varepsilon}\partial_t \psi = \nabla^2 \psi + A\nabla\cdot(\theta\nabla\psi) + \gamma\frac{(1-\theta^2)}{2\sqrt{2}\varepsilon}. \tag{5.5}$$

Here, the right hand side corresponds to the Poisson equation in (5.2) at the limit $\varepsilon \to 0$. The Dirac δ function peaked at the interface that appears multiplied by γ was substituted by a smooth phase-field functional peaked on $\theta = 0$, namely $(1-\theta^2)/(2\sqrt{2}\varepsilon)$. Moreover, the second term on the right hand side accounts for the normal derivatives that appear multiplied by A, since $\nabla\theta$ points at the normal direction to the interface. The time derivative $\partial_t\psi$ was added to introduce a rapid relaxation for ψ, so $\tilde{\varepsilon}$ is also a small artificial parameter that defines the characteristic diffusion time. This equation is in accordance to their original boundary conditions and the following generalized function

$$\gamma = 2\frac{\sigma b^2}{12(\eta_1+\eta_2)}\,\mathbf{s}\cdot\nabla\kappa. \tag{5.6}$$

Furthermore, the time evolving equation for the phase-field θ is given by

$$\varepsilon^2\partial_t\theta = f(\theta) + \varepsilon^2\nabla^2\theta + \varepsilon^2\kappa(\theta)|\nabla\theta| - \varepsilon^2\mathbf{V}\cdot\nabla\theta, \tag{5.7}$$

where

$$\mathbf{V} = \nabla\times(\psi\,\mathbf{z}) \tag{5.8}$$

is the phase-field advective velocity, and $f(\theta) = \theta(1-\theta^2)$. The generalized phase-field de-

pendent curvature is given by

$$\kappa(\theta) = -\nabla \cdot \mathbf{n}(\theta), \tag{5.9}$$

where

$$\mathbf{n}(\theta) = \frac{\nabla\theta}{|\nabla\theta|} \tag{5.10}$$

is the normal unitary vector, and the tangent vector is given by

$$\mathbf{s}(\theta) = \mathbf{n}(\theta) \times \mathbf{z}. \tag{5.11}$$

By comparing Eq. (5.1) with Eq. (5.7) we notice that two extra terms were added to the later. The term $\varepsilon^2\kappa(\theta)|\nabla\theta|$ was introduced to cancel off the Allen-Cahn law by killing the leading order contribution of the spurious curvature flow. Therefore, it makes the θ kink profile stable to any interface shape and keeps the mass balance between the phases. The last term on the right hand side of Eq. (5.7) simply sets the proper normal velocity to the interface according to the dynamics of ψ.

We stress that the phase-field equations (5.5) and (5.7) were carefully set in order to reproduce the original moving boundary problem at the sharp interface limit $\varepsilon,\tilde{\varepsilon} \to 0$. This was carried out in Ref. [43] by expanding the outer and inner phase equations in powers of ε and performing an asymptotic matching between them.

5.2 Viscous fingering in magnetic fluids

We turn now our attention to the viscous fingering problem when at least one of the fluids happens to be a magnetic fluid. Both fluids are assumed to be incompressible and obey a generalized Darcy's law that can be written as a potential flow, as in Eqs. (2.2) or (3.6). The sharp interface equations of this moving boundary problem may be set in terms of the velocity potential as shown in Eqs. (3.11), (3.12) and (3.13). We could also reformulate the problem in terms of its stream function ψ and it would look exactly like Eq. (5.2), but with a different expression for the vortex-sheet Γ. Therefore, there is no fundamental difference between the

equations set in Sec. 5.1 and those written for the flow of magnetic fluids, and we may use the phase-field equations (5.5) and (5.7) to describe both of them.

Lets take as a matter of simplification the case where fluid 1 is a Newtonian ferrofluid and fluid 2 is a nonmagnetic fluid. In this situation, the vortex-sheet strength is obtained by using (2.1) and (2.4) in $\Gamma = (\mathbf{v}_2 - \mathbf{v}_1)\cdot\mathbf{s}$ at the interface. Thus, it can be written as

$$\Gamma = \partial_n\psi_2 - \partial_n\psi_1 = \gamma + A(\partial_n\psi_2 + \partial_n\psi_1), \tag{5.12}$$

where γ is given by

$$\gamma = 2\frac{b^2}{12(\eta_1+\eta_2)}\,\mathbf{s}\cdot\nabla\left[\sigma\kappa - \frac{\mu_0\chi^2(\mathbf{H}\cdot\mathbf{n})^2}{2} - \frac{\mu_0\chi H^2}{2}\right]. \tag{5.13}$$

In (5.13) we have also assumed that the ferrofluid magnetization is collinear with the local magnetic field, i. e., $\mathbf{M} = \chi\mathbf{H}$. In case our magnetic fluid was a MR fluid, we would also have to include in (5.13) its magnetic field-dependent yield stress contribution, as in Eq. (3.6).

The only missing part in our description now is how to determine the local magnetic field $\mathbf{H}$ at the ferrofluid domain, since this is a nonlocal problem that depends on the interface shape. For the case where the applied magnetic field $\mathbf{H_0}$ has already a natural gradient, as in Eqs. (3.1) and (3.24), we may consider the leading contribution to the field gradient as produced by the applied magnetic field itself, and use $\mathbf{H} \approx \mathbf{H_0}$ in (5.13).

5.2.1 Ferrofluid in a radial magnetic field

Inspired by Refs. [24, 40] we have performed preliminary numerical phase-field simulations of a ferrofluid confined in a H-S cell and subjected to an applied radial magnetic field. The setup is explained in Sec. 3.1 and can be visualized in Fig. 3.1, where the inner fluid is now a Newtonian ferrofluid and the outer fluid is a nonmagnetic fluid of negligible viscosity. The aim here was to simulate Eqs. (5.5) and (5.7), where (5.13) is calculated using $\mathbf{H} = \frac{H_0}{L} r\ \hat{\mathbf{r}}$. Moreover, we may rescale velocities by $\frac{\mu_0 H_0^2 b^3}{24(\eta_1+\eta_2)L^2}$ and lengths by b in order to rewrite (5.13)

in the dimensionless form

$$\gamma = 2\,\mathbf{s}\cdot\nabla[B\kappa - \chi^2(\mathbf{r}\cdot\mathbf{n})^2 - \chi r^2], \tag{5.14}$$

where $B = \frac{2\sigma L^2}{\mu_0 H_0^2 b^3}$ is the dimensionless surface tension. This problem can be seen as a variation of the centrifugally driven nonmagnetic viscous fingering [9] one, with an augmented version for pressure jump condition (2.4).

We have used a C based code to discretize our phase-field equations (5.5) and (5.7) using finite differences in a semi-implicit in time scheme. In this scenario, we employ first order forward in time and second order centered in space differences to approximate the expressions for the derivatives. For each time step the diffusive and advective terms in Eqs. (5.5) and (5.7) are calculated implicitly. The remaining nonlinear terms are taken explicitly at the current time step. For more details of our numerical approach see Sec.5.3.2.2.

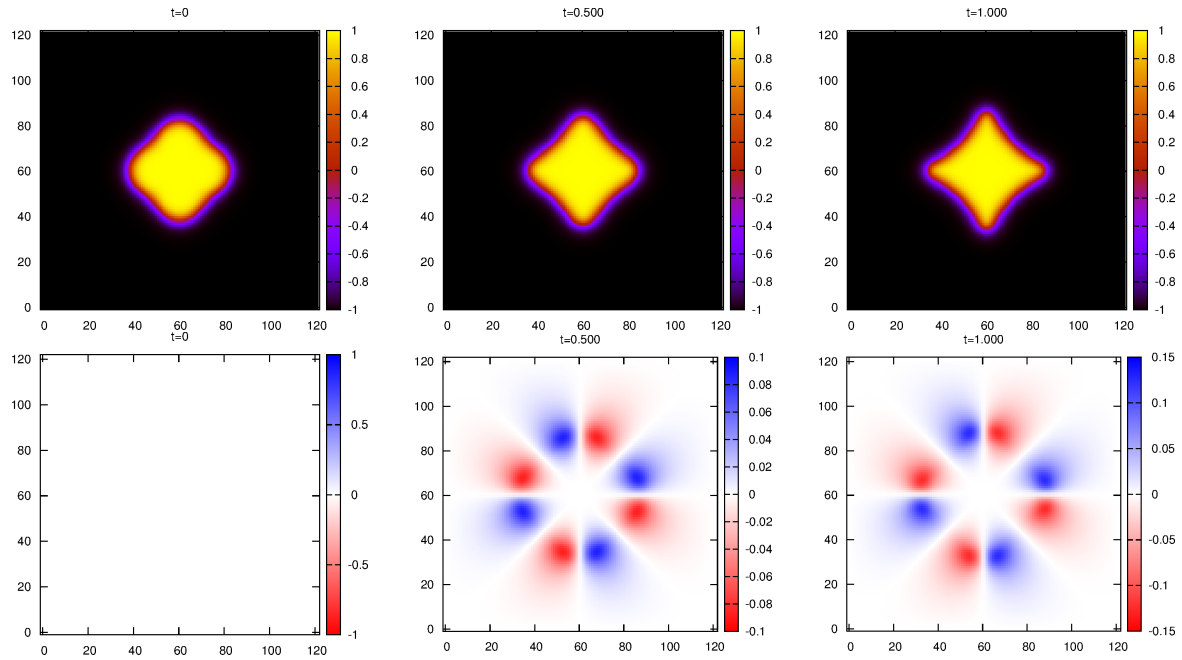

Figure 5.1: Phase-field simulation of an initially perturbed ferrofluid droplet subjected to a radial magnetic field. Upper panels: phase-field plots in color scale for three different times, where $\theta = +1$ ($\theta = -1$) corresponds to the inner (outer) fluid phase. Lower panels: stream function plots for the correspondent times in the upper plots.

Figure 5.1 shows snapshots from the simulation of Eqs. (5.5) and (5.7) for an initially circular droplet perturbed by a 4-fold mode. The upper panels display the phase-field θ at three different times: $t = 0$, $t = 0.500$ and $t = 1.000$, where the $\theta = +1$ phase (yellow colored) corresponds to the ferrofluid and the $\theta = -1$ phase (black colored) correspond to the nonmagnetic fluid. The lower panels display the stream function ψ at the three respective values of t. We have used the following values for the numerical parameters: $\varepsilon = 0.1$, $\tilde{\varepsilon} = 0.01$, time step $dt = 0.005$, a grid of size 120x120 and square mesh $dx = dy = 0.05$. The relevant dimensionless physical parameters are the viscosity contrast $A = 0.95$, the dimensionless surface tension $B = 0.01$, and the magnetic susceptibility $\chi = 0.5$.

The initial condition for θ is set as $\theta = \tanh[(R + a\cos 4\varphi - r)/(\varepsilon\sqrt{2})]$, where (r, φ) are polar coordinates, the initial circular radius is $R = 1.0$ and the perturbation amplitude of the fourth harmonic mode is $a = 0.2$. The stream function is set as $\psi = 0.0$ at $t = 0.0$. Boundary conditions at the walls are chosen to be $\theta = -1.0$ and $\psi = 0.0$, and correspond to zero normal velocity for the outer fluid phase at the borders.

As we can see from Fig. 5.1, an initial perturbation of the mode $n = 4$ tend to increase in amplitude for early times and then saturate, making the finger tips to get sharper and sharper. This is in accordance with the linear prediction at (3.16) and also with the morphological features of fully nonlinear stationary patterns in [24]. We believe that the presence of the normal magnetization contribution at the pressure jump condition (2.4) is the main responsible for the ultimate pattern morphology in $t = 1.000$, since this is the only difference between the centrifugally driven viscous fingering and our case. In the absence of this particular contribution (by taking out the term proportional to χ^2 in (5.14)) we would recover the centrifugally driven result in which finger tend to grow and get broader, up to the point that pinching happens [9].

If we continue to run the simulation for later times, we notice a significative loss of mass of the inner phase. This may be occurring due to the high curvature values the finger tips tend to exhibit, leading the curvature radius to be of the order of ε, which would violate the phase field assumption that ε is the smallest length scale in the problem. More numerical development still must be done in order to correct such issues.

5.3 Actin-based motility of lamellar fragments

Lamellar fragments are pieces of lamellipodia, the actin-based locomotion machinery of crawling cells. These fragments have been shown to exhibit spontaneous, sustained motion if properly deformed [35]. Despite its relative simplicity, a theoretical understanding of the minimal ingredients to explain this phenomenon is still lacking. A challenging question is how the treadmilling dynamics of actin, which polymerizes at the boundary, is coupled to the shape of the fragment to sustain motion, in particular in the absence of molecular motors. Recently, it has been shown that in an appropriate approximation, the flow of actin satisfies Darcy's law in an effectively two-dimensional geometry [36], thus reducing the dynamics to a free-boundary problem similar to that of viscous-fingering in Hele-Shaw cells, but with different boundary conditions [43].

Here we present a phase-field description of this free-boundary problem, as a tool to numerically integrate the fully nonlinear dynamics of this problem, aiming at a systematic study of the different families of steady propagating solutions, their stability and their basins of attraction. Such a diffuse-interface method is known to have important advantages with respect to sharp-interface methods (boundary-integral methods or conformal mapping techniques) in Laplacian problems, in particular when interfaces adopt complex shapes. Most importantly, their advantage is most substantial when the viscosity of the displaced fluid is not neglected, a common approximation that may have to be relaxed in order to gain a more quantitative understanding of the problem and its biological relevance. The main goal in this study is to complement with fully nonlinear numerical simulations the weakly nonlinear analysis done by using conformal mapping techniches in Ref. [154].

A phase-field strategy has already been used before within more complicated models [155, 156]. The model we present concentrates on the effects of polymerization forces combined with friction on the substrate and with membrane tension. The absence of molecular motors in the description makes the model simpler and more amenable to theoretical discussion. Appropriate convergence tests have been performed showing that the model is quantitatively accurate and competitive with respect to other techniques. Our results in the fully nonlinear regime confirm

that actin polymerization alone can sustain motion, and provide not only the families of stable steady shapes, but also a first characterization of their relative basins of attraction.

5.3.1 Problem formulation: sharp interface equations

Consider an initially nearly circular actin-based lamellar fragment surrounded by a non-active viscous fluid. The flow of both fluids takes place at an effectively two-dimensional geometry similar to a Hele-Shaw cell. Within this framework, the lubrication approximation is valid and inertial terms are negligible. The effective viscosities (or flow permeability) of the fluids are denoted as μ_j, where $j = 1$ ($j = 2$) labels the inner (outer) fluid. Also, the fluids in consideration are immiscible, and there exists a surface tension σ between them. In addition, gravity effects happen to be along the transversal direction $\mathbf{z}$ which is neglected.

In this confined environment the flow is governed by Darcy's law [37]

$$\mu_j \mathbf{v}_j = -\nabla \mathbf{p_j}, \tag{5.15}$$

where p_j denotes the pressure.

The inner lamellar fluid (fluid 1) is consumed due to actin depolymerization, which is modeled into constant areal negative divergence $-k$, while the outer fluid (fluid 2) is incompressible

$$\nabla \cdot \mathbf{v}_1 = -k, \tag{5.16}$$

$$\nabla \cdot \mathbf{v}_2 = 0. \tag{5.17}$$

Moreover, we assume that actin polymerization takes place at the interfacial boundary. Therefore, fluid 1 is produced at constant velocity rate v_p along the normal direction of the interface. This assumption is specified by the following modified boundary condition

$$(\mathbf{v}_2 - \mathbf{v}_1) \cdot \mathbf{n} = -v_p, \tag{5.18}$$

where $\mathbf{n}$ is the unitary normal vector to the interface and points inwards. It is worth noting that usual continuity of the velocities' normal component is recovered by setting the polymerization velocity term v_p to zero.

The problem is completely stated in terms of the velocity fields by deriving a boundary condition for the tangential jump of velocities. This is done by using Eq. (5.15) plus the pressure jump condition due to surface tension $p_1 - p_2 = \sigma\kappa$, where κ denotes the in-plane interfacial curvature. Following this prescription we derive

$$(\mathbf{v}_2 - \mathbf{v}_1)\cdot\mathbf{s} = \frac{2\sigma}{\mu_1+\mu_2}\partial_s\kappa + A(\mathbf{v}_2+\mathbf{v}_1)\cdot\mathbf{s}, \tag{5.19}$$

where $\mathbf{s}$ is the unitary tangential vector pointing counterclockwise, and $A = (\mu_1-\mu_2)/(\mu_1+\mu_2)$ represents the viscosity contrast.

Equations (5.16)-(5.19) defines the moving boundary problem of our system in which the normal interface velocity is given by $V_n = \mathbf{v}_1\cdot\mathbf{n} - v_p = \mathbf{v}_2\cdot\mathbf{n}$.

It is useful to perform a change of variables in order to reformulate the original problem in terms of tangentially continuous stream functions. To accomplish this goal we must redefine a velocity field for the inner region such that Eq. (5.16) becomes divergence-free. Moreover, aiming to obtain normal continuity condition at Eq. (5.18), the outer velocity field will also be redefined. Therefore we introduce the following corresponding stream functions

$$\nabla\times(\psi_1\mathbf{z}) = \mathbf{v}_1 + \frac{k}{2}\mathbf{r}, \tag{5.20}$$

$$\nabla\times(\psi_2\mathbf{z}) = \mathbf{v}_2 + \nabla\phi, \tag{5.21}$$

where $\mathbf{z} = \mathbf{s}\times\mathbf{n}$ is the unitary transversal vector and $\mathbf{r}$ is the two-dimensional position vector. The scalar field ϕ is defined at the outer region and it is determined by taking the divergence of Eq. (5.21) and imposing continuity of the tangential components of ψ_j at the interface. Therefore

$$\nabla^2\phi = 0, \tag{5.22}$$

$$\partial_n\phi = v_p + \frac{k}{2}\mathbf{r}\cdot\mathbf{n} \equiv \alpha, \tag{5.23}$$

determine ϕ at the outer region.

Furthermore, taking the curl of Eqs. (5.20) and (5.21) leads to

$$\nabla^2 \psi_{1,2} = 0. \tag{5.24}$$

Also, one may rewrite the boundary conditions (5.18) and (5.19) at the following forms

$$\partial_s \psi_1 = \partial_s \psi_2, \tag{5.25}$$

$$\partial_n \psi_2 - \partial_n \psi_1 = \gamma + A(\partial_n \psi_2 + \partial_n \psi_1), \tag{5.26}$$

where

$$\frac{\gamma}{2} = B\partial_s \kappa + \frac{(1-A)}{2}\partial_s \phi - \frac{(1+A)}{2}\frac{k}{2}\mathbf{r}\cdot\mathbf{s}, \tag{5.27}$$

and

$$B = \frac{\sigma}{\mu_1 + \mu_2}. \tag{5.28}$$

Equations (5.24)-(5.26) completely define the moving boundary problem in terms of the inner and outer stream functions, ψ_1 and ψ_2 respectively, and they resemble Eq. (5.2). The normal interface velocity is now expressed in terms of these new fields as $V_n = \partial_s \psi_1 - (k/2)\,(\mathbf{r}\cdot\mathbf{n}) - v_p = \partial_s \psi_2 - \partial_n \phi$.

5.3.2 Phase-field equations

In order to numerically obtain the fully nonlinear dynamics of the moving boundary problem described in the last section, it is convenient to use an analogous phase-field method to that described by Eqs. (5.5) and (5.7). We will use the auxiliary function θ, that reproduces a diffuse-interface of thickness ε, to rewrite the equations for ψ and ϕ.

Apart from the physical control parameters A, B, k and v_p, the dynamics in this model also depends on the artificial interface thickness ε, a relaxation time $\tilde{\varepsilon}$ for the stream function ψ, and a relaxation time ε' for the potential ϕ, which may be taken in general as different for numerical convenience. In the limit $\varepsilon,\tilde{\varepsilon},\varepsilon' \to 0$ the dynamics is strictly that of Eqs. (5.24)-(5.26).

We are able to write phase-field equations corresponding to Eqs. (5.22) and (5.24) as

$$\varepsilon' \partial_t \phi = \nabla^2 \phi + \alpha(\theta) \frac{(1-\theta^2)}{2\sqrt{2}\varepsilon}, \tag{5.29}$$

$$\tilde{\varepsilon} \partial_t \psi = \nabla^2 \psi + A \nabla \cdot (\theta \nabla \psi) + \gamma(\theta, \phi) \frac{(1-\theta^2)}{2\sqrt{2}\varepsilon}, \tag{5.30}$$

respectively. These equations are in accordance to their original boundary conditions and the following generalized functions

$$\alpha(\theta) = v_p + \frac{k}{2} \mathbf{r} \cdot \mathbf{n}(\theta), \tag{5.31}$$

$$\frac{\gamma(\theta)}{2} = \mathbf{s}(\theta) \cdot \left[B \nabla \kappa(\theta) + \frac{(1-A)}{2} \nabla \phi - \frac{(1+A)}{2} \frac{k}{2} \mathbf{r} \right]. \tag{5.32}$$

The time evolving equation for the phase-field θ is given by

$$\varepsilon^2 \partial_t \theta = f(\theta) + \varepsilon^2 \nabla^2 \theta + \varepsilon^2 \kappa(\theta) |\nabla \theta| - \varepsilon^2 \mathbf{V} \cdot \nabla \theta, \tag{5.33}$$

where

$$\mathbf{V} = \nabla \times (\psi \, \mathbf{z}) - \frac{k}{2} \mathbf{r} - v_p \mathbf{n}(\theta) \tag{5.34}$$

is the phase-field advective velocity, and $f(\theta) \equiv \theta(1-\theta^2)$. The generalized phase-field dependent curvature is given by

$$\kappa(\theta) = -\nabla \cdot \mathbf{n}(\theta), \tag{5.35}$$

where

$$\mathbf{n}(\theta) = \frac{\nabla \theta}{|\nabla \theta|} \tag{5.36}$$

is the normal unitary vector, and the tangent vector is given by

$$\mathbf{s}(\theta) = \mathbf{n}(\theta) \times \mathbf{z}. \tag{5.37}$$

We have arbitrarily chosen the $+1$ (-1) phase as the inner (outer) one. Accordingly to this convention, the normal vector (5.36) points inwards, the tangent vector (5.37) points at the counterclockwise direction, and the curvature (5.35) is positive for a circle.

5.3.2.1 Dimensionless parameters

Now, we write down the dimensionless versions of our equations. Lengths and velocities are rescaled by $R_0 = 2v_p/k$, and v_p, respectively. Equations (5.29), (5.30) and (5.33) hold their original form. On the other hand, Eqs. (5.31), (5.32) and (5.34) are rewritten as

$$\alpha(\theta) = 1 + \mathbf{r}\cdot\mathbf{n}(\theta), \tag{5.38}$$

$$\frac{\gamma(\theta)}{2} = \mathbf{s}(\theta)\cdot\left[\tilde{B}\nabla\kappa(\theta) + \frac{(1-A)}{2}\nabla\phi - \frac{(1+A)}{2}\mathbf{r}\right], \tag{5.39}$$

$$\mathbf{V} = \nabla\times(\psi\,\mathbf{z}) - \mathbf{r} - \mathbf{n}(\theta), \tag{5.40}$$

respectively, and

$$\tilde{B} = \frac{\sigma k^2}{4(\mu_1+\mu_2)v_p^3}. \tag{5.41}$$

5.3.2.2 Numerical implementation

We follow [9, 153, 157] and use finite differences in a semi-implicit in time scheme to discretize our dimensionless phase-field equations (5.29), (5.30) and (5.33). In this scenario, we employ first order forward in time and second order centered in space differences to approximate the expressions for the derivatives

$$\partial_t\theta \approx \frac{\theta_{i,j}^{n+1} - \theta_{i,j}^{n}}{dt}, \tag{5.42}$$

$$\partial_x\theta \approx \frac{\theta_{i+1,j} - \theta_{i-1,j}}{2dx}, \tag{5.43}$$

$$\partial_{xx}\theta \approx \frac{\theta_{i+1,j} - 2\theta_{i,j} + \theta_{i-1,j}}{dx^2}, \tag{5.44}$$

where i (j) stands for x (y) discretization, n for time discretization, dx is the mesh size and dt is the time step. For each time step the diffusive and advective terms in Eqs.(5.29), (5.30) and (5.33) are calculated implicitly, i. e., they are taken at time step $n+1$. The remaining nonlinear terms are taken explicitly at time step n. For instance, the curvature $\kappa(\theta)$ is calculated explicitly as in [153, 157]

$$\kappa = -\frac{\partial_{xx}\theta + \partial_{yy}\theta}{[(\partial_x\theta)^2 + (\partial_y\theta)^2 + \delta]^{1/2}} + \frac{(\partial_x\theta)^2\partial_{xx}\theta + 2\partial_x\theta\partial_y\theta\partial_{xy}\theta + (\partial_y\theta)^2\partial_{yy}\theta}{[(\partial_x\theta)^2 + (\partial_y\theta)^2 + \delta]^{3/2}}, \tag{5.45}$$

where δ is a small numerical factor of the order 10^{-8} introduced to avoid divergences. The derivatives of κ in Eq. (5.39) are calculated using second order centered differences such as $\partial_x\kappa \approx \frac{\kappa_{i+1,j} - \kappa_{i-1,j}}{2dx}$.

At each time iteration, we first calculate ϕ^{n+1} by using θ^n in (5.29), then obtain ψ^{n+1} by using ϕ^{n+1} and θ^n in (5.30), and finally we obtain θ^{n+1} by using ψ^{n+1} in (5.33). For each of these sub steps, the implicit terms are calculated by inverting a $(2N+1)$x$(2N+1)$ sparse matrix obtained for the extended system composed by all the field values of the grid, including the boundary values.

Figure 5.2 shows snapshots of the time evolution for an initially circular droplet perturbed by Fourier modes $n = 1$ and $n = 2$ of respective amplitudes a_1 and a_2. The upper panels display the phase-field θ at three different times: $t = 0$, $t = 38.5$ and $t = 87.0$, where the $\theta = +1$ phase (yellow colored) correspond to the cell fragment and the $\theta = -1$ phase (black colored) correspond to an usual viscous fluid. The mid panels display the stream function ψ at the three respective values of t. The lower panels display the auxiliary function ϕ at the three respective values of t. We have used the following values for numerical parameter: $\varepsilon = 0.1$, $\tilde{\varepsilon} = 0.01$, $\varepsilon' = 0.01$, time step $dt = 0.005$, a grid of size 150x150 and square mesh $dx = dy = 0.05$. The relevant dimensionless physical parameters are the viscosity contrast $A = 0.95$, the dimensionless surface tension $B = 0.08$, the polymerization velocity $v_p = 0.5$ and depolymerization rate $k = 1.0$.

The initial condition for θ is set as $\theta = \tanh[(R + a_1\cos\varphi + a_2\cos 2\varphi - r)/(\varepsilon\sqrt{2})]$, where

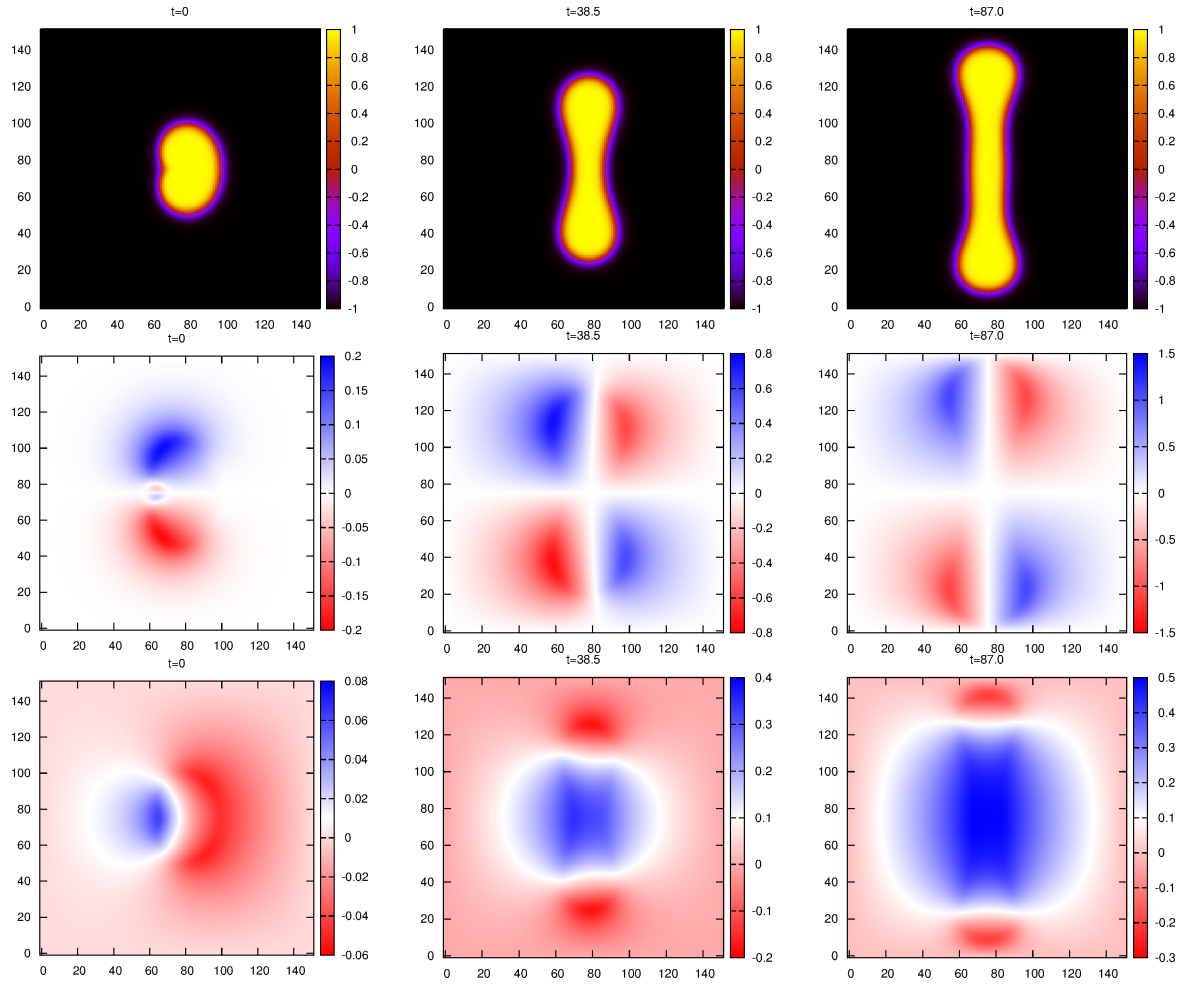

Figure 5.2: Phase-field simulation of an initially perturbed cell fragment. Upper panels: phase-field plots in color scale for three different times, where $\theta = +1$ ($\theta = -1$) corresponds to the inner (outer) fluid phase. Mid panels: stream function plots for the correspondent times in the upper plots. Lower panels: auxiliary ϕ function plots for the correspondent times in the upper plots. Boundary conditions are set as $\theta = -1.0$, $\psi = 0.0$ and $\phi = 0.0$.

(r, φ) are polar coordinates, the initial circular radius is $R = 1.0$ and the perturbation amplitudes are $a_1 = 0.3$ and $a_2 = 0.2$. Here, the mode $n = 1$ is added to the dynamics in order to brake the symmetry of the problem and introduce a propagating direction. Moreover, the auxiliary function is set as $\phi = 0.0$ and them relaxed by (5.29) until it saturates for the fixed initial θ, defining thus the initial condition for ϕ displayed at the $t = 0.0$ lower panel. The same procedure is done to find the initial condition for ψ displayed at the $t = 0.0$ mid panel: it was relaxed from $\psi = 0.0$ by using 5.30 keeping θ and ϕ fixed. This is done to guarantee that all the fields satisfy the same conditions at $t = 0$. Boundary conditions at the walls are chosen to be $\theta = -1.0$, $\psi = 0.0$ and $\psi = 0.0$. They correspond to zero normal velocity for the outer fluid phase at the borders, and also reflected mass sources at the boundaries produced by image charges of ϕ.

As we can see from Fig. 5.2, the initial perturbation of the mode $n = 2$ tend to increase in amplitude for early times, which is in agreement with the linear prediction in [36], and then saturate at very late times due to nonlinear and also boundary effects. The linear analysis also predicts that the mode $n = 1$, which is responsible for translations of the droplet mass center, is marginally stable and therefore could be enhanced by a nonlinear coupling. However, this is not the case in our simulation, since the shape becomes more symmetric with respect to both x and y axes as time grows, revealing a decrease in a_1.

This is not consistent with the conformal mapping results to this problem exposed in [154]. We should expect the droplet to saturate in a much more asymmetric shape, which would induce the shape to achieve much larger propagating velocities. Also, it was expected a much less prominent mode $n = 2$, that should not reach the boundaries. These evidences suggest that the constant valued boundary conditions $\psi = 0$ and $\phi = 0$ are introducing spurious effects and significantly changing the rising viscous fingering shapes.

In order to clarify this issue we have performed a simulation with the same parameters of Fig. 5.2, but this time using periodic boundary conditions for θ, ψ and ϕ. However, since the periodic boundary conditions are difficult to implement at our semi-implicit code, for this situation we have only used an explicit time integration scheme. This result is shown in Fig. 5.3.

Now in Fig. 5.3, the phase-field time evolution seems to be more coherent to the conformal

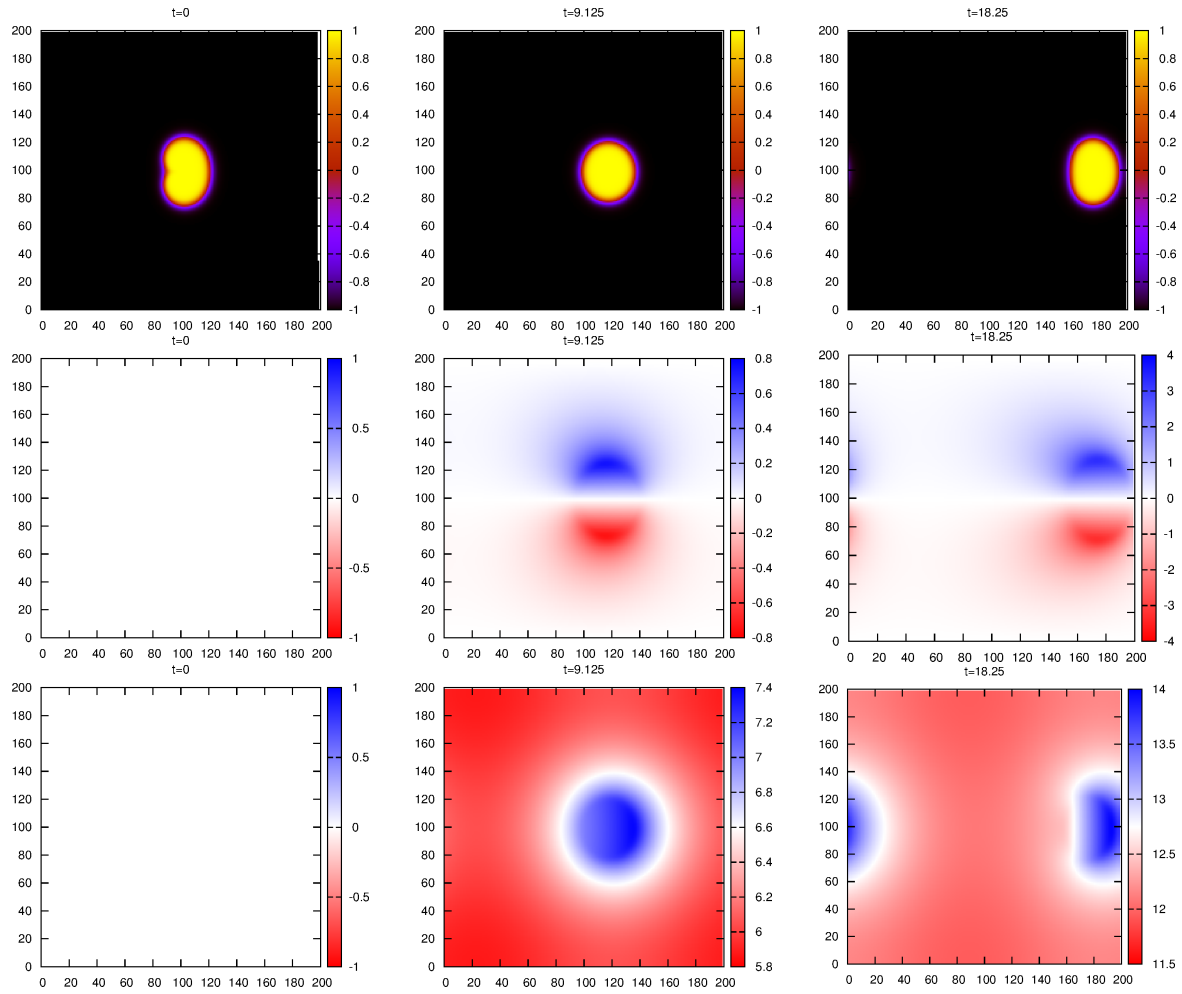

Figure 5.3: Phase-field simulation of an initially perturbed cell fragment. Upper panels: phase-field plots in color scale for three different times, where $\theta = +1$ ($\theta = -1$) corresponds to the inner (outer) fluid phase. Mid panels: stream function plots for the correspondent times in the upper plots. Lower panels: auxiliary ϕ function plots for the correspondent times in the upper plots. Boundary conditions are taken to be periodic for θ, ψ and ϕ.

mapping weakly nonlinear predictions. The droplet is much less elongated and pretty more asymmetric, as we can see in the snapshots of $t = 18.25$. Moreover, the propagating velocity is almost three orders of magnitude larger than in Fig. 5.2, being even larger than the velocities found in [154]. On the other hand, as the droplet touches the boundary walls we have to stop the simulation, since the centrifugal term in (5.39) is not well defined across the boundaries.

Although we have found travelling shapes in our phase-field model, more research is needed in order to get more quantitative and conclusive results about this specific topic. Other kinds of boundary conditions must be taken and a direct comparison with the weakly nonlinear shapes in [154] is still lacking.

CHAPTER 6

Conclusions

6.1 Conclusions from Chapter 2

In Chap. 2, we have performed a weakly nonlinear analysis of the ferrofluid peak formation problem in confined geometry. Our theoretical approach was able to extract useful analytical information about the morphology of the time-evolving interfacial patterns, as well as the stability of resulting steady structures. This is done at lowest nonlinear order through a perturbative mode coupling approach. The formation of the stationary or propagating peaks can be qualitatively explained by a mechanism involving the interplay of just two Fourier modes (the fundamental and its harmonic), and predicted already at second-order.

In Sec. 2.1, we have considered the normal field instability of a confined ferrofluid in the presence of a vertical magnetic field. Our analytical results for the nonlinear interface peaked morphology, dynamics and statics are in line with the experimental findings of Refs. [58, 59], and also with related steady shapes calculated in [52] through a much more convoluted theoretical approach.

We note that the fully nonlinear description of this problem through numerical simulations would be of great interest, but has not yet been analyzed. Despite its challenging nature (in part due to the sharpness of advanced time shapes), such a numerical study using the phase-field technique could be considered as a natural extension of our current analytic investigation.

In Sec. 2.2, we investigate the examined the influence of an in-plane tilted magnetic field on the profile shape and propagation velocity of interfacial traveling waves between a ferrofluid and a nonmagnetic viscous fluid. For a more general consideration, both fluids are subjected to a basal parallel flow. We performed a weakly nonlinear analysis of the system (similar to that of Sec. 2.1) that provided important analytic information about the dynamics of the propagating

structures.

The action of the tilted magnetic field is revealed already at the linear regime: it is shown that by tilting the field one can sustain wave motion even in the absence of external flow. Moreover, it is found that the velocity of the waves depends on the tilting angle. Our nonlinear results indicate that the time evolving interfacial wave shapes tend to approach stationary wave profiles. In fact, the shape of such stationary wavy patterns can be manipulated by the tilted magnetic field, resulting in different nonlinear wave forms: sinusoidal, vertical peaked structures separated by wide troughs, and skewed undulating forms. Finally, we found that the the nonlinear wave velocity is sensitive to variations on the tilting angle, a mechanism that can be used to control its magnitude.

It would be of interest to see our theoretical results verified by laboratory experiments. However, we are not aware of any existing parallel flow experiment with a ferrofluid subject to a tilted uniform magnetic field. Interestingly, there is a recent example in the literature in which a theoretical prediction [158] about solitary wave propagation in ferrofluids has been realized experimentally [159]. However, it considered the action of an azimuthal magnetic field on a cylindrical ferrofluid surface. In the same spirit, we hope our current results could pave the way for future experimental and theoretical investigations into propagating deformations, and localized waves in Hele-Shaw parallel flow with ferrofluids.

6.2 Conclusions from Chapter 3

The study of Hele-Shaw pattern formation in ferrofluids has been largely explored during the last few decades. These investigations have unveiled a number of patterning structures and interesting dynamic behaviors. However, the same cannot be said about similar studies for confined magnetorheological fluids. In this chapter we have examined the emergence of patterns in a complex magnetic fluid, in which its yield stress properties can be tuned by an external radial magnetic field.

At Sec. 3.1, we have explored the problem of a MR fluid subjected to a radialy increasing

external magnetic field. By using linear analysis, mode-coupling theory, and a vortex-sheet formalism we have been able to identify several features about the stability and morphology of the confined MR fluid patterns. At linear stages of the dynamics, we have found that the yield stress contributions tend to stabilize the interface, restraining the number of fingering structures formed. At the weakly nonlinear level, the yield stress acts to inhibit the formation of highly spiky fingers induced by the applied field. Finally, by assuming a stationary condition we have accessed fully nonlinear shapes, which look like swollen polygons, whose edges undergo a morphological transition by varying from convex to concave structures. Despite their unstable character, this class of exact solutions shed some light on the understanding of some important fully nonlinear aspects of this complex pattern forming system.

In Sec. 3.2, we have investigated exact stationary solutions associated to centrifugally-driven magnetic fluid patterns subjected to an azimuthal magnetic field in the confined geometry of a Hele-Shaw cell. By considering the response of Newtonian ferrofluids and yield stress, magnetorheological fluids, a vortex-sheet formalism has been employed to unveil a variety of fully nonlinear steady shapes.

We applied a perturbative, second-order mode-coupling theory to access important static and dynamic aspects of the pattern forming system. Our analytical predictions for stationary solutions at lowest nonlinear order, and including just a few participating modes are compared to the exact solutions of the problem, and a satisfactory agreement is found. This supports the idea that the weakly nonlinear approximation provides a good reduced description of the exact solutions. The weakly nonlinear approach is also used to examine the stability of the equilibrium pattern morphologies. In spite of the stabilizing action of both applied azimuthal magnetic field and yield stress properties, we have verified that the steady solutions are unstable. Nevertheless, they can help one to understand important morphological features of corresponding fully nonlinear time evolving patterns.

6.3 Conclusions from Chapter 4

In this chapter, we have considered a modified version of the Saffman-Taylor viscous fingering problem in radial Hele-Shaw geometry. In contrast to the conventional purely Newtonian situation, we have examined the case in which a fluid of negligible viscosity displaces a viscous yield stress fluid. Motivated by existing experiments [34, 147] we have focused on the regime in which viscous effects prevail over yield stress. These experiments revealed the rising of ramified structures, presenting some tip-splitting events, but the predominance of side branching phenomena.

In order to get some useful analytical hints about the influence of the yielding direction on viscous fingering, we have deduced a Darcy-like law [Eq. (4.10)] for the gap-averaged problem, considering that the yield stress acts parallel to the velocity direction. This expression was used in Ref. [42] as a starting point to study the onset of pattern formation of confined yield stress fluids in the weak yield stress regime. As a result, Eq. (4.10) revealed itself to be capable of reproducing important morphological features observed in experiments, such as side-branching at the finger tips.

6.4 Conclusions from Chapter 5

We have developed a phase-field model strongly based on the one proposed by Ref. [43] in order to simulate viscous fingering in some kind of complex fluids, namely magnetic fluids (Sec. 5.2) and lamellar fragments (Sec. 5.3). The model consists on introducing an auxiliary function that mimics the flow of two immiscible fluid phases by introducing a diffuse interface between them. As a consequence of that, the original moving boundary problem to the sharp interface is transformed into a set of partial differential equations for the relevant fields and may be numerically integrated continuously across the smoothed interface.

Preliminary numerical results are in reasonable qualitative agreement with previous simulations and analytical predictions. On the other hand, the code still requires computational

improvement in order to solve some issues due to high curved interfaces for magnetic fluids, and also to set more suitable boundary wall conditions for cell fragments.

As future perspectives we shall test the phase-field method to magnetic fluids under other kinds of applied magnetic field configurations, and also for the case of MR fluids. In the case of lamellar fragments, we intend to perform some more quantitative comparisons between our results and those in Ref. [154]. Moreover, the study of these two different branches of viscous fingering phenomena opens up an intriguing question about the possibility of manipulating actin-based cell motility by magnetic means. Doping cells or an extracellular medium with nanometer sized magnetic particles is already a feasible experiment, and by applying an external magnetic field maybe one could conveniently tune cell threadmilling. Our weakly nonlinear analytical approach and numerical phase-field tools may help us to elucidate this kind of issue.

References

[1] P. G. Saffman and G. I. Taylor, Proc. R. Soc. London Ser. A **245**, 312 (1958).

[2] G. Homsy, Annu. Rev. Fluid Mech. **19**, 271 (1987); K. V. McCloud and J. V. Maher, Phys. Rep. **260**, 139 (1995); J. Casademunt, Chaos **14**, 809 (2004).

[3] K. V. McCloud and J. V. Maher, Phys. Rep. **260**, 139 (1995).

[4] V. M. Entov, P. I. Etingof, and D. Ya. Kleinbock, Eur. J. Appl. Math. **6**, 399 (1996).

[5] F. X. Magdaleno, A. Rocco, and J. Casademunt, Phys. Rev. E **62**, R5887 (2000).

[6] D. Crowdy, Q. Appl. Math. **60**, 11 (2002).

[7] C.-Y. Chen and S.-W. Wang, Fluid Dyn. Res. **30**, 315 (2002).

[8] Ll. Carrillo, F. X. Magdaleno, J. Casademunt and J. Ortín, Phys. Rev. E **54**, 6260 (1996).

[9] E. Alvarez-Lacalle, J. Ortín, and J. Casademunt, Phys. Fluids **16**, 908 (2004).

[10] E. Alvarez-Lacalle, J. Ortín, and J. Casademunt, Phys. Rev. E **74**, 025302(R) (2006).

[11] S. Ramezani, S. Aniss, and M. Souhar, C. R. Mec. **330**, 633 (2002).

[12] S. L. Waters and L. J. Cummings, Phys. Fluids **17**, 048101 (2005).

[13] R. Folch, E. Alvarez-Lacalle, J. Ortín, and J. Casademunt, Phys. Rev. E **80**, 056305 (2009).

[14] R. E. Rosensweig, *Ferrohydrodynamics* (Cambridge University Press, Cambridge, 1985).

[15] E. Blums, A. Cebers, and M. M. Maiorov, *Magnetic fluids* (de Gruyter, New York, 1997).

[16] A. O. Tsebers and M. M. Maiorov, Magnetohydrodynamics (N.Y.) **16**, 21 (1980).

[17] D. P. Jackson, R. E. Goldstein and A. O. Cebers, Phys. Rev. E **50**, 298 (1994).

[18] G. Pacitto, C. Flament, J.-C. Bacri, and M. Widom, Phys. Rev. E **62**, 7941 (2000).

[19] A. J. Dickstein, S. Eramilli, R. E. Goldstein, D. P. Jackson and S. A. Langer, Science **261**, 1012 (1993).

[20] S. Elborai, D.-K. Kim, X. He, S. -H. Lee, S. Rhodes, and M. Zahn, J. Appl. Phys. **97**, 10Q303 (2005).

[21] D. P. Jackson and J. A. Miranda, Phys. Rev. E **67**, 017301 (2003).

[22] D. P. Jackson and J. A. Miranda, Eur. Phys. J. E **23**, 389 (2007).

[23] C.-Y. Chen, S. -Y. Wu, and J. A. Miranda, Phys. Rev. E **75**, 036310 (2007).

[24] R. M. Oliveira, J. A. Miranda, and E. S. G. Leandro, Phys. Rev. E **77**, 016304 (2008).

[25] J. Rabinow, AIEE Trans. **67**, 1308 (1948).

[26] J. M. Ginder, in *Encyclopedia of Applied Physics*, edited by G. L. Trigg (VCH, Weinheim, 1996), Vol. 16, p. 487.

[27] J. M. Ginder, MRS Bull. **23**, 26 (1998).

[28] G. Bossis, S. Lacis, A. Meunier, and O. Volkova, J. Magn. Magn. Mater. **252**, 224 (2002).

[29] S. Genç and P. P. Phulé, Smart Mater. Struct. **11**, 140 (2002).

[30] H. A. Barnes, J. Non-Newtonian Fluid Mech. **81**, 133 (1999).

[31] P. Moller, A. Fall, V. Chikkadi, D. Derks, and D. Bonn, Phil. Trans. R. Soc. A **367**, 5139 (2009).

[32] P. Coussot, J. Fluid Mech. **380**, 363 (1990).

[33] E. Lemaire, P. Levitz, G. Daccord, and H. Van Damme, Phys. Rev. Lett. **67**, 2009 (1991).

[34] A. Lindner, P. Coussot, and D. Bonn, Phys. Rev. Lett. **85**, 314 (2000).

[35] A. B. Verkhovsky, T. M. Svitkina, and G. G. Borisy, Curr. Biol. **9**, 11 (1999).

[36] A. C. Callan-Jones, J.F. Joanny, and J. Prost, Phys. Rev. Lett. **100**, 258106 (2008).

[37] J. Casademunt, Chaos **14**, 809 (2004).

[38] S. A. Lira and J. A. Miranda, Phys. Rev. E **84**, 016303 (2011).

[39] S. A. Lira and J. A. Miranda, Phys. Rev. E **86**, 056301 (2012).

[40] S. A. Lira, J. A. Miranda, and R. M. Oliveira, Phys. Rev. E **81**, 046303 (2010).

[41] S. A. Lira, J. A. Miranda, and R. M. Oliveira, Phys. Rev. E **82**, 036318 (2010).

[42] J. V. Fontana, S. A. Lira, and J. A. Miranda, Phys. Rev. E **87**, 013016 (2013).

[43] R. Folch, J. Casademunt, A. Hernández-Machado, and L. Ramrírez-Piscina, Phys. Rev. E **60**, 1724 (1999).

[44] J. -C. Bacri, R. Perzynski, and D. Salin, Endeavour **12**, 76 (1988).

[45] M. Seul and D. Andelman, Science **267**, 476 (1995).

[46] M. Zahn, J. Nanoparticle Research **3**, 73 (2001).

[47] D. Andelman and R. E. Rosensweig, J. Phys. Chem. B **113**, 3785 (2009).

[48] J. -C. Bacri and F. Elias, in *Morphogenesis - Origins of Patterns and Shapes*, edited by P. Bourgine and A. Lesne (Springer, New York, 2011).

[49] M. D. Cowley and R. E. Rosensweig, J. Fluid Mech. **30**, 671 (1967).

[50] V. N. Zaitsev and M. I. Shliomis, Sov. Phys. Dokl. **14**, 1001 (1970).

[51] A. Gailitis, J. Fluid Mech. **82**, 401 (1977).

[52] A. Engel, H. Langer, and V. Chetverikov, J. Magn. Magn. Mater. **195**, 212 (1999).

[53] B. Abou, J.-E. Wesfreid, and S. Roux, J. Fluid Mech. **416**, 217 (2000).

[54] R. Friedrichs and A. Engel, Phys. Rev. E **64**, 021406 (2001).

[55] R. Richter and I. V. Barashenkov, Phys. Rev. Lett. **94**, 184503 (2005).

[56] C.-Y. Chen, W.-K. Tsai, and J. A. Miranda, Phys. Rev. E **77**, 056306 (2008).

[57] F. Boyer and E. Falcon, Phys. Rev. Lett. **101**, 244502 (2008).

[58] J.-C. Bacri and D. Salin, J. Phys. Lett. **45**, 559 (1984).

[59] C. Flament, S. Lacis, J.-C. Bacri, A. Cebers, S. Neveu, and R. Perzynski, Phys. Rev. E **53**, 4801 (1996).

[60] J. A. Miranda and M. Widom, Int. J. Mod. Phys. B **12**, 931 (1998).

[61] J. A. Miranda and M. Widom, Physica D **120**, 315 (1998).

[62] A. O. Cebers, Magnetohydrodynamics (N.Y.) **17**, 113 (1981).

[63] S. A. Langer, R. E. Goldstein, and D. P. Jackson, Phys. Rev. A **46**, 4894 (1992).

[64] J. Richardi, D. Ingert, and M. P. Pileni, Phys. Rev. E **66**, 046306 (2002).

[65] J. Richardi and M. P. Pileni, Prog. Theor. Chem. Phys. **12**, 41 (2003).

[66] S. H. Strogatz, *Nonlinear dynamics and chaos: with applications to physics, biology, chemistry, and engineering* (Addison-Wesley, New York, 1994).

[67] J. F. Nye, H. W. Lean, and A. N. Wright, Eur. J. Phys. **5**, 73 (1984).

[68] E. Alvarez-Lacalle, J. Ortín, and J. Casademunt, Phys. Rev. Lett. **92**, 054501 (2004).

[69] M. Zeybek and Y. C. Yortsos, Phys. Rev. Lett. **67**, 1430 (1991).

[70] M. Zeybek and Y. C. Yortsos, J. Fluid Mech. **241**, 421 (1992).

[71] P. Gondret and M. Rabaud, Phys. Fluids **9**, 3267 (1997).

[72] L. Meignin, P. Gondret, C. Ruyer-Quil, and M. Rabaud, Phys. Rev. Lett. **90**, 234502 (2003).

[73] C. Ruyer-Quil, C. R. Acad. Sci., Ser. IIb: Mec. **329**, 337 (2001).

[74] F. Plouraboué and E. J. Hinch, Phys. Fluids **14**, 922 (2002).

[75] E. J. Hinch and F. Plouraboué, Phys. Fluids **17**, 052107 (2005).

[76] J. A. Miranda and M. Widom, Phys. Rev. E **61**, 2114 (2000).

[77] For recent reviews on ferrofluids, see for instance, D. Andelman and R. E. Rosensweig, J. Phys. Chem. B **113**, 3785 (2009); J. -C. Bacri and F. Elias, in *Morphogenesis - Origins of Patterns and Shapes*, edited by P. Bourgine and A. Lesne (Springer, New York, 2011).

[78] S. Orzag, J. Fluid Mech. **50**, 689 (1971).

[79] T. Tatsumi and T. Yoshimura, J. Fluid Mech. **212**, 437 (1990).

[80] C. Rinaldi, A. Chaves, S. Elborai, X. He, and M. Zahn, Curr. Opin. Colloid Interface Sci. **10**, 141 (2005).

[81] D. Andelman and R. E. Rosensweig, J. Phys. Chem. B **113**, 3785 (2009).

[82] H. Shahnazian and S. Odenbach, Int. J. Mod. Phys. B **21**, 4806 (2007).

[83] H. Shahnazian and S. Odenbach, J. Phys.: Condens. Matter **20**, 204137 (2008).

[84] C.-Y. Chen, Y. -S. Yang, and J. A. Miranda, Phys. Rev. E **80**, 016314 (2009).

[85] G. H. Covey and B. R. Stanmore, J. Non-Newton. Fluid Mech. **8**, 249 (1981).

[86] S. A. Lira and J. A. Miranda, Phys. Rev. E **80**, 046313 (2009).

[87] R. Ewoldt, PhD thesis, Massachusetts Institute of Technology, 2009.

[88] R. Ewoldt, G. McKinley, and A. Hosoi, Bull. Am. Phys. Soc. **53**, No. 15, 252 (2008).

[89] S. A. Lira and J. A. Miranda, Phys. Rev. E **79**, 046303 (2009).

[90] E. Alvarez-Lacalle, E. Pauné, J. Casademunt, and J. Ortín, Phys. Rev E **68**, 026308 (2003).

[91] H. Gadêlha and J. A. Miranda, Phys. Rev. E **70**, 066308 (2004).

[92] J. A. Miranda and M. Widom, Int. J. Mod. Phys. B **12**, 931 (1998).

[93] E. Alvarez-Lacalle, J. Casademunt, and J. Ortín, Phys. Rev E **64**, 016302 (2001).

[94] G. Tryggvason and H. Aref, J. Fluid Mech. **136**, 1 (1983).

[95] G. Birkhoff, Los Alamos Scientific Laboratory Technical Report No. LA-1862, 1954 (unpublished).

[96] P. Kuzhir, M. T. López-López, and G. Bossis, Phys. Fluids **21**, 053101 (2009).

[97] P. P. Phulé and J. M. Ginder, Int. J. Mod. Phys. B **13**, 2019 (1999).

[98] E. S. G. Leandro, R. M. Oliveira, and J. A. Miranda, Physica D **237**, 652 (2008).

[99] J. White, J. Oakley, M. Anderson, and R. Bonazza, Phys. Rev E **81**, 026303 (2010).

[100] E. Alvarez-Lacalle, J. Ortín, and J. Casademunt, Phys. Fluids **16**, 908 (2004).

[101] J. Plateau, *Annu. Rep. Board Regents Smithson Inst.*, 207-285 (1863).

[102] R. A. Brown and L. E. Scriven, Proc. R. Soc. London A **371**, 331 (1980).

[103] K. Ohsaka and E. H. Trinh, Phys. Rev. Lett. **84**, 1700 (2000).

[104] R. J. A. Hill and L. Eaves, Phys. Rev. Lett. **101**, 234501 (2008).

[105] C. L. Shen, W. J. Xie, and B. Wei, Phys. Rev. E **81**, 046305 (2010).

[106] V. Cardoso and Ó. J. C. Dias, Phys. Rev. Lett. **96**, 181601 (2006).

[107] N. Bohn and J. A. Wheeler, Phys. Rev. **56**, 426 (1939).

[108] V. G. Kartavenko, K. A. Gridnev, and W. Greiner, Phys. Atom. Nucl. **65**, 637 (2002).

[109] L. W. Schwartz, Phys. Fluids A **1**, 167 (1989).

[110] J. A. Miranda, Phys. Rev. E **62**, 2985 (2000).

[111] J. A. Miranda and E. Alvarez-Lacalle, Phys. Rev. E **72**, 026306 (2005).

[112] D. Bonn and M. Denn, Science **324**, 1401 (2009).

[113] G. Ovarlez, Q. Barral, and P. Coussot, Nature Mater. **9**, 115 (2010).

[114] J. V. Maher, Phys. Rev. Lett. **54**, 1498 (1985).

[115] A. J. DeGregoria and L. W. Schwartz, J. Fluid Mech. **164**, 383 (1986).

[116] E. Meiburg and G. M. Homsy, Fluids **31**, 429 (1988).

[117] C. -W. Park and G. M. Homsy, Phys. Fluid **28**, 1583 (1985).

[118] P. Tabeling, G. Zocchi and A. Libchaber, J. Fluid Mech. **177**, 67 (1987).

[119] T. Maxworthy, J. Fluid Mech. **177**, 207 (1987).

[120] A. Arnéodo, Y. Couder, G. Grasseau, V. Hakim and M. Rabaud, Phys. Rev. Lett. **63**, 984 (1989).

[121] J. Bataille, Rev. Inst. Fr. Pet. Ann. Combust. Liq. **23**, 1349 (1968).

[122] S. D. R. Wilson, J. Colloid Interface Sci. **51**, 532 (1975).

[123] L. Paterson, J. Fluid Mech. **113**, 513 (1981).

[124] J.-D. Chen, J. Fluid Mech. **201**, 223 (1989); J. -D. Chen, Exp. Fluids **5**, 363 (1987).

[125] H. Thomé, M. Rabaud, V. Hakim, and Y. Couder, Phys. Fluids **A1**, 224 (1989).

[126] O. Praud and H. L. Swinney, Phys. Rev. E **72**, 011406 (2005).

[127] P. Fast and M. J. Shelley, J. Comput. Phys. **212**, 1 (2006).

[128] J. Mathiesen, I. Procaccia, H. L. Swinney, and M. Thrasher, Eur. Phys. Lett. **76**, 257 (2006).

[129] S. W. Li, J. S. Lowengrub, and P. H. Leo, J. Comput. Phys. **225**, 554 (2007).

[130] C.-Y. Chen, C.-W. Huang, H. Gadêlha, and J. A. Miranda, Phys. Rev. E **78**, 016306 (2008).

[131] S. W. Li, J. S. Lowengrub, J. Fontana, and P. Palffy-Muhoray, Phys. Rev. Lett. **102**, 174501 (2009).

[132] R. B. Bird, R. Armstrong, and O. Hassager, *Dynamics of Polymeric Liquids* (Wiley, New York, 1977).

[133] A. Buka, P. Palffy-Muhoray, and Z. Racz, Phys. Rev. A **36**, 3984 (1987).

[134] H. Zhao and J. V. Maher, Phys. Rev. E **47**, 4278 (1993).

[135] J. Ignés-Mullol, H. Zhao and J. V. Maher, Phys. Rev. E **51**, 1338 (1995).

[136] N. Kagei, D. Kanie, and M. Kawaguchi, Phys. Fluids **17**, 054103 (2005).

[137] J. E. Sader, D. Y. C. Chan, and B. D. Hughes, Phys. Rev. E **49**, 420 (1994).

[138] D. Bonn, H. Kellay, M. Ben Amar and J. Meunier, Phys. Rev. Lett. **75**, 2132 (1995); D. Bonn, H. Kellay, M. Braunlich, M. Ben Amar, and J. Meunier, Physica A **220**, 60 (1995).

[139] L. Kondic, P. Palffy-Muhoray, and M. J. Shelley, Phys. Rev. E **54**, R4536 (1996).

[140] L. Kondic, M. J. Shelley, and P. Palffy-Muhoray, Phys. Rev. Lett. **80**, 1433 (1998).

[141] E. Corvera Poiré and M. Ben Amar, Phys. Rev. Lett. **81**, 2048 (1998).

[142] M. Ben Amar and E. Corvera Poiré, Phys. Fluids **11**, 1757 (1999).

[143] P. Fast, L. Kondic, M. J. Shelley, and P. Palffy-Muhoray, Phys. Fluids **13**, 1191 (2001).

[144] M. Constantin, M. Widom, and J. A. Miranda, Phys. Rev. E **67**, 026313 (2003).

[145] P. Fast and M. J. Shelley, J. Comput. Phys. **195**, 117 (2004).

[146] S. Nguyen, R. Folch, V. K. Verma, H. Henry, and M. Plapp, Phys. Fluids **22**, 103101 (2010).

[147] N. Maleki-Jirsaraei, A. Lindner, S. Rouhani, and D. Bonn, J. Phys.: Condens. Matter **17**, S1219 (2005).

[148] G. K. Batchelor, *An Introduction to Fluid Dynamics* (Cambridge University Press, Cambridge, 1967).

[149] G. Dai and R. B. Bird, J. Non-Newtonian Fluid Mech. **8**, 349 (1981).

[150] G. G. Lipscomb and M. M. Denn, J. Non-Newtonian Fluid Mech. **14**, 337 (1984).

[151] S. D. R. Wilson, J. Non-Newtonian Fluid Mech. **47**, 211 (1993).

[152] J. M. Piau, J. Rheol. **40**, 711 (1996).

[153] Y. Sun, and C. Beckermann, J. Comput. Phys. **220**, 626 (2007).

[154] C. Blanch-Mercader and J. Casademunt, Phys. Rev. Lett. **110**, 078102 (2013).

[155] F. Ziebert, S. Swaminathan and I. S. Aranson, J. R. Soc. Interface **9**, 1084 (2012).

[156] D. Shao, H. Levine and W-J Rappel, PNAS, vol. **109**, no. 18 (2012).

[157] Peter Smereka, SIAM J. Sci. Comput. **19**, 1 (2003).

[158] D. Rannacher and A. Engel, New J. Phys. **8**, 108 (2006).

[159] E. Bourdin, J.-C. Bacri, and E. Falcon, Phys. Rev. Lett. **104**, 094502 (2010).